UNIVERSITY OF SOUTHAMPTON

Design of a High Temperature Superconducting Coil for Energy Storage Applications

by

Andreas W. Zimmermann

A thesis submitted for the degree of Master of Philosophy

Faculty of Engineering and Physical Sciences

March 2021

Declaration of Authorship

I, Andreas-Walter Zimmermann, declare that this thesis titled, "Design of a High Temperature Superconducting Coil for Energy Storage Applications" and the work presented in it are my own. I confirm that:

- This work was done wholly or mainly while in candidature for a research degree at this University.
- Where any part of this thesis has previously been submitted for a degree or any other qualification at this University or any other institution, this has been clearly stated.
- Where I have consulted the published work of others, this is always clearly attributed.
- Where I have quoted from the work of others, the source is always given. With the exception of such quotations, this thesis is entirely my own work.
- I have acknowledged all main sources of help.
- Where the thesis is based on work done by myself jointly with others, I have made clear exactly what was done by others and what I have contributed myself.

Signed: _____

Date: _____

UNIVERSITY OF SOUTHAMPTON

Abstract

Faculty of Engineering and Physical Sciences

Master of Philosophy

Design of a High Temperature Superconducting Coil for Energy Storage Applications

by Andreas W. Zimmermann

Besides applications in magnetic resonance imaging (MRI) and particle accelerators, superconductors have been proposed in power systems for use in fault current limiters, cables and energy storage. Since its introduction in 1969, superconducting magnetic energy storage (SMES) has become one of the most power-dense storage systems, with over 1 kW/kg, placing them in the category of high power technologies, along with supercapacitors and flywheels. The discovery of high temperature superconductors (HTS) in 1986, with transition temperatures of over 90 K, brought a series of advantages over low temperature superconducting magnets (operating below 4.2 K), which include a higher operating temperature, of up to 77 K, improved thermal stability and higher critical current in magnetic fields. This has enabled the use of SMES in projects requiring large power pulses and quick response time, such as grid scale balancing services. However, due to large costs of superconducting tape, exceeding $100/m, only small scale magnets, with storage capacity below 1 MJ have been built.

This project's aim is to study the design of a HTS coil for use in energy storage systems. A methodology is proposed for a parametric design of a superconducting magnet using second generation high temperature tape, made with Yttrium Barium Copper Oxide(YBCO). The process takes into account the target energy stored, the output power and the voltage of the magnet, the latter of which has a direct impact on peak transport current required, and hence, the choice of tape and operating temperature. The search algorithm is scripted in R, with a function that takes the deliverable energy, power and voltage as input parameters and returns the near-optimum configuration of a coil that uses the minimum length of tape, achieved through discrete optimisation.

The resulting configuration is used in a MATLAB/Simulink simplified model of a DC microgrid. The operation of the coil is assessed during two scenarios, simulating a demand and surplus of power, respectively. The bidirectional power flow between the coil and the circuit is enabled by a two quadrant DC-DC chopper, controlled using PWM generated by a closed loop PI controller. The effect of increasing the controller gains by an order of magnitude is observed in the quicker response of the coil and a lower variation of DC link capacitor voltage.

Acknowledgements

My entire experience in this research degree has been fantastic and this is mainly due to the people I have had the pleasure of meeting and collaborating with. Firstly, I would like to express my deep gratitude to my supervisor, Prof. Suleiman Sharkh, for his calm and approachable attitude, his dedication to knowledge and his immense patience, which have encouraged me to analyse concepts in more detail and be curious about everything. I have thoroughly enjoyed our talks and one lesson I will always remember is to always ask the right questions!

Being part of the CDT for Energy Storage and its Applications certainly made my post-graduate experience more dynamic and enjoyable. For this I would like to thank Prof. Andy Cruden for his involvement in improving the experience as part of the centre, as well as Sharon Brown for her support and encouragement. Also, I am grateful for all the discussions (serious or less so), the ideas shared and the banter with the wonderful colleagues from the CDT. I had so much to learn from you and I feel that we have created some strong connections that will last for a lifetime. In particular, I would like to thank James, who I've now known for almost a third of my life, since the first week at uni, as well as Harriet, Ewan Fraser and Nick Hillier for their friendship and support.

Finally, I would like to thank my amazing wife, Mara, for always believing in me, listening to my rants, lifting me in moments of doubt and showing me that life is colourful and much more than a project. A huge thank you to my parents and my brother, who have always shown unconditional support. I couldn't have done it without you and I hope I did you proud.

Contents

Declaration of Authorship iii

Abstract v

Acknowledgements vii

Contents ix

List of Figures xiii

List of Tables xvii

Abbreviations xix

Nomenclature and Physical Constants xxi

1 Introduction 1

1.1 Energy Storage in Sustainable Systems 1

1.2 High Power Storage Technologies 4

1.2.1 Flywheel Energy Storage (FES) 4

1.2.2 Supercapacitors (SC) 5

1.2.3 Superconducting Magnetic Energy Storage (SMES) 6

1.2.4 Discussion 8

1.3 SMES components 9

1.4 SMES: History and Current State of the Art 14

1.5 Knowledge gaps and Research Motivation 17
1.6 Project Aim and Objectives 19
1.7 Thesis Outline 19

2 SMES Background **21**
2.1 Introduction to Superconductivity 21
2.1.1 Meissner effect 22
2.1.2 London Penetration Depth 22
2.1.3 Type I and Type II superconductors 23
2.2 Practical Superconductors 26
2.2.1 Timeline of practical superconductors 26
2.2.2 First and Second Generation HTS 28
2.2.3 HTS Anisotropy 30
2.3 Critical State Models 32
2.3.1 Bean model 33
2.3.2 Kim model 34
2.3.3 E-J Power law 34
2.4 AC losses 35
2.5 Magnet Winding and Optimisation 36
2.6 Refrigeration and Quench Protection 38
2.6.1 Refrigeration for superconducting magnets 38
2.6.2 Cryocoolers: Types and operation 39
2.6.3 Quench Protection 43

3 SMES Magnet Design **45**
3.1 Methodology 45
3.1.1 Initial assumptions 45
3.1.2 Outline of design methodology 48
3.2 Superconducting tape selection 51
3.3 Magnetic fields in coils 55

3.4 Coil inductance . . . 62
3.5 Stress and strain . . . 62
3.6 Stored energy and final configuration . . . 63
3.7 Impact of power and voltage . . . 66
3.8 Discussion . . . 67

4 SMES power control **69**
4.1 Model setup . . . 69
4.1.1 Modes of operation of SMES magnet . . . 69
4.1.2 DC microgrid simplified model . . . 71
4.2 Simulation Scenarios . . . 74
4.2.1 Magnet Storage Mode . . . 74
4.2.2 Magnet Discharge Mode at 100 kW . . . 75
4.2.3 Magnet Charge Mode at 100 kW . . . 78
4.3 Summary . . . 79

5 Conclusions and Further Work **81**
5.1 Conclusions . . . 81
5.2 Recommended Future Work . . . 83

A Field scaling factors **85**

B Coil Optimisation Code **89**

C Stress equation **97**

References **101**

List of Figures

1.1 Types of energy storage applications at different response and discharge times 2

1.2 Ragone plot . . . 3

1.3 Proportion of energy used in a SMES unit delivering 5 MJ at 1 MW . . . 8

1.4 SMES components . . . 10

1.5 Illustration of T-H-J Critical Surface . . . 11

1.6 AC/DC converters for SMES-battery . . . 12

1.7 Diagram of persistent switch . . . 13

1.8 Placement of coils in a proposed hybrid SMES model . . . 16

2.1 Meissner effect in a superconductor . . . 22

2.2 Magnetic field distribution along the thickness of a superconductor . . . 23

2.3 Magnetization of superconductors . . . 24

2.4 Distribution of fluxons under different phases, as a function of temperature and magnetic field . . . 25

2.5 The discovery timeline of major superconducting materials . . . 27

2.6 Cross sections of HTS tapes . . . 28

2.7 Cross section of an YBCO coated conductor . . . 29

2.8 HTS tape anisotropy . . . 31

2.9 Structure of Roebel YBCO cables . . . 32

2.10 Current density across the tape width under changing external fields according to Bean's model . . . 33

2.11 Power law in YBCO tapes . . . 35

2.12 SMES Solenoid configuration . . . 37

2.13 Diagram of double pancake coil . . . 37

2.14 Different coil types . . . 38
2.15 Recuperative refrigeration cycles . . . 40
2.16 Regenerative refrigeration cycles . . . 41

3.1 Diagram of YBCO tape structure and dimensions . . . 46
3.2 Cross section of a 6 layer double pancake . . . 47
3.3 Flow chart outlining the design steps for the superconducting magnet . . . 49
3.4 Critical Current as a function of perpendicular field at 22 K in Superpower SCS12050 tape . . . 53
3.5 Critical curve of SCS12050 at 22 K . . . 54
3.6 Diagram of the cross section in an axisymmetric solenoid . . . 56
3.7 Ratio between maximum and central axial field in a rectangular cross section coil, as a function of α and β . . . 57
3.8 Ratio between radial and axial magnetic field as a function of α and β . . . 58
3.9 Load lines for a solenoid with fixed α and β and variable R_i . . . 59
3.10 Load lines for a solenoid with fixed R_i and α and variable β . . . 60
3.11 Load lines for a solenoid with fixed R_i and β and variable α . . . 60
3.12 Load lines for a solenoid $\alpha = 1.08$ and $\beta = 0.25$ and variable R_i . . . 61
3.13 Model of the solenoid with the final parameters . . . 65
3.14 Tape length and peak operating current as a function of voltage . . . 66

4.1 SMES DC-DC chopper in charge mode . . . 70
4.2 SMES chopper in discharge mode . . . 71
4.3 SMES chopper in storage mode . . . 71
4.4 Circuit diagram of the SMES connected to a DC-DC chopper, a DC-link capacitor and a load . . . 72
4.5 PI Control loop for IGBTs T1 and T2 . . . 72
4.6 Intersective PWM generation method . . . 73
4.7 DC link capacitor current and voltage during storage . . . 74
4.8 Coil transport current and voltage during storage . . . 75
4.9 DC link capacitor voltage and current during the compensation of a 100 kW load, with PI gains of 1 . . . 76

4.10 Coil voltage and transport current during the compensation of a 100 kW load, with PI gains of 1 76

4.11 DC link capacitor voltage and current during the compensation of a 100 kW load, with PI gains of 100 77

4.12 Coil voltage and transport current during the compensation of a 100 kW load, with PI gains of 100 77

4.13 DC link capacitor voltage and current during the compensation of a 100 kW load, with PI gains of 100 and a SMES current of 150A 78

4.14 Coil voltage and transport current during the compensation of a 100 kW load, with PI gains of 100, when the coil current starts at 150 A 78

4.15 DC link capacitor voltage and transport current during the compensation of a 100 kW excess power injection, with PI gains of 100 79

4.16 Coil voltage and transport current during the compensation of a 100 kW excess power injection, with PI gains of 100 79

List of Tables

1.1 Characteristics of Grid-scale energy storage systems 5

2.1 Summary of Cryocoolers 42

3.1 Properties of Superpower SCS12050 YBCO tape 52

3.2 Values of Young's modulus for various configurations of SCS12050 tape . . 63

3.3 Matrix T 64

3.4 Final design parameters of 1MJ/100kW YBCO SMES 65

4.1 IGBT Switching Pattern 70

A.1 Values of shape factors F, G and K depending on α and β 85

Abbreviations

1G	**1**st **G**eneration
2G	**2**nd **G**eneration
AC	**A**lternating **C**urrent
CAES	**C**ompressed **A**ir **E**nergy **S**torage
CSC	**C**urrent **S**ource **C**onverter
DC	**D**irect **C**urrent
DDLWEC	**D**irect **D**rive **L**inear **W**ave **E**nergy **C**onverter
DVR	**D**ynamic **V**oltage **R**estorer
emf	**e**lectro**m**otive **f**orce
ES	**E**nergy **S**torage
EV	**E**lectric **V**ehicles
GM	**G**ifford **M**cMahon
HEV	**H**ybrid **E**lectric **V**ehicles
HTS	**H**igh **T**emperature **S**uperconductors
IGBT	**I**nsulated **G**ate **B**ipolar **T**ransistor
LTS	**L**ow **T**emperature **S**uperconductors
LVDC	**L**ow **V**oltage **D**irect **C**urrent
m-CHP	**m**icro- **C**ombined **H**eat (and) **P**ower
MOV	**M**etal **O**xide **V**aristor
MTS	**M**edium **T**emperature **S**uperconductors
NPC	**N**eutral **P**oint **C**lamped
PHES	**P**lug-in **H**ybrid **E**lectric **V**ehicles
PCU	**P**ower **C**onditioning **U**nit
PID	**P**roportional- **I**ntegral- **D**erivative
PV	**P**hoto**v**oltaic

PT	**P**ulse **T**ube
PWM	**P**ulse **W**idth **M**odulation
ReBCO	**R**are-earth **B**arium **C**opper **O**xide
SC	**S**uper**c**apacitor
SMES	**S**uperconducting **M**agnetic **E**nergy **S**torage
UPS	**U**ninterruptible **P**ower **S**upply
VSC	**V**oltage **S**ource **C**onverter
YBCO	**Y**ittrium **B**arium**C**opper**O**xide

Nomenclature and Physical Constants

Symbol	Name	Unit
$B_z(0,0)$	Central axial field density	T
$B_\parallel$	Axial field density	T
$B_\perp$	Radial field density	T
C	Capacitance	F
e	Back electromotive force	V
E	Energy	J
f	Fill factor	-
$F(\alpha,\beta)$	Factor used to calculate field	-
$G(\alpha,\beta)$	Maximum to central axial field ratio	-
H_{c1}, H_{c2}	Critical fields in Type II wires	A/m
I_c	Critical Current	A
I_{op}	Operating (Transport Current)	A
J_c	Critical current density across YBCO layer	A/m^2
J_e	Engineering current density across tape	A/m^2
$K(\alpha,\beta)$	Radial to maximum axial field ratio	-
l	Tape Length	m
L	Inductance	H
n	electron number density	m^{-3}
P_{Cu}	Power loss in Cu layer	W
R_i	Coil inner radius	m
R_o	Coil outer radius	m

s	Safety factor	-
t	Tape thickness	m
T_c	Critical temperature	K
T_{op}	Operating temperature	K
V	Voltage	V
w	Tape width	m
Y	Young's modulus	Pa

α	external to internal coil radius ratio	-
β	coil length to internal diameter ratio	-
ω	angular velocity	rad/s
ϵ	normalised coil radius	-
ε	strain	%
κ	Ginzburg-Landau parameter	-
λ_L	London penetration depth	m
ν	Poisson's ratio	-
ξ	coherence length	m
ρ	Resistivity	Ωm
σ	Electric conductivity	S/m
σ_r	Radial Stress	Pa
σ_θ	Hoop Stress	Pa
τ	Coil discharge time	s
Φ	Magnetic Flux	Wb

Constant	**Name**	**Value and Unit**
h	Planck's constant	6.62×10^{-34} m^2kg/s
m	Mass of an electron	9.11×10^{-31} kg
q	Electric charge of an electron	1.6×10^{-19} C
μ_0	Magnetic permeability of free space	$4\pi \times 10^{-7}$ H/m
Φ_0	Magnetic flux of a fluxon	2.07×10^{-15} Wb

Chapter 1

Introduction

1.1 Energy Storage in Sustainable Systems

Over the past two decades, fossil fuels have been increasingly used as the primary energy resource across all the major sectors, including industrial, transportation and residential, leading to severe environmental effects [1]. Despite the rise in productivity, leading to economic growth, the quality of air has been significantly deteriorated due to anthropogenic pollution. In an attempt to reduce these effects, most of the world governments have signed the Paris Agreement in 2015 [2], which proposes a series of measures that must be taken in order to limit the rise of the average global temperature below 2° C, compared to the pre-industrial levels. Among the measures are the increased adoption of renewable generation, including wind turbines, solar photovoltaic (PV) panels, as well as replacing internal combustion engine (ICE) vehicles with hybrid and electric vehicles (HEV and EV)[3].

A higher penetration of renewable generation technologies leads to a less stable system and hence, increasing balancing costs. Given the low correlation between the electricity demand and the wind generation profile, periods with low demand and high generation may lead to negative day-ahead electricity prices, curtailing the subsidies for some of the newer plants [4]. Energy storage technologies are a promising solution for these issues, contributing in the transition to sustainable energy systems by filling the gaps between supply and demand. Hence, they have attracted increasing interest from both industry and

academia [5, 6]. Figure 1.1 presents a summary of grid-scale energy storage applications, depending on the response and discharge time required.

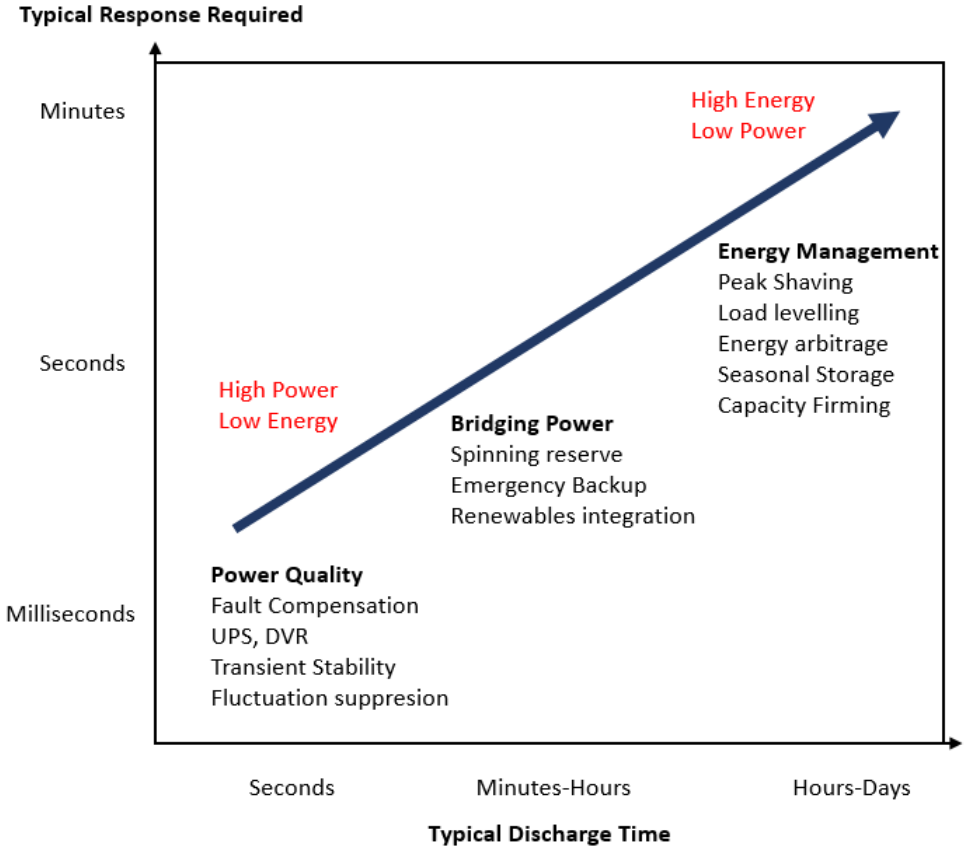

Figure 1.1: *Types of energy storage applications at different response and discharge times and their typical power and energy characteristics. Adapted from [7]*

Depending on their characteristics, storage technologies are typically classified in two categories: high energy and high power. While there is no consensus on the exact values of energy and power that would define these categories, a way of distinguishing them is through the ratio between energy storage capacity and deliverable power. In the Ragone plot from Figure 1.2, the approximate range of specific energy and specific power for some of the most popular storage technologies is represented on a logarithmic scale. A high ratio between specific energy and power is characteristic to technologies such as fuel cells, Li-ion batteries and thermal energy storage, where the typical discharge duration can exceed $10h$, thus being classified as high energy systems. On the other hand, technologies in which the specific energy to power ratio does not exceed $0.1h = 360s$ are considered high power and include supercapacitors, flywheels and superconducting magnetic energy storage (SMES).

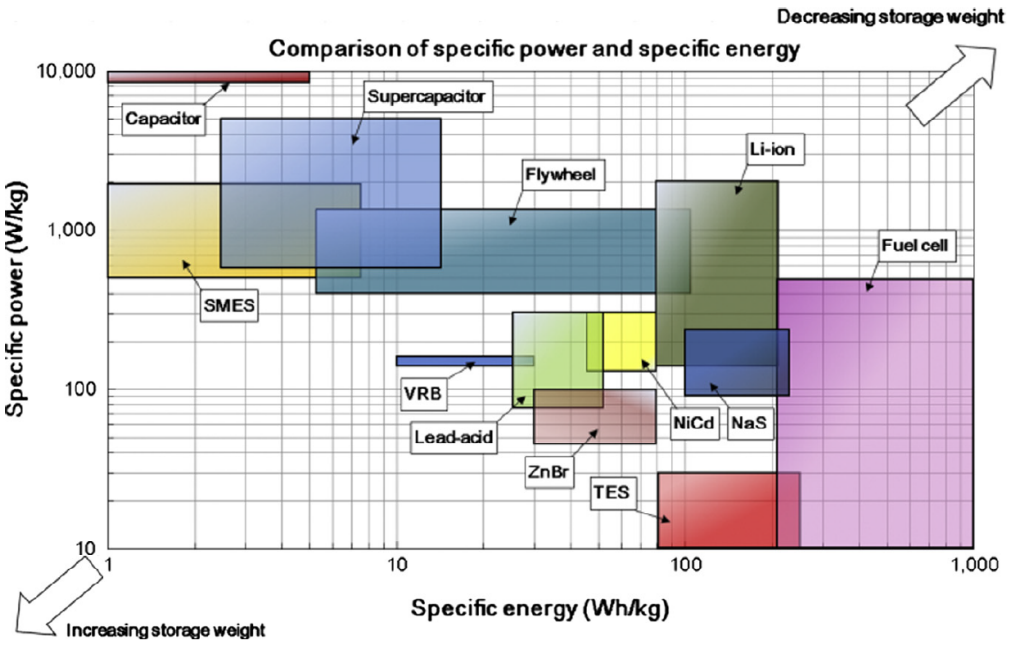

Figure 1.2: *Ragone plot showing specific energy and power levels for the most popular energy storage technologies, excluding auxiliary systems, such as enclosures or converters [6]*

This classification is valid at any scale, from small portable electronic devices, to electric vehicles, where the peak power output typically does not exceed 1 MW, with storage capacities of up to 200 kWh (extreme examples being the Tesla Roadster and Rimac Concept Two [8]), and even up to grid-scale storage, with power output in excess of 100 MW and storage capacity of at least 100 MWh.

Currently, Pumped Hydroelectric Energy Storage (PHES) represents over 99% of the entire global storage capacity, with the majority of the remainder being from Compressed Air Energy Storage (CAES) and Sodium-Sulfur batteries [9]. These are large scale systems, with capacities in the range of 1 GWh and power ratings of more than 100 MW, their economical feasibility improving with increasing size [10]. Large scale Lithium-ion batteries have also been commissioned, with demonstrators of up to 100 MW/ 129 MWh, installed by Tesla in Australia [11]. A major advantage of batteries for high energy applications is their versatility, as packs can be scaled according to energy and power requirements, and placed in any location, unlike PHES or CAES, which depend on a high head water reservoir or an underground cavern, respectively [12]. Given their large storage capacity, which enables the discharge over several hours, PHES, CAES and large scale batteries

are suitable for energy management and bridging power, being classified as high energy technologies.

High power fit at the other side of the spectrum and are suitable for power quality applications. These include compensating faults, ensuring a transient stability and maintaining a steady grid voltage and frequency [13]. While lead-acid and Lithium-ion batteries have been successfully implemented in these applications, they cannot sustain repeated high power discharge cycles without a severe effect on their storage capacity and lifespan [14]. In large scale power applications, battery packs are oversized and operate at low cycle efficiencies, which increases the overall cost [15].

Due to their lower power capital cost, extended lifetime at high discharge rates and high efficiency, superconducting magnetic energy storage (SMES), supercapacitors and flywheels are the preferred technologies in high power applications [15]. Table 1.1 provides a summary of performance characteristics of energy storage technologies used in grid applications, with the purpose of highlighting the differences between high power and high energy systems. While some of these metrics are presented as broad numeric intervals, they are useful for giving a sense of scale of each system, ultimately indicating their suitable application category.

1.2 High Power Storage Technologies

1.2.1 Flywheel Energy Storage (FES)

In flywheel energy storage (FES), electricity is used to power a motor, which spins a solid cylinder to high speeds, thus storing energy in kinetic form. At any point, the energy stored in the flywheel can be expressed through the equation:

$$E = \frac{I\omega^2}{2} \tag{1.1}$$

where I is the moment of inertia of the flywheel and ω is the angular velocity. To discharge the flywheel, the motor that spun it is used as a generator to produce electrical power in a controlled regime.

Table 1.1: *Characteristics of Grid-scale energy storage systems. Data from [6, 7, 13, 15–17]*

Parameters	PHES	CAES	Secondary Batteries (Li-ion, Lead-acid, NaS, NiCd)	Flow Batteries (Vanadium Redox, ZnBr)	SMES	Supercapacitors	Flywheels
Power Rating **(MW)**	30-5,000	< 1,000	< 100 (Li-ion), < 40 (Lead-acid)	< 50	< 10	< 0.3	< 20
Energy Capacity **(MWh)**	500-8,000	500-2,900	< 10 (Li-ion), < 244.8 (NaS)	< 5	< 0.015	< 0.0005	< 5
Response Time	mins	mins	ms	ms	ms	ms	ms
Cycle Efficiency **(%)**	70-85	45-55	65-97	60-80	95	95	90-93
Daily Self Discharge **(%)**	v.small	v.small	< 1	small	10-15	10-40	100
Lifetime **(cycles)**	< 60,000	< 30,000	< 10,000	< 12,000	100,000+	100,000+	20,000+
Power Capital Cost **($/kW)**	2,000-4,000	400-1,000	200-4,000	600-2,500	200-300	100-300	250-350
Energy Capital Cost **($/kWh)**	5-100	2-120	200-3,800	150-1,000	1,000-10,000	300-2,000	1,000-14,000

While traditionally, large steel cylinders operating at low speeds have been used in FES, developments in composite materials fabrication have enabled the manufacturing of high strength lightweight flywheels, with higher rotational speeds [18]. Moreover, to reduce friction and increase the lifetime, magnetic bearings are used, especially in high speed units [6].

The main advantages of FES are the simplicity of technology, with a straightforward way of calculating the state of charge; the extended lifetime and fast response. Unlike Li-ion batteries, the depth of discharge in flywheels does not affect the expected lifetime. On the down side, the drawbacks of FES are the very high self discharge (up to 100% per day [13]), as well as the need for containment, to prevent damage to the surroundings in case of a catastrophic failure.

1.2.2 Supercapacitors (SC)

Supercapacitors store energy in the electric field created at the electrode-electrolyte interface. Unlike flywheels, this process supposes no energy conversion from electrical to

mechanical form, which enables the cycle efficiency to reach values of up to 99%[15]. There are three main types of supercapacitors, depending on the storage mechanism and the construction: electrostatic double layer capacitor (EDLC), pseudocapacitors and hybrid capacitors [19]. The storage capacity is given by:

$$E = \frac{CV^2}{2} \tag{1.2}$$

where C is the capacitance and V is the voltage across the capacitor plates. Depending on the electrolyte used, the voltage of an individual cell can either be up to 0.9V (for aqueous electrolyte) or up to 2.7 V (for organic electrolyte). To increase the total voltage, multiple cells can be combined in series, however this requires a more complex cell management technique, ultimately increasing the cost of the system. In terms of power density, supercapacitors can reach values in excess of 5000 W/kg, with a fast response time and very high cyclability, however they have a high self discharge (of up to 40% / day [7]) and a low energy density.

1.2.3 Superconducting Magnetic Energy Storage (SMES)

Similar to an inductor, a SMES system stores energy in the magnetic field created by the current injected in the coil. What makes SMES more attractive than large inductors made of copper wires is the ability of sustaining currents with minimum decay, due to the lack of electrical resistance. This is achieved by winding the coil with superconducting wires and cooling the entire magnet below T_c, the critical transition temperature for the material used.

The energy stored in a SMES is approximated using the equation:

$$E = \frac{LI^2}{2} \tag{1.3}$$

where L is the coil self inductance and I is the transport current. While the steady state operation can be analysed by modelling the coil as a simple inductor, the transient operation requires a distributed parameter network model, in which every turn of the coil is split into multiple inductive segments, along with capacitors representing the capacitance between axially and radially adjacent turns, as well as between turns and the ground.

Given the large number of turns in a superconducting magnet, often in excess of several thousands, such mathematical model of a coil would become complicated and impractical. The distributed network model can be further simplified into an equivalent lumped circuit model, in which every inductive element represents an entire pancake winding, while the mutual inductive couplings are between axially separated pancakes. This was analysed in [20] and [21] with the purpose of determining the transient voltage distribution along the winding, which dictates the required thickness of insulation. This modelling method is however, out of the scope of this project.

According to Faraday's law, a magnetic field is building up in the bulk of the coil during charge, which then collapses during discharge. Changes in magnetic field create a back electromotive force (emf), which in turn, induces a current opposing the magnetic field change, as stated by Lenz's law. This is expressed through the equation:

$$V = -\frac{\mathrm{d}N\phi}{\mathrm{d}t} = -L\frac{\mathrm{d}I}{\mathrm{d}t} \tag{1.4}$$

where V is the voltage measured between the coil terminals, ϕ is the magnetic flux and N is the number of turns in the coil. During charge, the coil behaves like a load, therefore the rate of change of current would have the same sign as the voltage applied between the terminals.

A particularly challenging aspect of SMES is maintaining a constant power output during discharge, due to the current decaying. If the coil voltage is kept at a constant level, the output power is decreasing proportionally to the current. A solution for this problem is proposed in [22], where a coil capable of delivering 1 MW at 1 kV is designed. Here, the magnet is oversized to carry a current of 3 kA and the power converter operates in a buck mode. This is achieved by adjusting the duty cycle (the proportion of time during which the power converter switches are closed), proportionally adjusting the output voltage to give the required power output. Once the transport current decays below 1 kA, the SMES output power cannot match the required level and the remaining energy stored cannot be used. In this particular case, the proportion of useful energy is:

$$\frac{I_{max}^2 - I_{min}^2}{I_{max}^2} = \frac{3^2 - 1^2}{3^2} = 88.9\% \tag{1.5}$$

where I_{min} and I_{max} are the minimum and maximum values of transport current for which the output power can reach 1 MW. The proportion of used energy is represented in figure 1.3.

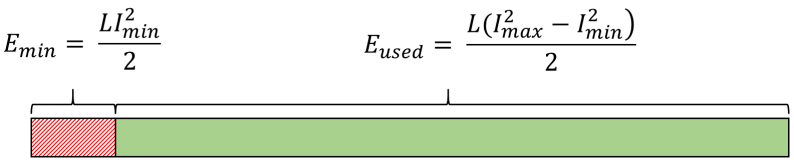

Figure 1.3: *Proportion of energy used in a SMES unit delivering 5 MJ at 1 MW, as proposed in [22]*

By oversizing the SMES unit, larger power switches are necessary to cope with the higher current, thus increasing the cost of the system. On the other hand, this situation resembles the one of a battery operating at a lower voltage than the load. In this case, a voltage boost converter is used to increase the battery voltage to the required level. With a similar approach, the current in the SMES could potentially be boosted to a higher value, increasing the proportion of energy used, while decreasing the maximum required transport current.

1.2.4 Discussion

Even if all the high-power storage technologies have similar performance characteristics, they can only be suitable for certain applications. The need for a refrigeration system and the stray magnetic fields limit the practical applications of SMES to large scale units, unlike supercapacitors and flywheels, which can be successfully used in small-scale applications, such as Kinetic Energy Recovery Systems (KERS)[23].

Scaling up is one of the challenges of high power energy storage, due to high rates of discharge, which often mean the entire deliverable energy is released over a few seconds. Equations (1.1), (1.2) and (1.3) follow a similar structure, with a constant that depends on geometrical and physical properties, multiplied by the square of a variable which represents the form in which energy is stored. Therefore, to increase the storage capacity, either the physical size, or the performance of the system must be maximised. The modularity of each system is essential in this process.

In large scale supercapacitor banks, multiple cells are connected either in series to increase the total voltage, or in parallel, to increase the capacitance. In SMES, multiple single or double pancake windings (explained in more detail in Section 2.5) are connected to form a larger solenoid, increasing the size of the cryostat required. In flywheels however, individual cylindrical masses are contained in a vacuum support structure, in order to prevent potential damage to the surroundings. Therefore, the only way of increasing the rating of the system is to combine the outputs of multiple flywheels.

Overall, when compared to supercapacitors and flywheel energy storage, a SMES unit has the lowest self discharge, of less than 15% daily [13]; the longest lifespan, estimated to exceed 20 years [15] and among the lowest operating costs less than \$0.001/kWh-cycle [9]. Nevertheless, there are still aspects that require significant improvements. Firstly, the capital cost of superconducting cables, mainly influenced by the advancement in manufacturing volume and techniques, is still very high, at 250-400 \$/kA m [24]. Secondly, high-field designs cannot contain all magnetic field lines, leading to stray field, which escapes the bulk of the coil. This is more pronounced in solenoidal coils, as some field lines would escape through the positive pole. Finally, large scale units have not been implemented widely, so there is little knowledge around their scaling and synergy with other systems in the power grid. To make SMES more attractive in future power grids, these challenges can be tackled through commissioning more test units and demonstrator projects, as well as through more intensive research into the power electronics interface and control.

1.3 SMES components

The core element of a SMES system is a coil made of superconducting wire. As long as its temperature is maintained below the critical transition value of the chosen superconducting material, T_c, its electrical resistance remains zero. This enables the coil to carry high values of transport current, thus maintaining a magnetic field. Moreover, due to the lack of resistance, the current can be sustained in a persistent, storage mode, without the need for a voltage supply and with negligible losses [25]. The persistent switch operation is explained in more detail at the end of this section.

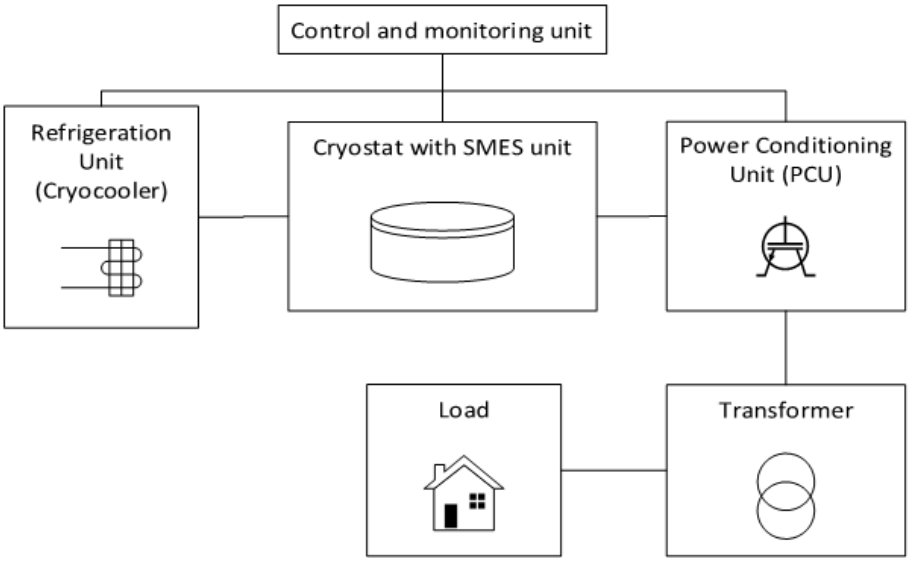

Figure 1.4: *SMES components*

Besides the superconducting coil in an insulating cryostat, a there are three other subsystems in a SMES unit, all illustrated in Figure 1.4. To maintain the temperature of the superconducting coil below the transition value, a refrigeration unit is necessary. There are two principal methods of cooling used in SMES, depending on the required operating temperature. For low temperature superconductors (LTS), such as NbTi or Nb_3Sn, where their critical transition temperature is below 20 K, a cryogen bath with liquid Helium (4.2K boil-off temperature) is required [26]. On the other hand, typical critical temperatures for high temperature superconductors (HTS) are above 90 K, allowing them to operate safely in a wider range of temperatures, which go as high as 77 K. This enables the possibility of either wet cooling (using liquid Helium, Neon, Hydrogen, Oxygen or Nitrogen), as well as dry cooling, using cryogen-free conduction coolers, which are typically smaller volume and more efficient than wet alternatives. Further detail on the types and operation of cryocoolers is given in section 2.6.1.

For any given superconductor, a critical surface can be defined, showing the relationship between J_c (the critical current density), T_c (the critical temperature) and H_c (the critical magnetic field strength), illustrated in Figure 1.5. As the operating temperature is higher, the maximum values for transport current and external magnetic fields are decreasing, as illustrated in the T-H-J diagram below. This highlights a limitation of high temperature superconducting materials operating close to their transition temperature.

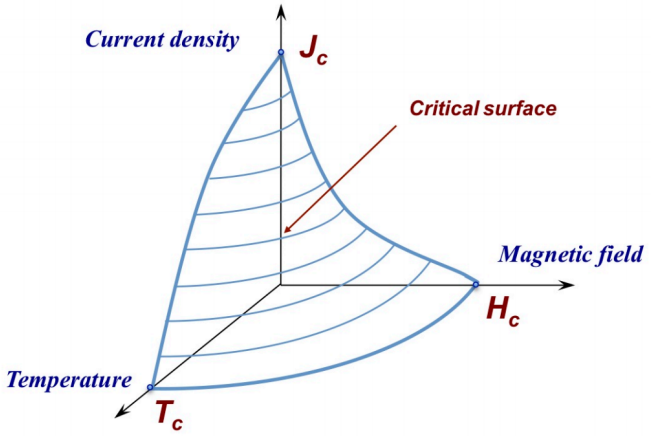

Figure 1.5: *Illustration of T-H-J Critical Surface [27]*

The power conditioning unit (PCU) consists of a power converter that enables the operation of the coil in three modes: charge, store and discharge [28]. For connection to AC grids, two main types of bidirectional converters are employed: either the current source (CSC), which connects directly to the coil and has an LC filter at the output, or a voltage source (VSC), with a DC-DC stage connected to the storage unit and comprising a chopper and an output capacitor capacitor, along with a DC-AC 3 leg, 2 level inverter, consisting of 6 Insulated Gate Bipolar Transistors (IGBT)[29]. These topologies are depicted in Figure 1.6.

In a VSC, the conduction losses are higher, due to the DC-DC chopper, which is reflected in the lower efficiency of this topology. At low power levels, CSC has a higher efficiency, with 95.7% compared to 91.3% in VSC at 10 kW and 92.7% compared to 91.1% in VSC at 50 kW [30].

In a VSC, the operation of the inverter side is independent from the type or number of energy storage devices connected, as long as the voltage of the DC link capacitor is maintained constant. Hence, the VSC topology has been extensively used in system-level SMES studies [29, 31], including hybrid SMES-battery systems[32]. The DC-DC side from a SMES VSC consists bridge chopper, that can operate in charge, store and discharge modes. The charge and discharge regimes are given by the switching pattern of the transistors in the power converter. The chopper operation was briefly discussed in the literature [33–36], however no detailed analysis on the practical sizing of switches, control methods and converter losses was done.

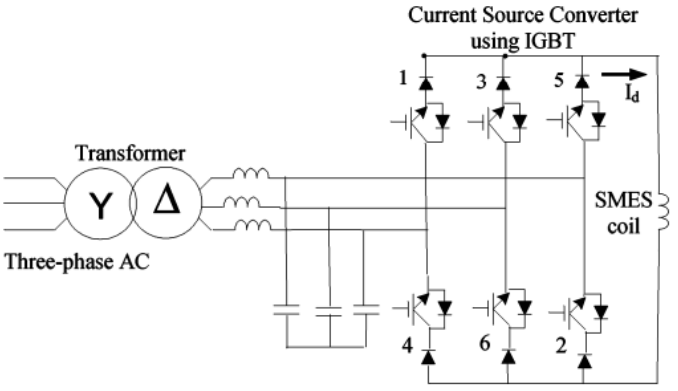

(a) CSC with SMES [29]

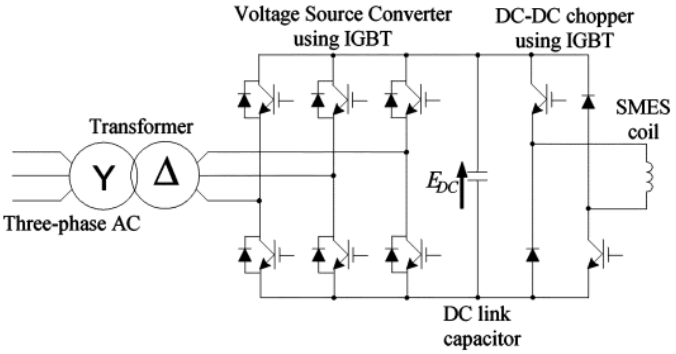

(b) VSC with SMES [29]

Figure 1.6: *AC/DC converters for SMES-battery*

The storage mode can be achieved in two ways, depending on the duration. For a short term storage, which only spans over a few minutes, this is realised by short circuiting the magnet through the power converter switches. While this is easy to achieve by controlling the switches, it has two major disadvantages. Firstly, the magnet would still be connected to the power converter circuit through the current leads, which are the main paths of heat conduction from the low temperature of the magnet to the ambient temperature of the power converter. Secondly, the coil current would circulate through a series of closed switches and diodes, which would lead to ohmic losses due to their resistance. If operated in this mode for a long time, the transport current will gradually decay, leading to a significant self discharge of the magnet.

If, however, the magnet is required to operate in persistent mode for longer periods, in applications such as nuclear magnetic resonance spectrometers (NMR), a far better

solution is the use of a persistent switch. This consists of a short length of superconducting tape, soldered at each end of the coil winding, as depicted in Figure 1.7.

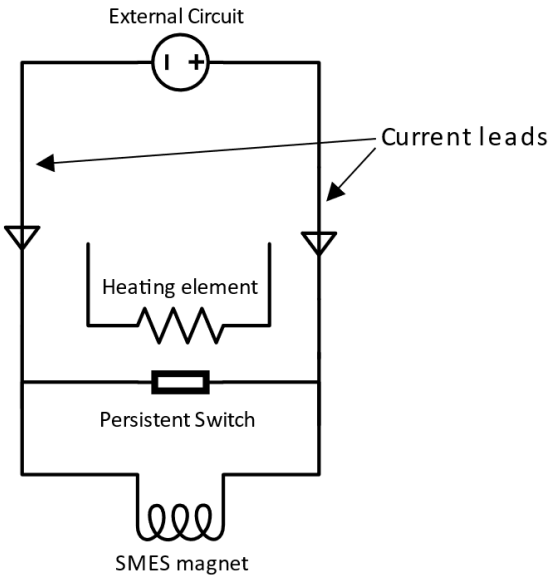

Figure 1.7: *Diagram of persistent switch*

A small heating element is attached to the switch. During charge or discharge, the persistent switch is heated up to just a few degrees above the critical temperature of the superconducting tape, making it resistive. In an experiment In this case, current only flows through the current leads to the external circuit. The small temperature difference between the 'on' and 'off' states of the switch leads to a very small heat dissipation, that can be covered by the power provided by the cryocooler.

To initiate the persistent mode, the heater is turned off and the temperature of the switch is dropping, reaching the same value as the surrounding cryogenic environment. This creates a superconducting current path and allows the magnet to function in a persistent mode, with only a minimal current decay caused by the soldered joints [37]. Typically, this transition time is between a few milliseconds to a few seconds [38].

Finally, monitoring and controlling parameters such as temperature, self-field (magnetic field generated by the current circulating in the coil, in the absence of an external magnetic field), current and voltage is essential for ensuring the coil operates in optimal conditions. For this, sensors are attached to the magnet and connected to a microprocessor, which serves the role of a monitoring and control subsystem.

If either the current density, the temperature or the magnetic field strength in a small portion of the coil exceeds the critical value given by the critical surface specific to the superconducting material used in the winding (Figure 1.5), that coil section would quench, transitioning to a resistive state. As it becomes resistive, that coil section will produce Joule heating, increasing the temperature of the surrounding areas and causing the quench to propagate throughout the coil. Therefore, quench detection is another important role fulfilled by the monitoring and control system, which engages the protection circuit to prevent damage to the coil, in case the superconductor undergoes a transition to the resistive state. More detail on quench protection is given in 2.6.3.

1.4 SMES: History and Current State of the Art

Considering the high costs of the superconducting materials, together with a SMES technology that is not yet fully developed, the number of demonstrator projects is very low, compared to other competing technologies. Moreover, most of these projects use LTS materials, where the processes of manufacturing wires and cables are mature and scalable, leading to lower costs than equivalent HTS cables.

After the concept of SMES was proposed by M. Ferrier in 1969 [24], a growing interest in the design and build of these units was reflected in the research intensity. The first practical SMES demonstrator was designed and built by General Atomic at the Los Alamos laboratory and installed in 1982 at the Tacoma substation, in Washington, USA. Its main role was to stabilise the Pacific intertie transmission line, connecting the Pacific Northwest region with Southern California. With a storage capacity of 30 MJ and a nominal power of 8.5 MW, the unit was using NbTi superconducting cables to carry a peak current of 4900 A [39]. During the following years, more LTS projects were commissioned, including a 100 MJ unit developed by Florida State University in collaboration with the Centre for Advanced Power Systems (CAPS) [40]; a 7.34 MJ NbTi coil at Chubu Electric Power Company, Japan, for bridging instantaneous voltage dips [41]; and six SMES units of 3 MJ each, as part of a distributed SMES (D-SMES) project carried by American Superconductor [42]. Smaller LTS systems, with storage capacities between 30 KJ and 3 MJ, have been built and tested over the past 20 years: a 2 MJ NbTi unit built at the Institute of Electrical Engineering in China [43], a 3 MJ NbTi unit built at the Korean Electric Research Institute

and used for voltage sag compensation [44] and a 2.6 MJ NbTi unit built at Ansaldo Richerche Spa, Italy and used in compensating voltage fluctuations [45].

With the discovery and commercialisation of high temperature superconductors (HTS), a few organisations have taken on the challenge of designing and building large scale HTS SMES units. All these units are using Bismuth-Strontium-Calcium-Copper-Oxide (Bi-2212 and 2223), a first generation (1G) HTS composite. Among the notable projects are a 600 kJ Bi-2223 unit built by the Korean Electric Research Institute for power grid stabilization [46], a 1 MJ Bi-2212 system at Chubu Electric Power Corporation, Japan, for bridging voltage dips [47] and a 800 kJ Bi-2212 unit at the National Centre for Scientific Research, France, used as a pulsed power source [48].

Second generation (2G) HTS materials, such as Rare-Earth-Barium-Copper-Oxide (where possible Rare-Earth elements are Yttrium - Y, Samarium - Sm and Gadolinium - Gd), are becoming increasingly attractive for SMES applications due to possible operating temperatures of up to 77K, requiring less cooling power than LTS [49].Despite this, there are no reports of large scale demonstrator units. Some smaller scale YBCO SMES systems have been designed and manufactured for lab tests, including a 4 kJ unit, cooled by solid nitrogen at 30K [50] and a 93 J GdBCO unit, used in a hybrid SMES-battery Dynamic Voltage Restorer(DVR), which detects a voltage drop in the system and provides fast power compensation [51, 52].

The idea of combining different types of superconducting materials in the same SMES system has also been explored, with the purpose of increasing the energy density, at a lower capital cost. One system included two solenoidal coils: a thin and long Nb-Ti coil at the exterior, for a better dissipation of heat generated by AC losses during charge-discharge cycles and a thick and short Bi-2212 coil, placed inside the NbTi unit, for a higher critical current density in magnetic fields [53, 54]. Another demonstrator unit used YBCO and BSCCO tapes, achieving a total storage capacity of 6 kJ at 69 K and used for power fluctuations compensation [55]. The choice of two different HTS materials was motivated by the way their critical current changes with the direction of external magnetic field. This property is known as anisotropy and will be explained in more detail in Chapter 2. At either end of a solenoid, the magnetic field lines are changing direction from being parallel to the central coil axis to being perpendicular. As YBCO tapes have a higher critical

current than BSCCO tapes in perpendicular field [56], YBCO coils were placed at both ends of a larger BSCCO coil, as illustrated in Figure 1.8.

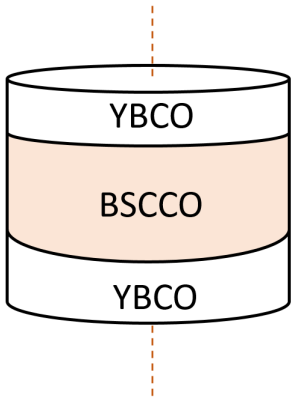

Figure 1.8: *Placement of coils in model proposed by [55]*

Apart from SMES systems that have successfully been manufactured, there are plenty of proposed HTS coil designs, capable of storing less than 1 MJ. These include an 90 kJ YBCO system for PV transient performance improvement [34, 35], a 600 kJ Bi-2223 unit for power grid stabilisation [46], a 7.65 kJ Bi-2223 unit for UPS [57] and even a 220 kJ toroidal BSCCO unit for application in hybrid vehicles [58, 59]. A more ambitious conceptual design project is the 2.4 GJ/100MVA toroidal YBCO SMES proposed by Shikimaki et al. [60] for use in load fluctuation compensation. This unit would require 2090 km of YBCO cable and would be 9.25 m in external diameter, making it very large and expensive.

Finally, the idea of combining SMES with high-energy storage systems, such as Lead-Acid and Lithium-ion batteries, has been studied in several papers. These include conceptual designs of hybrid systems for compensating power fluctuations in railway substations [61], EV fast charging stations [62] and microgrids [32, 35, 63]. Integration with renewables was also studied, considering solar PV systems [64, 65], wind turbines [66–68] and Direct Drive Linear Wave Energy Converters (DDLWEC) [69]. Applications in the transport sector were also proposed, as part of the integrated power system of a ship [70], as well as the energy storage system for a bus [71]. Different hybrid storage configurations were proposed, with a combination between a 48 GJ MgB_2 SMES and a liquid Hydrogen store [72], as well as a combination between a fuel cell, a SMES unit and a battery [73]. In most of these papers, the main focus is around the energy management and power flow control, with little consideration on the design and sizing of the storage systems, and without any detailed analysis of the topology and operation of the power converters.

Currently, two main problems prevent the commissioning of large scale SMES units: technical knowledge and cost. These two key issues are largely reciprocal, in the sense that if further technical advancements are made in the process of tape manufacturing, as well as in the design of SMES, the cost can be potentially driven down. On the other hand, technical experience can only be attained through further research which leads to practical demonstrators of HTS tape applications, but requires significant investment.

Regarding cost, the main issue is manufacturing long 2G HTS tapes that maintain a consistent and high current density throughout the entire length. The common performance metric used in benchmarking HTS tapes is the product between the maximum length and the current density achieved along the tape. Improved manufacturing techniques have led to an exponential growth of this metric, from merely 90 Am to over 300 kAm, between 2002 and 2008. However, YBCO tape costs are exceeding $40/m, nearly 20 times the cost of a metre of NbTi wire and 2.6 times the cost of Bi-2223 tape, one of the other two most used superconducting materials [24]. As large scale superconducting magnets require several kilometres of tape, the cost of 2G HTS SMES becomes very high, with an estimated cost of $1,000-10,000/kWh, nearly an order of magnitude more expensive than other competing technologies, such as Li-ion batteries with an estimated cost of $600-2,500/kWh [6].

On the other hand, the gaps in technical knowledge are mainly around the optimal design of a superconducting coil, the topology and control of the power converter, as well as the practical method of scaling up the entire system. As previously explained, some lab-scale designs of 2G HTS SMES units have been proposed [34, 50–52], but these are far from providing a realistic contribution in power systems. A more comprehensive design of an YBCO SMES unit was presented in [22], however this is practically difficult and costly to implement, due to its length of over 3 m and diameter of just under 0.8 m, requiring a large and expensive cryostat vessel.

1.5 Knowledge gaps and Research Motivation

The motivation of this project comes from the promising impact that 2G HTS SMES can have in power systems, particularly in fast frequency response (FFR) and balancing services, both at the transmission and distribution levels. Given the cost of the system,

which can be an order of magnitude higher than equivalent Li-Ion batteries, there needs to be a justification for pursuing large scale SMES systems, as currently similar types of services can be achieved with batteries. While in small scale applications, where the power requirement is in the range of several kW, batteries have a clear advantage of being compact, modular and relatively inexpensive, the situation changes as larger power outputs are required. In these cases, due to their C-rate (rate required to completely discharge the maximum storage capacity in 1 hour) limited to 1-2 for large scale systems, batteries would have to be oversized in terms of energy storage in order to provide the required power, which increases their cost.

In SMES systems, however, a full discharge takes several minutes, at most, hence they typically store less energy compared to batteries, at the same power level. This characteristic suggests that at large scale, there is a power level beyond which SMES would make more economical and technical sense than equivalent large scale batteries. This issue is extremely complex and depends on numerous variables, such as economic and political environment, regulations on power systems, or future advancements in battery and superconductor technology. On the other hand, there are certain aspects regarding the methodology of designing SMES coils for high power applications, that have not been fully addressed in the literature and could potentially contribute to a better understanding of the role this technology could play.

Second generation high temperature superconductors (2G HTS) have shown performance improvements over industry-standard LTS wires, due to their higher operating temperature and critical current density in magnetic fields. This recommends them for usage in SMES systems, as cooling costs can be significantly reduced by eliminating the need for expensive liquid Helium. Nevertheless, SMES systems using these type of cables are not fully developed and understood and some issues still require further studies.

Firstly, there is the challenge of designing a large scale superconducting magnet, with storage capacity exceeding 1 MJ, while using the least amount of superconducting tape. While small scale units have been previously designed, as described in [34, 50–52], the methodology is either not clearly explained, or factors such as discharge power and magnetic forces are not taken into account. This thesis is aiming to address this gap by proposing a design methodology for a larger scale coil, which takes into account both the output power and the magnetic forces arising due to the high current circulating in the

coil. This would enable an easier direct comparison between SMES and other competing technologies, assessing key parameters, such as performance and cost.

1.6 Project Aim and Objectives

The main aim of this project is to propose a methodology of designing a SMES coil, which, besides the energy storage capacity, takes into account the required power output of the unit. The approach is using analytical expressions and numerical tables to derive the key parameters of a superconducting coil through an optimisation algorithm, which minimises the length of tape used. This enables a quick estimation of the performance and cost of the SMES coil, which can be used in comparisons against other high power storage systems, to determine which is more feasible for certain applications. Moreover, this is essential in studying the scale-up of SMES from a systems perspective.

In line with the objective, the aims of the project are:

1. To propose a design method for a large scale HTS SMES coil using analytical and numerical calculations, instead of computational Finite Element Modelling (FEM), in order to estimate the physical dimensions, the operating current and magnetic field, as well as the mechanical stress developed in the coil.
2. To develop an algorithm that generates coil configuration from a set of discrete input parameters, with the aim of minimising the length of superconducting tape used, given a target energy storage and output power level.
3. To analyse the operation of the designed coil as part of a simplified DC microgrid, when the typical DC-DC chopper topology from the literature is used. This is important for identifying the limitations of the chosen converter as the power demand is increased.

1.7 Thesis Outline

In line with the objectives set, the contents of the thesis are structured as follows:

- After the literature review covering the state of the art of SMES technology presented in Chapter 1, a more detailed theoretical background of superconductors and their applications in energy storage is given in Chapter 2. Through this, most of the theoretical concepts used in further chapters are introduced.

- In Chapter 3, a parametric coil design method that takes into consideration the energy and power is presented. Starting with the choice of commercial YBCO tape and an outline of its properties, the steps continue with the calculation of magnetic fields for different coil shape factors, which give the equations of load lines. The final design is obtained through discrete optimisation of shape factors and inner coil radius, with the objective of minimising the length of tape used.

- In Chapter 4, the coil design is introduced in a simplified DC microgrid model, to which is connected through a DC-DC chopper. Its operation is assessed under two different scenarios: a sudden spike in demand and sudden surplus of power.

- Finally, Chapter 5 draws the conclusions and outlines the a set of proposals for future work.

Publication

A. W. Zimmermann, S. M. Sharkh, "Design of a 1MJ/100kW High Temperature Superconducting Magnet for Energy Storage", *Energy Reports, Proceedings of the 4th Annual CDT Conference in Energy Storage and its Applications*, 9-11 July 2019.

Chapter 2

SMES Background

This chapter covers the theoretical background of SMES technology, starting with a brief introduction to the theory of superconductivity, followed by a classification of superconductors and overview of commercially available wires and tapes. The main characteristics of HTS tapes, along with the critical state models, are explained. Finally, practical aspects about the construction of the SMES system, including types of windings, insulation and the cooling system are presented.

2.1 Introduction to Superconductivity

Superconductivity was first observed in 1911 by Kamerlingh Onnes, a Dutch physicist working at Leiden University. Given by his successful liquefaction of Helium for the first time in 1908, he performed a series of tests of material properties at temperatures below 4.2 K. Remarkably, Onnes discovered that the electrical resistance of mercury (Hg) became zero at 3 K, thus marking the beginning of the superconductivity [74]. Over the following decades, as more elements and compounds were studied at low temperatures and found to be superconducting, some attempts were made at explaining the superconductivity phenomenon.

2.1.1 Meissner effect

In 1933, Meissner and Ochsenfeld discovered that a lead disc is expelling magnetic flux from its bulk once cooled below its transition temperature [75] (translated in [76]), as illustrated in Figure 2.1. This was important as it differentiated superconducting materials from perfect conductors, which, in theory, would maintain a constant magnetic field throughout their bulk at any temperature.

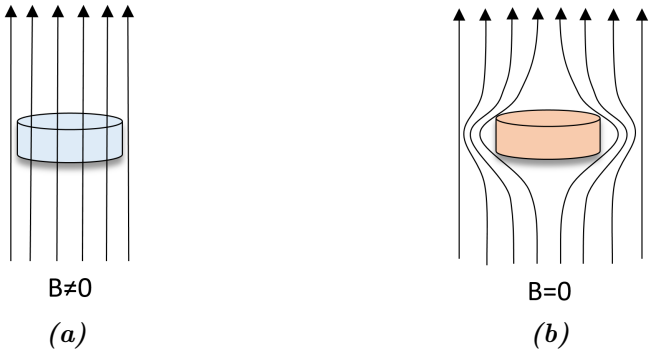

Figure 2.1: *Magnetic field lines in (a) normal and (b) superconducting states*

2.1.2 London Penetration Depth

In 1935, Fritz and Heinz London mathematically described how an external magnetic field penetrates through the skin of a superconductor, over a small length, given by:

$$\lambda_L = \sqrt{\frac{m}{\mu_0 n q^2}} \tag{2.1}$$

where m is the mass of charge carriers, q is the electron charge and n is the local density of superconducting carriers, which is a material property has the unit m^{-3}[77]. It was demonstrated by J.E.Hirsch that superconducting carriers can only be electron holes, with a method based on conservation of energy and momentum during a transition between superconducting and resistive states [78].

The penetration depth changes with temperature according to the relation:

$$\lambda(T) = \lambda_0 \left[1 - \left(\frac{T}{T_c}\right)^4\right]^{-1/2} \tag{2.2}$$

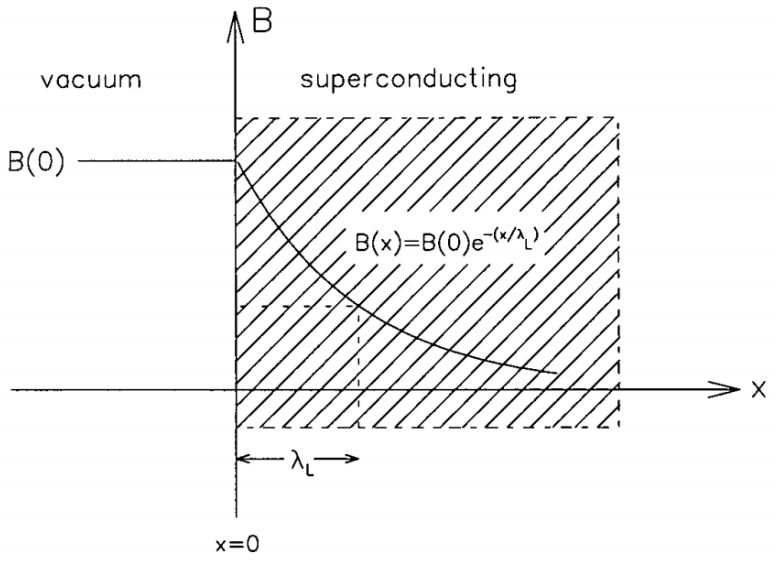

Figure 2.2: *Distribution of an external parallel magnetic field of magnitude $B(0)$ along the thickness of a superconductor. London penetration depth is the distance between the surface and the place in which the value of magnetic field reaches $B(0)e^{-1}$ [79]*

where λ_0 is the penetration depth at 0 K. When T approaches T_c, the penetration depth tends to infinity.

2.1.3 Type I and Type II superconductors

Further progress in understanding superconductivity was made by V. Ginzburg and L. Landau, who proposed a theory describing the transition between the normal and superconducting state, followed by A. Abrikosov [80], who extended the Ginzburg-Landau theory to explain the state transition in type II superconductors.

The transition from normal to superconducting state within a material occurs over a finite length, known as the coherence length, ξ_0. The Ginzburg-Landau parameter is defined as: $\kappa = \frac{\lambda}{\xi}$, where λ is the London penetration depth [81]. This is used to distinguish between type I and type II superconductors:

$$\begin{cases} 0 < \kappa < \frac{1}{\sqrt{2}}, & \text{for type I} \\ \kappa > \frac{1}{\sqrt{2}}, & \text{for type II} \end{cases}$$

In practice, the behaviour of type I and II superconductors is described through a **B-H** diagram as in Figures 2.3a and 2.3b.

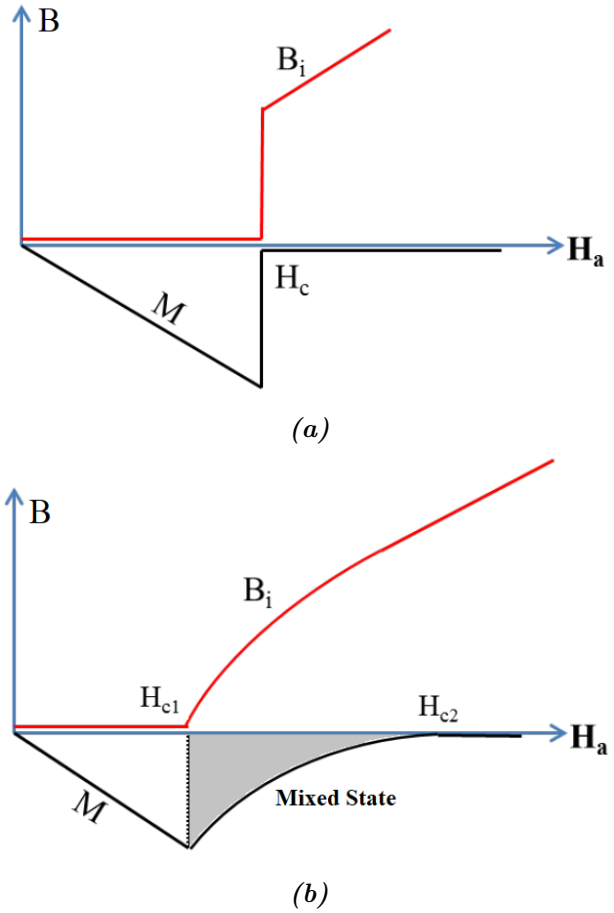

Figure 2.3: *Magnetization curves of (a) Type I and (b) Type II superconductors. Adapted from [82]*

The magnetic flux density, B, is expressed as:

$$B = \mu_0(H + M) \tag{2.3}$$

where H is the applied magnetic field intensity, M is the magnetisation and μ_0 is the magnetic permeability of vacuum. In the superconducting state, type I materials behave as diamagnets, thus $M = -H$ and $B = 0$. Beyond the critical field intensity, the flux density is sharply increasing to $B_\mathrm{i} = \mu_0 H$, after which it increases linearly.

In type II superconductors, a similar behaviour is seen below H_{c1}, the lower critical field intensity and above H_{c2}, the upper critical field intensity. However, the difference is in

the mixed state that appears between H_{c1} and H_{c2}, when the magnetization is slowly decreasing, while a non-zero flux density is present through the bulk.

In type I superconductors, represented by some elemental metals, such as Lead (Pb), Titanium (Ti) [83] or Aluminium (Al) [84], the bulk cannot be penetrated by external magnetic flux lines, therefore a sharp state transition is observed when the critical field is exceeded. However, in type II superconductors, there are two different critical field values, between which the material is in a mixed state, allowing some flux lines to penetrate the bulk. These flux lines are integral multiples of fluxons, quantums of magnetic flux, each with a magnitude of:

$$\Phi_0 = \frac{h}{2e} = 2.07 \times 10^{-15} \text{ Wb} \tag{2.4}$$

where h is Planck's constant and e is the electron charge [85]. Figure 2.4 shows the distribution of fluxons depending on the state, as a function of normalised magnetic field and temperature. Multiple fluxons are grouped in vortices, with a diameter of ξ_0, the coherence length. These are called Abrikosov vortices and, depending on the value of magnetic field, have a variable distribution and density through the material.

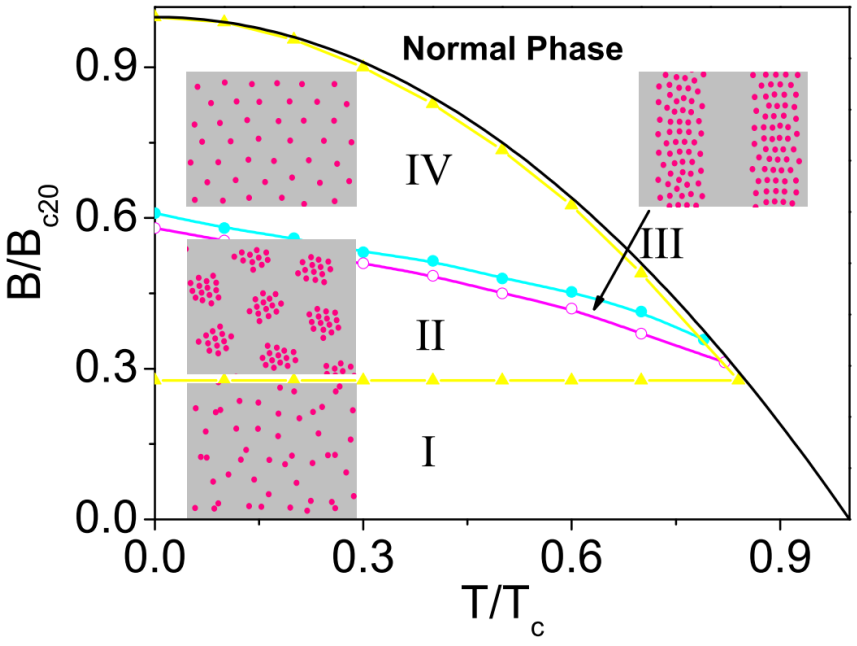

Figure 2.4: *Distribution of fluxons under different phases, as a function of temperature and magnetic field [86]*

At low values of magnetic field, vortices are irregularly distributed throughout the material, corresponding to phase I in Figure 2.4. As the magnetic field is increased, the vortices

regroup in bubbles and stripes, which correspond to phase II ($B = 0.43B_{c02}$) and phase III ($B = 0.59B_{c02}$), respectively [86]. A further increase in magnetic field leads to a regular distribution of vortices, in which the lattice spacing is inversely proportional to the field, effectively becoming zero at $B = B_{c02}$ [24].

This classification of superconductors is particularly important for determining which materials can be used in practical applications. When exposed to an external magnetic field, type I superconductors undergo and abrupt transition to resistive state, even when a small current is injected. On the other hand, type II superconductors can sustain large currents under external fields, making them suitable for tapes that can be used in SMES.

Another milestone in attempting to explain superconductivity was reached in 1957 by J.Bardeen, L.N.Cooper and J.R.Schrieffer, who proposed the BCS theory, for which they received the Nobel prize in 1972 [87]. Free electrons interact with the atom lattice by attracting nearby positive charges, thus causing a positively charged distortion, or a phonon. Consequently, this distortion attracts a nearby electron, binding with it and forming a Cooper pair (electron-phonon interaction). The binding force in the Cooper pair exceeds the resistance from the lattice, due to reduced vibrations at low temperatures, thus allowing it to pass through lattice with no resistance.

While further details are outside the scope of this project, it is interesting to notice that the theory predicted a maximum superconducting temperature of 40 K, which is well below the critical transition temperatures occurring in present HTS materials. Therefore, a clear explanation of superconductivity which applies to HTS is yet to be formulated.

2.2 Practical Superconductors

2.2.1 Timeline of practical superconductors

Following the discovery of superconductivity in Hg in 1911, more elements and compounds were found to be superconducting at critical temperatures $T_c < 40K$, thus being in line with the BCS theory. While most of the early superconductors were type I elemental metals, around the 1960s, compounds such as Niobium-Titanium (NbTi) and Niobium Tin (Nb_3Sn) were tested at low temperatures, showing the ability of carrying currents at

magnetic field densities exceeding 10T [88]. These were the first type II, low temperature (LTS) practical superconductors, which have been used extensively in manufacturing wires. BCS superconductors are represented by green circles in Figure 2.5, but are not used in the SMES design section of this project.

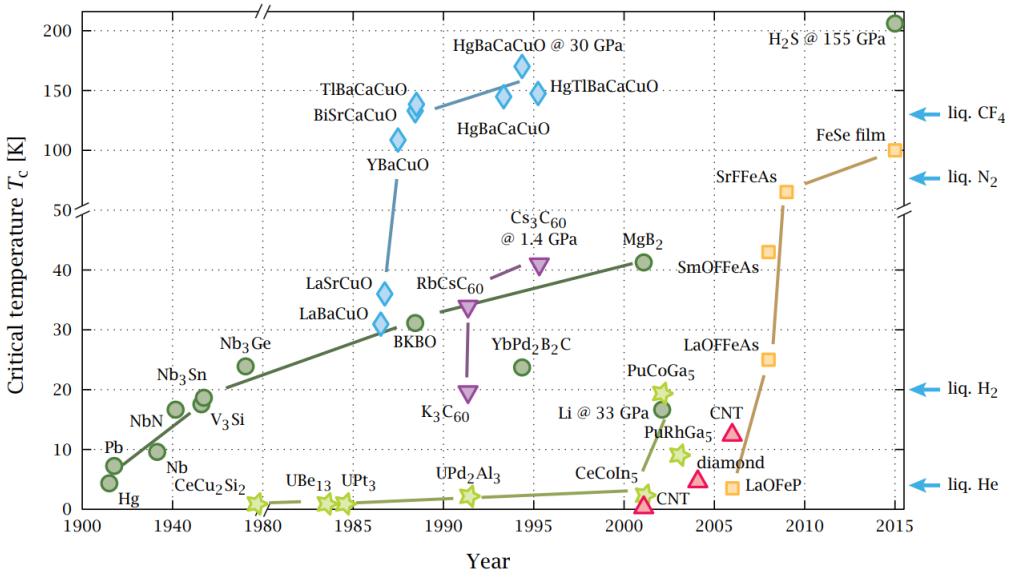

Figure 2.5: *The discovery timeline of major superconducting materials.* ***Green circles****: BCS superconductors,* ***Blue Diamonds****: Cuprates,* ***Yellow squares****: Iron-based superconductors [89]*

An important breakthrough was achieved with the discovery of superconductivity in certain cuprate compounds, in 1986. These have critical transition temperatures of over 80 K, placing them outside the scope of the BCS theory and marking the beginning of the high temperature superconductivity field (HTS) [90].

HTS materials present significant practical advantages over LTS, including the operation at higher temperatures, increasing the thermal stability and allowing the cooling to be realised through dry cryocoolers, as well as a higher current density under an external magnetic field [91]. As mentioned in Chapter 1, there are three cuprate compounds used in practical HTS superconductors: BSCCO 2212, BSCCO 2223 and ReBCO, represented as blue diamonds in Figure 2.5. During the past recent years, HTS materials have attracted increasing interest, as the manufacturing techniques have improved, increasing the commercial availability.

2.2.2 First and Second Generation HTS

The first practical HTS wires were manufactured in the late 1980s, using $Bi_2Sr_2CaCu_2O_8$ (Bi-2212) and $Bi_2Sr_2Ca_2Cu_3O_{10}$ (Bi-2223)[92]. While Bi-2223 has a higher critical temperature than Bi-2212 (110 K compared to 90 K), Bi-2212 can sustain higher critical current at sub-20 K temperatures. BSCCO wires are made using a similar technique as the one employed for LTS cables: powder-in-tube (PIT). In this method, the oxide mixture containing the superconducting compound is used in a powder form, filling a silver alloy tube. The tube is extruded and shaped in round Bi-2212 wires, which can then undergo further heat treatment and mechanical processing to obtain Bi-2223 tapes. Cross sections of Bi-2212 and Bi-2223 are presented in Figure 2.6.

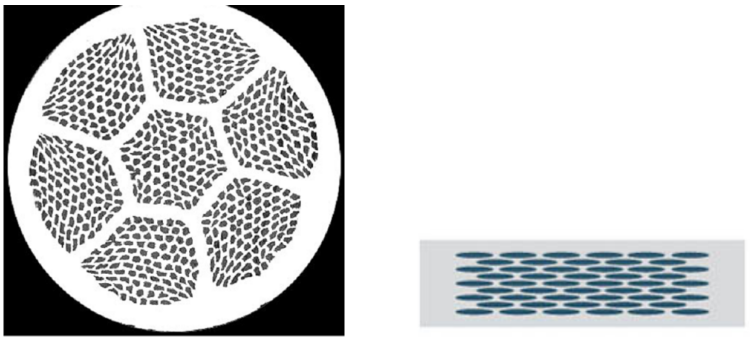

(a) *[92]* ***(b)*** *[93]*

Figure 2.6: *Cross section of (a) Bi-2212 round wire and (b) Bi-2223 flat tape*

Besides its role as electrical protection and structural matrix, a silver alloy is used as a sheath due to the high diffusivity of oxygen required during the reaction to Bi-2223, as well as due to it being inert to the superconducting powder [92]. Nevertheless, the two main disadvantages are the low mechanical strength, limiting the maximum strain to 250 MPa for an AgMg alloy [24], as well as the high material cost. As mentioned in Chapter 1, first generation (1G) Bi-based superconducting wires have successfully been used in SMES applications, with storage scales ranging from a few kJ, up to 1 MJ.

With improved critical current in external magnetic fields, second generation (2G) superconducting materials are based on REBCO, cuprates of rare-earth metals, such as Yttrium (Y), Strontium (Sr) or Gadolinium (Gd). Of these, the most popular compound used in making practical superconducting tape is $YBa_2Cu_3O_{7-x}$, often referred to as YBCO or Y-123. Practically, YBCO superconductors are manufactured using textured templated fabrication, in processes such as Ion beam assisted deposition (IBAD), Rolling assisted

biaxially textured substrates (RABiTS™) or Inclined Substrate Deposition (ISD)[24] . Several companies are producing 2G HTS tapes, including Bruker, American Superconductor Corporation (AMSC) and Superpower Inc. The cross section of an YBCO coated conductor, made by Superpower Inc. is shown in Figure 2.7.

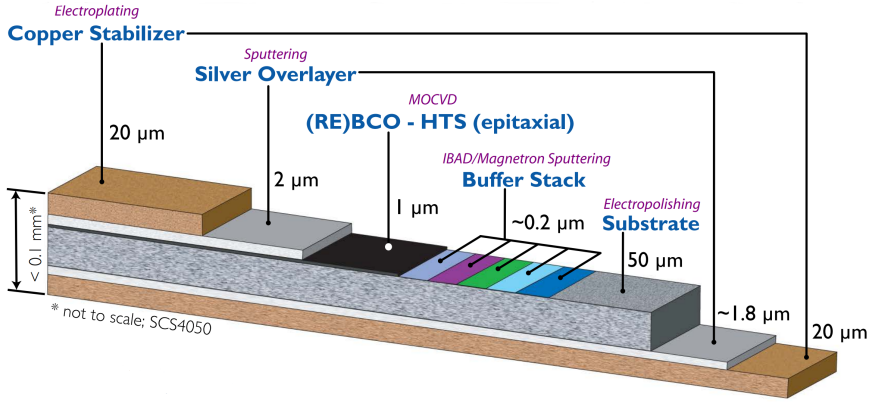

Figure 2.7: *Cross section of an YBCO coated conductor [94]*

A thin superconducting layer with a thickness of 1-2 μm is deposited on a buffer stack, which controls the superconductor grain alignment in an IBAD process, leading to a higher critical current density. This is followed by a Hastelloy substrate. This substrate increases the mechanical strength of the tape, while reducing AC losses due to its non-magnetic nature, as well as eddy current losses, due to its high electrical resistance. Silver is a good electrical conductor and does not react with YBCO, therefore it is used in a thin overlayer for making the electrical contact. At either side of the stack, a thick copper layer is used for additional stability, also acting as a parallel current path in case of quench [24]. While in superconducting state, the transport current only flows through the superconducting layer, facilitated by the lack of electrical resistance. However, if either the local temperature exceeds the critical value in a section of the tape, or there are mechanical defects, due to inhomogeneity or stress degradation, leading to a higher local current density, the magnet would transition to the resistive state. While in LTS this transition is sharp, in HTS it occurs slowly, with a longitudinal normal zone propagation velocity (NZPV) of 0.01-0.1 m/s, compared to 10-40 m/s in LTS [95]. As an effect, in HTS the current is shared between the superconducting layer and the copper stabiliser during quench, delaying any irreversible damage to the tape.

Finally, a relatively novel superconducting material was discovered in 2001 and has been intensively studied for power systems applications. Magnesium diboride (MgB_2) has a critical transition temperature T_c=39K, which is the highest value achieved by a non-cuprate superconductor [96]. Due to its simple structure, low anisotropy, good current density performance under magnetic fields and lower costs, MgB_2 has the potential for successful applications in SMES [97]. Given its critical temperature of 39K, MgB_2 can be classified as a Medium Temperature Superconductor (MTS).

Considering their better thermal stability, higher critical temperatures, in excess of 90 K, giving a larger operating margin compared to LTS, as well as the high critical current density at low fields, with values of up to 1000 MA/m^2 at 20K, in fields of under 13 T [24] , the SMES magnet in this project will be designed using HTS tapes.

2.2.3 HTS Anisotropy

HTS tapes have a high degree of anisotropy, which affects the value of critical current. Firstly, the orientation of grain boundaries within the crystallographic structure of the superconductor affect the current flow. Even slight misalignments between the grain boundaries and the current flow direction can cause significant drops in the critical current value, which is why the alignment of the crystallographic axes must be strictly controlled during manufacturing, to ensure a uniform current distribution along the entire conductor length [24].

Secondly, HTS tapes are also anisotropic under external magnetic fields. When the field direction is perpendicular to the c-axis, the critical field reaches its peak value. As the angle between the field direction and the c axis is gradually reduced, the critical current drops. Figure 2.8b illustrates the critical current density as a function of temperature, for different external fields and under different angles. It can be observed that the critical current drops with the angle between the field lines and the c-axis at any flux density [98].

In practice, the effect of anisotropy must be considered when designing the SMES coil. At either end of the coil, the direction of magnetic field changes from parallel to the central coil axis, to perpendicular, in a radial distribution. As a consequence, the angle between the field lines and the c-axis of the crystallographic plane in the superconductor reduces from 90° to 0°, thus reducing the maximum critical current that can be sustained. To avoid

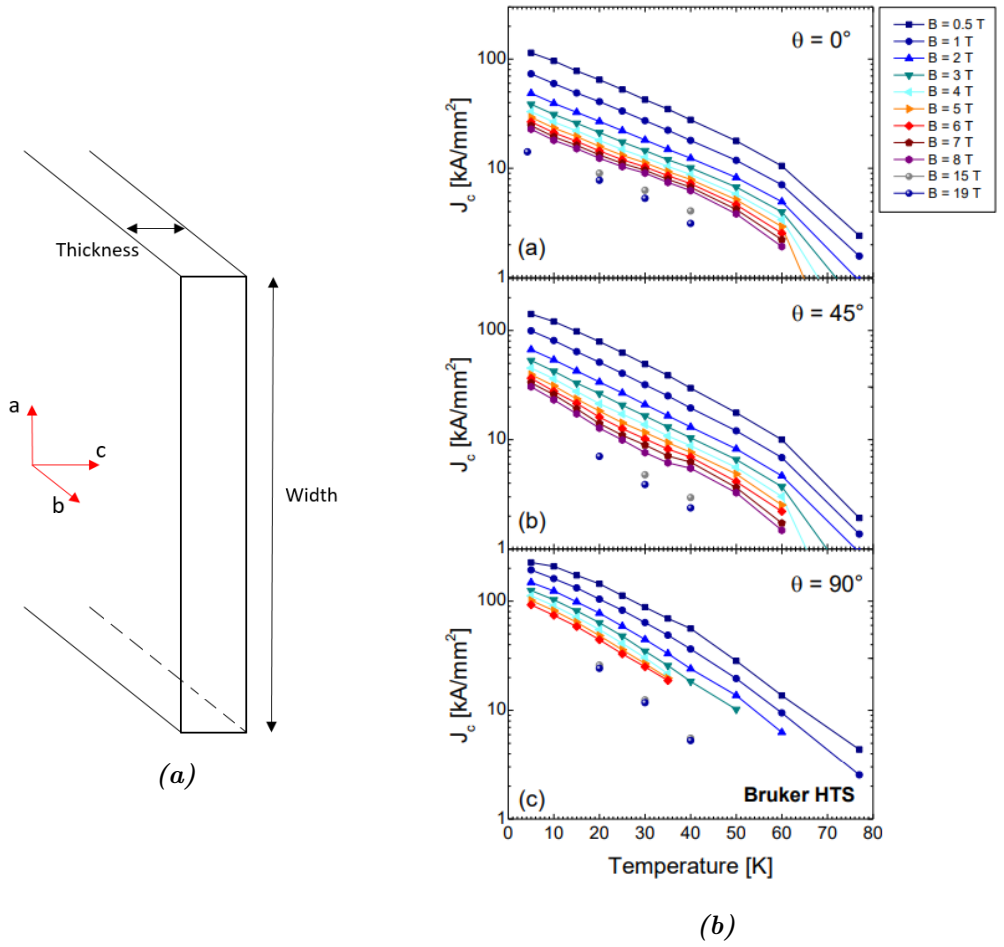

Figure 2.8: *(a) Direction of crystallographic axes relative to the tape dimensions in ReBCO superconductors; (b) Dependency of critical current density on temperature, magnetic flux density and direction relative to the c-axis of the crystallographic ReBCO structure in a Bruker HTS tape [98]*

quench, the transport current needs to be limited below the critical value in perpendicular field, assuming that all the turns in the coil are connected in series.

Due to high anisotropy, one of the main goals in 2G HTS tapes manufacturing is to increase the critical current in magnetic fields perpendicular to the tape width (parallel to the c-axis). This has been achieved in tapes with thicker layers of GdYBCO (4.3-4.6 μm, compared to the usual 1-2 μm), doped with Zr. These tapes have achieved engineering critical current densities J_e (total current in tape divided by the entire tape area) of over 5 kA mm^{-2} at 4.2 K and 14 T, comparable to the performance of thin film tapes at the same temperature and field, but with the field parallel to the tape width [99].

A way of increasing the transport current in a SMES unit is by using Roebel cables, which consist in multiple superconducting tapes isolated between each-other and transposed with

a certain pitch. This practice has been widely applied in electric machines, in order to reduce eddy current losses [100], which are explained in Section 2.4.

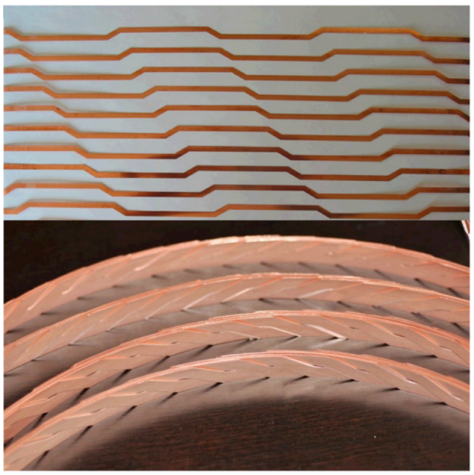

Figure 2.9: *Structure of Roebel YBCO cables [100]*

This technique requires cutting the tape using a punching tool, effectively reducing its width by half. As a consequence, the overall current density of the resulting Roebel cable is typically between 30 and 60 % lower than the sum of critical current densities in each individual tape [24]. Cables with a critical current of up to 2628 A at 77 K and self field have been produced, using 15 stacks of 3 tapes each [101]. While the Roebel cable has a significant improvement in critical current over a single tape, which can only sustain up to 149.5 A, it suffers from a degradation of 61 %, compared to the total critical current of the 45 tapes connected in parallel.

2.3 Critical State Models

Critical state models attempt to establish a relation between the critical current density and the external magnetic field in a superconducting tape. These can be used in finite element modelling and analysis (FEM, FEA) for calculating the distribution of current density along the tape dimensions, the forces, as well as the heat dissipation due to AC losses.

2.3.1 Bean model

The first critical state model was proposed by Bean in 1964 [102] and is based on the assumption that the transport current can only take two values across the tape width, depending on the magnetic field penetration depth. This model considers a thin superconducting slab in parallel external field, as depicted in Figure 2.10. Depending on the field intensity, the slab is penetrated over a finite distance, where the current density reaches the critical value, J_c.

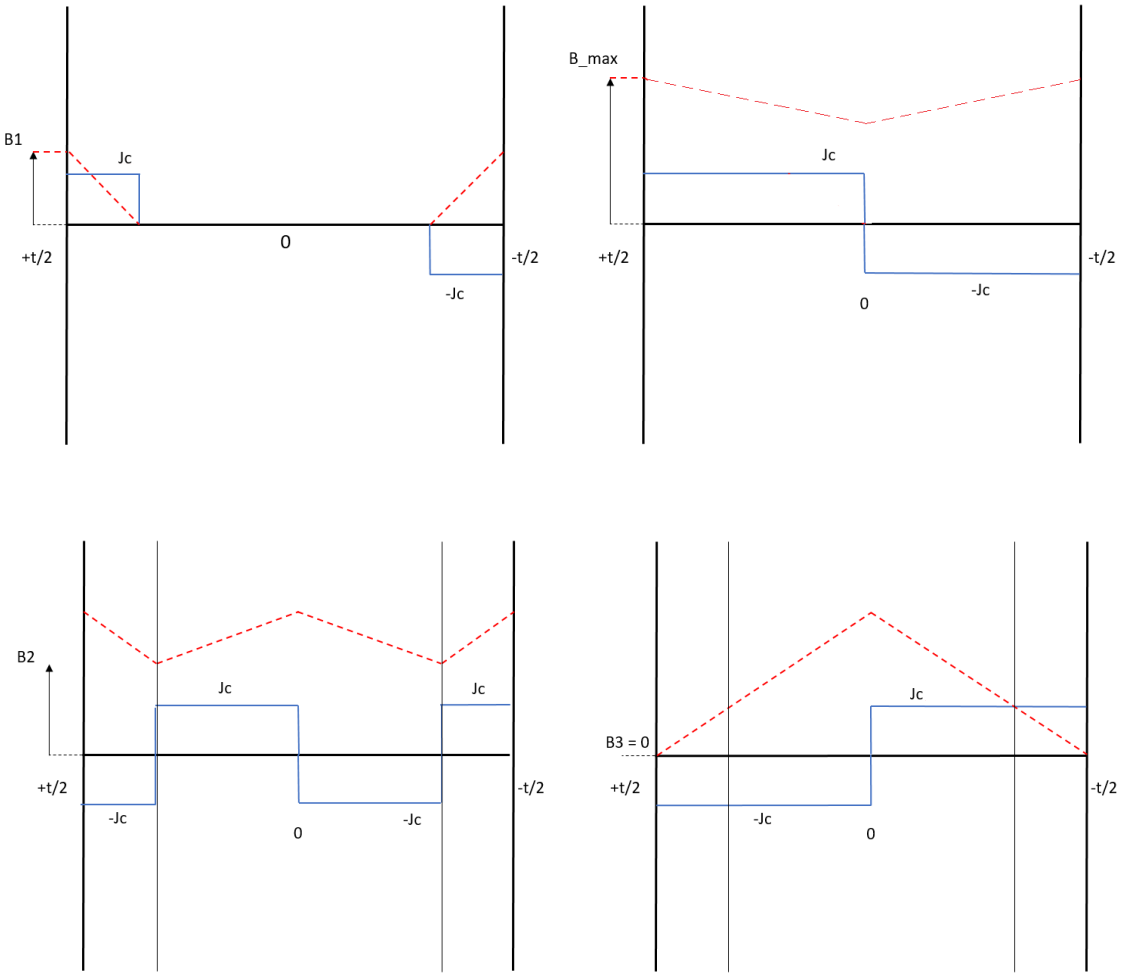

Figure 2.10: *Current density across the tape width under changing external fields according to Bean's model*

According to Ampère's law in a 1D case, the change of in flux density along the slab can be expressed as:

$$\frac{dB}{dx} = \mu_0 J(x) \tag{2.5}$$

In the penetrated regions, the field is linearly decreasing to 0, as $J(x) = \pm J_c$, while in the shielded regions, $J(x) = 0$, so the field remains null.

2.3.2 Kim model

The model proposed by Kim et al. [103] assumes that the value of critical current changes along the width of the slab, depending on the penetrating field intensity, according to the scaling law:

$$J_c(B) = \frac{J_{c0}(T)}{1 + k|B|} \tag{2.6}$$

Here, $J_{c0}(T)$ is the critical current density under no external field at the operating temperature and k is a constant depending on the material.

The model was also adapted to account for anisotropy in HTS tapes [104], taking the form:

$$J_c(B_\parallel, B_\perp) = J_{c0} \cdot \left(1 + \frac{\sqrt{k^2|B_\parallel|^2 + |B_\perp|^2}}{B_0}\right)^{-\alpha_0} \tag{2.7}$$

Here, $B_\parallel$ and $B_\perp$ are the parallel and perpendicular components of the magnetic field, respectively; while B_0, α_0, and k are material constants.

2.3.3 E-J Power law

When type II superconductors are in the mixed state, the vortex lattice is formed, consisting in fluxons bundled cores. Flux lines perpendicular to the current flow direction are subject to Lorentz forces, which move the vortices through the material [24]. This phenomenon, known as 'flux creep' [105], generates an electric field, inducing pseudo-resistive losses in the superconductor and degrading its critical current performance. To reduce this effect, flux pinning sites are created in HTS during the manufacturing process, by introducing defects on the crystal lattice of the superconductor layer. As long as the pinning force exceeds the Lorentz force, no flux creep occurs.

Proposed by Rhyner et al.[106], the power law is a scaling relation enabling the calculation of the generated electric field in terms of the transport current density. It has the form:

$$E = E_c \left(\frac{J}{J_c}\right)^n \tag{2.8}$$

where E is the electric field at a current density of J, E_c is the electric field criterion and J_c is the critical current density. The exponent, n, is a material constant, with typical values of 20-30 for HTS and exceeding 40 for LTS [107]. In resistive materials, $n = 1$.

To define the critical current density value, the electric field criterion is used. It is generally accepted that the critical current density is obtained when the electric field measured in the tape reaches $E_c = 1\mu V/cm$, although a stricter value of $E_c = 0.1\mu V/cm$ was also employed [108].

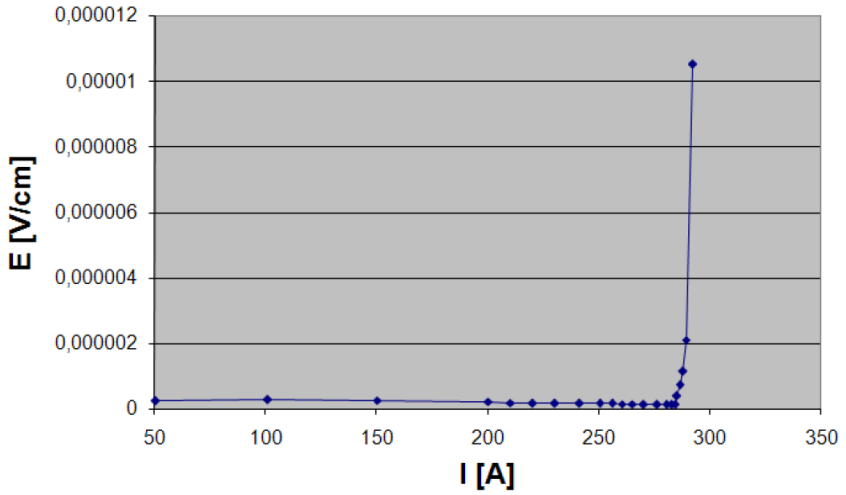

Figure 2.11: *Power law in YBCO tapes [109]*

As the resistivity of the tape is related to the electric field and current density through Ohm's law: $E = \rho J$, equation 2.8 can be rewritten as:

$$\rho = \rho_c \left(\frac{J}{J_c}\right)^{n-1} \simeq \rho_c \left(\frac{J}{J_c}\right)^{n} \tag{2.9}$$

This is useful for expressing the resistivity of the tape as the transport current density approaches the critical value.

2.4 AC losses

In order to determine the cooling power necessary to maintain a SMES unit at the suitable temperature, it is important to identify the sources of energy loss during the operation. While the transport current is DC, its magnitude changes with the state of charge of the magnet, causing the self field to vary. This leads to AC losses in the magnet, which are

dissipated as heat and are generally made up of magnetic hysteresis, eddy current and coupling current losses [110]. Besides the resistive losses from solder joints, current leads and power electronic converters, AC losses are important sources of inefficiency in a SMES system.

For simplifying the calculation of AC losses, there are two important assumptions that must be made. The first one is related to coupling losses, which are given by the circulation of currents in the resistive metallic path surrounding superconducting filaments, due to a change in external magnetic field. Since 2G HTS tapes used in SMES only consist of a single layer of superconducting material, as opposed to a multi-filamentary structure, coupling losses will be neglected.

The second assumption is related to eddy current losses. When the magnetic field is perpendicular to the tape, eddy currents opposing the direction of this field are induced in the metallic skin of the tape, creating joule heating [111]. In SMES, there is no applied alternating magnetic field, however the self field induced due to the transport current is changing at a constant rate during discharge. However, analysing AC losses in a superconducting coil is outside the scope of this project.

2.5 Magnet Winding and Optimisation

There are two main types of superconducting magnet winding configurations: the solenoid and the toroid. In the solenoid, superconducting tape is wound helically on a cylindrical former, resulting in a multilayer, multi-stack air-cored coil. In a toroid, a similar approach is used, winding the tape on an air-cored toroidal former.

Due to the difficulty in manufacturing long lengths of 2G HTS tapes with homogeneous properties, it is more practical to build the SMES coil by stacking multiple single or double pancake coils. In this way, a better control on the performance of the tape is achieved, as each pancake coil can be individually tested to ensure it meets the standards. In single pancake coils, one end of the tape is inside the winding, while the other end is outside of it, which makes it more difficult to connect multiple coils in series. On the other hand, double pancake coils, as shown in Figure 2.13 have both ends outside of the coil, making

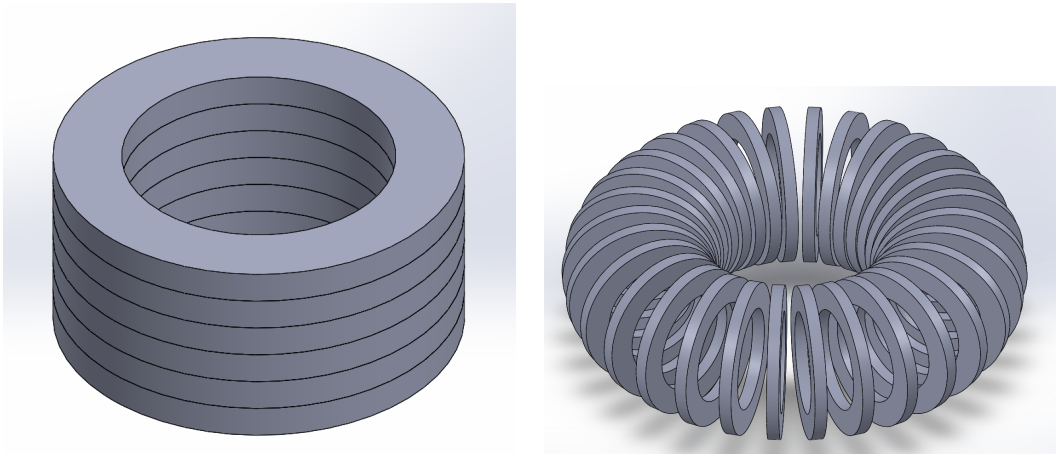

(a) *(b)*

Figure 2.12: *SMES coil configurations: (a) Solenoid configuration, (b) Toroid Configuration*

it easier to connect consecutive modules through joints. Double pancake coils can be used in both solenoid and toroid configurations and confer SMES magnets a certain degree of modularity.

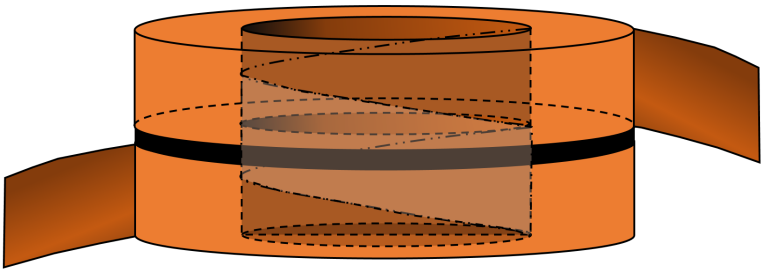

Figure 2.13: *Diagram of double pancake coil*

A main advantage of the toroidal configuration over a solenoid is the reduction of stray field, as the lines are effectively trapped inside the coil bulk. Nevertheless, when it comes to energy storage density, solenoidal configurations are far superior, as proven in different studies [112, 113]. Simulations of both configurations with four different HTS tapes were run and the results indicated that for the same length, a solenoid stored at least twice the energy compared to a toroid [113].

Besides solenoidal and toroidal coils, which have circular cross sections, other types of coils were proposed. These include double toroidal and n-poligon groups, both made with sections with a D-shaped cross section [114]. However, it is expected that the manufacturing of these would be more challenging and was not detailed in the literature.

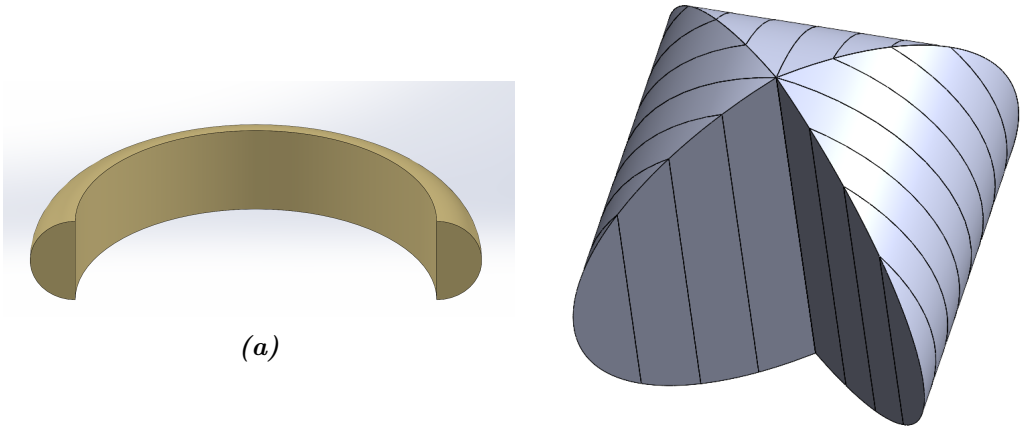

(a) *(b)*

Figure 2.14: *Different types of coils (a) D cross-setion, (b) N-polygon with N=4*

To balance the forces in toroidal coils, effectively increasing their energy storage capabilities, tilted-toroidal coils were suggested [115]. In such configuration, the pancake coils are tilted by certain angles around the vertical and radial axes, leading to an overall reduction of electromagnetic forces.

2.6 Refrigeration and Quench Protection

2.6.1 Refrigeration for superconducting magnets

Given the large difference between the operating temperature of a superconducting magnet and ambient temperature, which can be as high as 290 K, adequate cooling is essential within a SMES system. AC losses in the system, dissipated as heat, must be efficiently removed to prevent temperature from rising inside the dewar.

There are two main types of cryogenic systems: wet and dry. In a dry system, heat generated by the coil is removed through a highly conductive metallic plate, hence the name of conductive cooling. The magnet is kept in vacuum, inside a dewar. In a wet system, the superconducting magnet is submerged in a pool of cryogen, which typically consists of a liquefied gas. Depending on the operating temperature, the choice of cryogen can be liquid Helium ($T_{boil} = 4.2K$), liquid Hydrogen ($T_{boil} = 20K$), liquid Nitrogen ($T_{boil} = 77K$) and liquid Oxygen ($T_{boil} = 90K$). The heat generated by the magnet is

absorbed as latent heat by the cryogen, causing it to boil-off. To maintain the SMES below its critical temperature, the cryogen bath can either be topped up periodically, making it an open system, or a cryocooler can be used to continuously remove the generated heat and reliquify the cryogen, in a closed systems. The latter is preferred, as less interaction is required with the system.

While LTS magnets with critical temperatures of under 10K can only operate in liquid Helium, HTS materials are suitable for usage in liquid Nitrogen with limited performance, given the high temperature, or liquid Hydrogen, with significantly improved performance. This is a significant advantage of HTS tapes, as the operation cost is reduced.

2.6.2 Cryocoolers: Types and operation

Cryocoolers are based on refrigeration cycles, using a working fluid, which is typically Helium, Neon or Argon [116], to remove excess heat from a cold reservoir and reject it to the surrounding medium. Within the cycle, a compressor is used to increase the pressure, hence the temperature of the working fluid, which is then condensed, releasing the absorbed heat to the surroundings. The fluid is then cooled through a heat exchanger and passed through an evaporator, reaching a temperature below the one of the cold medium [24].

The coefficient of performance of the cycle is given by:

$$COP = \frac{\dot{Q}_c}{\dot{W}_c} \tag{2.10}$$

where $\dot{Q}_c$ is the heat flow absorbed from the cold reservoir and $\dot{W}_c$ is the net input power for the cycle, the sum between the power necessary to drive the compressor and the output power given in the expansion. Every real system can be benchmarked against the ideal (Carnot) system, working between the same cold (T_c) and hot (T_h) temperatures. The Carnot COP is given by:

$$COP_{Carnot} = \frac{T_c}{T_h - T_c} \tag{2.11}$$

thus the efficiency of a real refrigeration system can be expressed as [116]:

$$\eta = \frac{COP}{COP_{Carnot}} \tag{2.12}$$

For a constant hot reservoir temperature of 300K, the COP_{Carnot} for a system with a cold reservoir at 77K is 0.345, more than 24 times greater than the value for a cold reservoir temperature of 4.2K, showing a clear advantage for HTS in terms of cooling costs.

There are two major types of cycles used in cryocoolers: recuperative and regenerative. In recuperative cycles, the working fluid flows in a single direction, with separated high and low pressure streams. Heat is transferred from the high pressure to the low pressure line through a heat exchanger. This method is used in Joule-Thomson (JT) and Brayton cycles, illustrated in Figure 2.15. While these cycles are largely similar, the difference comes at the gas expansion stage, which is realised through an expansion valve in the JT cycle and with an expansion turbine in the Brayton cycle.

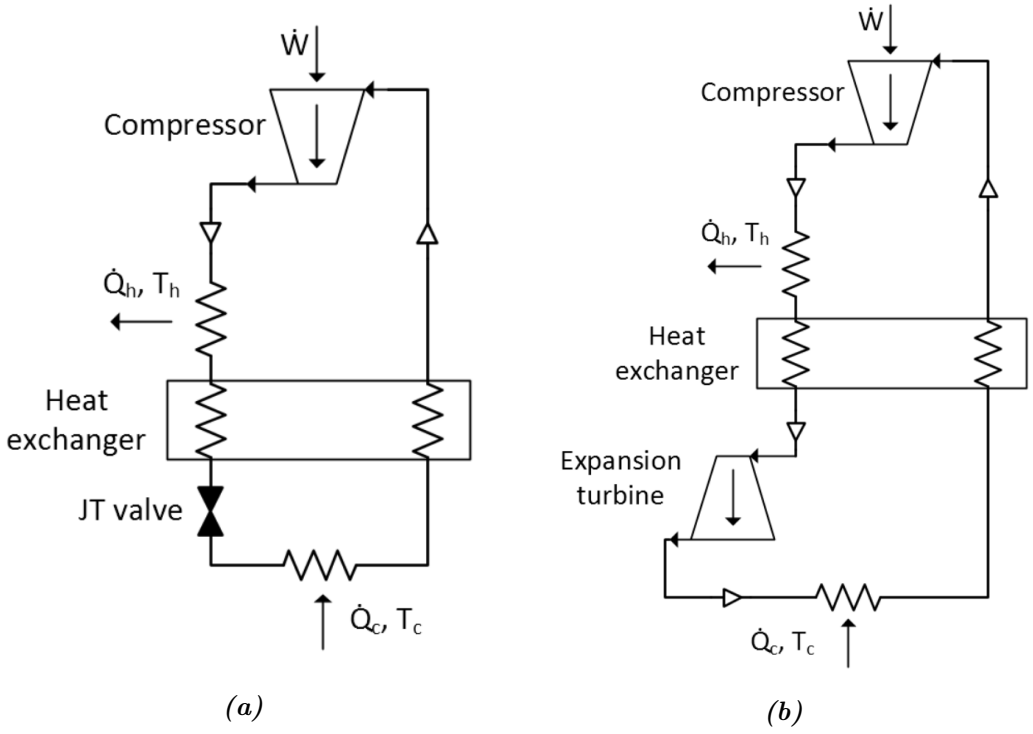

Figure 2.15: *Recuperative refrigeration cycles: (a) Joule-Thomson, (b) Brayton. Figures adapted from [116]*

Contrary to recuperative cycles, steady high and low pressure levels are maintained throughout the cycle, regenerative cycles are based on oscillations of pressure. A key component of regenerative cycles is the regenerator, a solid porous material that increases the contact surface area with the gas and has high heat capacity.

Both Stirling and Gifford-McMahon cycles have the same operation at the cold head. In the high temperature side, Helium is compressed isothermally, giving away heat to

the surrounding at T_h. The gas then is passed through the regenerator, reducing its temperature from T_h to T_c, the latter being the temperature of the cold head. To remove heat from the cold environment, the gas is then expanded isothermally, maintaining its temperature and absorbing Q_c. It then goes back through the regenerator and the cycle is repeated [117].

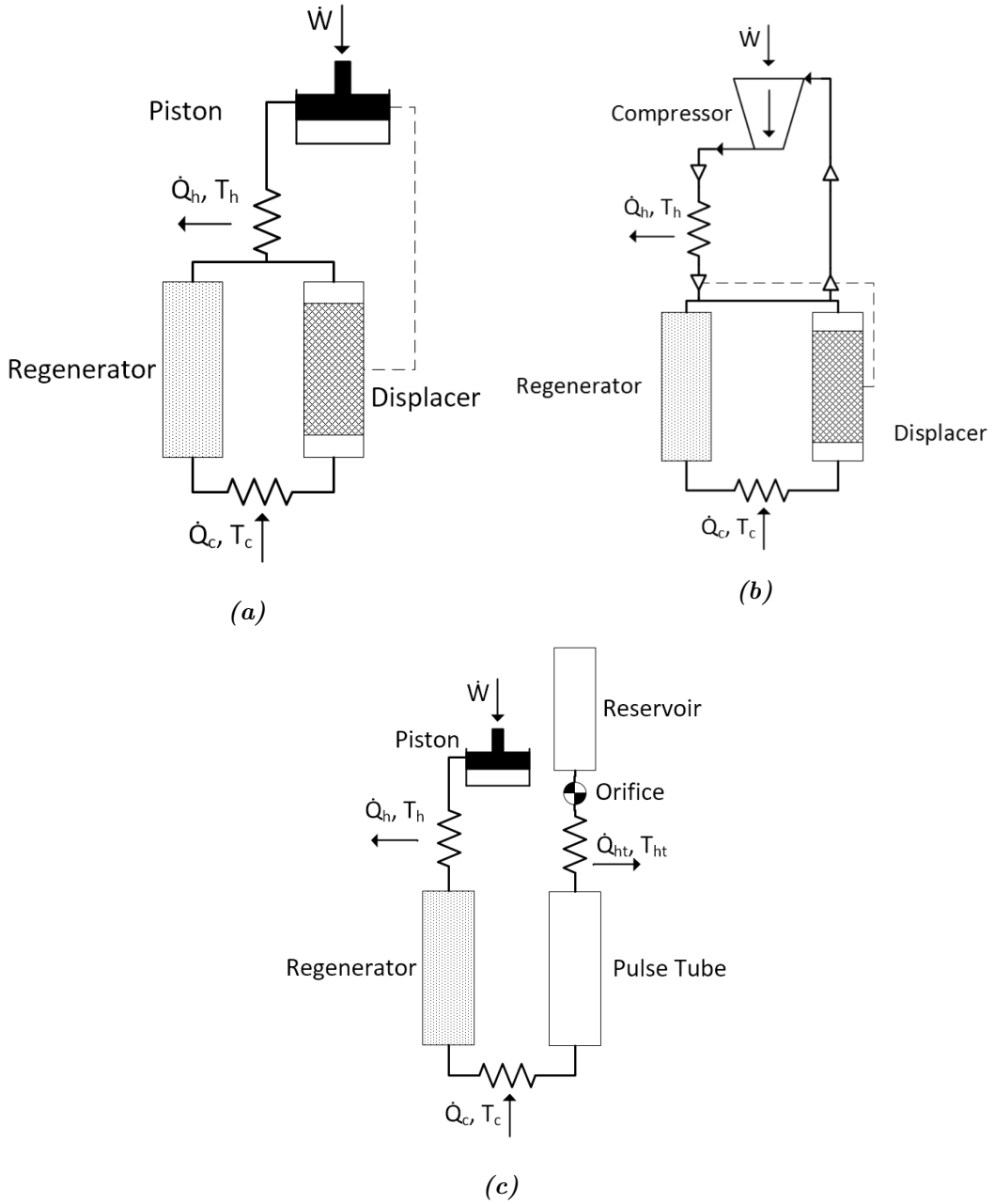

Figure 2.16: *Regenerative refrigeration cycles: (a) Stirling, (b) Gifford-McMahon, (c) Pulse-Tube. Figures adapted from [116]*

While in a Stirling cycle, the movement of the compressor and displacer pistons is harmonic, with the displacer leading by 90°, in a GM cycle these movements are decoupled. This is achieved by alternatively coupling the cold head to the low and high pressure ducts of a compressor by the means of a rotating valve.

In a Pulse-Tube (PT) cycle, depicted in Figure 2.16c the compressor piston moves down, compressing the fluid and forcing it through an orifice in the reservoir, where it exchanges heat with the surroundings. This happens until the pressure difference between the reservoir and the tube becomes zero. After this, the piston moves up, expanding the volume of the fluid and reducing its temperature. As the pressure in the pulse tube is now lower than in the reservoir, Helium will flow from the reservoir into the pulse tube until the pressures equalise. This stage removes heat from the cold head through the heat exchanger. Effectively, there are three distinct volumes of fluid within the PT: one on the hot end that enters and exists the reservoir, one in the middle that would stay inside the tube and act as a thermal gradient between the cold and hot end, as well as one at the cold end, that removes heat from the cold head [116].

Table 2.1: *Summary of Cryocoolers*

Refrigeration cycle	Type	Advantages	Disadvantages
Joule-Thomson	Recuperative	• Non-moving parts at cold end • Can be used in miniature devices (e.g. infrared sensors) • Fast cool-down	• Low efficiency • Requires two stages for cooling below 70K • Requires high pressures (>20 MPa)
Brayton	Recuperative	• Higher efficiency than JT • Requires lower pressure	• Difficult to manufacture expansion turbines for small systems
Stirling	Regenerative	• Long lifetime of displacer, given by low oscillation frequency (1-2 Hz)	• Slow cool-down
Pulse-Tube	Regenerative	• No moving parts at cold end • Most efficient of cryocoolers	• Convective instabilities occurring if cold head is up or horizontal • Not suitable for applications with less than 10 W input power.
Gifford McMahon	Regenerative	• Less expensive than PT • Compressor can be located separately to the cold head, reducing vibrations	• Reduced displacer lifetime due to high oscillation frequency (30-60 Hz)

As the required temperature decreases, so does the efficiency of cryocoolers. In small systems, with a cooling power of less than 10 kW, this can barely exceed 20% of the Carnot efficiency at 80 K, dropping below 5% at temperatures under 10 K [118]. To increase its efficiency, the cooling process is typically done in two stages.

Table 2.1 gives an overview of cryocoolers, along with their advantages and disadvantages. Further detail on cryocoolers design is out of the scope of this project.

2.6.3 Quench Protection

In a SMES unit, quench occurs when the magnet undergoes a transition from superconducting to resistive state. This can happen when either the current density, the temperature, or the magnetic field exceed the critical values during operation. Due to the rise in electrical resistance, ohmic losses occur in the cable, further increasing the temperature. Because of low margins between the operating and the critical temperature, LTS magnets have a much faster quench propagation speed, which, at high transport currents, can cause significant damage. On the other hand, given the high temperature margin, the quench in HTS magnets can often be detected and prevented.

Detailed studies of quench propagation have been carried in superconducting tapes [119–121], showing that the propagation velocity can exceed 200 m/s at high fields. Hence, a continuous monitoring of temperatures and voltages at different points in the coil is necessary, along with a quench protection circuit with a fast response time. This usually consists of a power switch and a metal oxide varistor (MOV), both connected in parallel to the SMES unit. The MOV is capable of effectively suppressing transient voltage, making a suitable protection circuit in case of quench.

Ultimately, if the quench cannot be prevented during operation, damage on the superconducting layer can be prevented through the inclusion of an alternative conduction path, which consists of a Cu layer or matrix, as explained in section 2.2.2. All practical superconducting cables include an such conductive layer, typically Ag in BSCCO and Cu in YBCO. In case of quench, part of the current would flow through this path, effectively decreasing the current density across the superconducting layer and preventing damage.

Chapter 3

SMES Magnet Design

In order to study the scale-up of SMES systems, it is essential to understand how changing the geometry influences electro-magnetic parameters, such as inductance, transport current and magnetic field, as well as the required length of superconducting tape. This can inform the electrical model of a SMES in a circuit, as well as help approximate the costs incurred by such a system as the requirements change. This chapter outlines the parametric design methodology for a HTS magnet that can be used in a SMES system, with the primary goal of minimising the length of superconducting tape used for a set quantity of deliverable energy. The method is applied to the design of a magnet capable of delivering 1 MJ of energy at a rate of 100 kW.

3.1 Methodology

3.1.1 Initial assumptions

In SMES applications, the main goal is to maximise the energy stored per unit length of superconducting tape. This can be done either by maximising the storage capacity for a given length of superconductor, which is typical in lab-scale projects relying on limited budgets [49, 50], or by storing a target quantity of energy while minimising the length of superconducting tape. The latter approach is typical in large scale projects and will be used in this chapter, as it will aid in scaling the magnet to large storage capacities, in excess of 10 MJ.

As no comprehensive Finite Element Analysis (FEA) packages have been developed for simulating superconducting behaviour, the design methodology outlined in this project is based solely on analytical expressions and numerical tables.

The cross section of the superconducting tape is assumed rectangular, with a width w and a thickness t, as depicted in Figure 3.1.

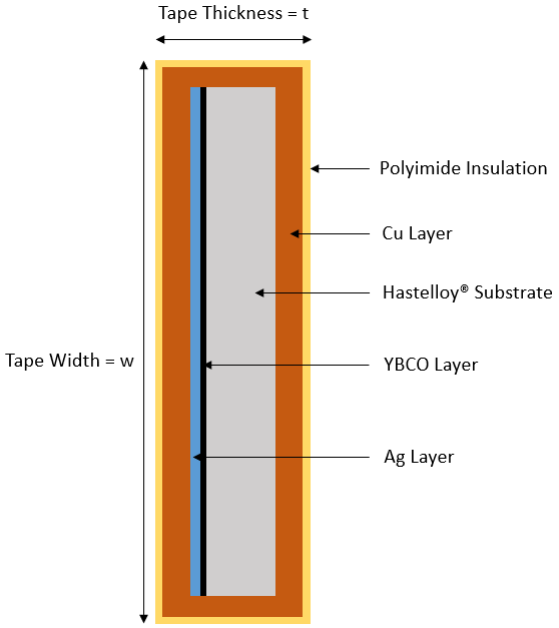

Figure 3.1: *Diagram of YBCO tape layers and dimensions*

As a solenoidal coil can store more energy than a toroidal configuration, with the same quantity of material [113], it is the preferred configuration in SMES. This makes the construction of the magnet simpler, as it only requires stacking several double pancake units axially and connecting them in series, as presented in Figure 2.12a form Section 2.5. A cross section of a double pancake coil is presented in Figure 3.2.

Assuming that the wider face of the tape is parallel to the central axis of the solenoid, the height of the solenoid is proportional to the number of stacked double pancakes and is denoted by $2b$. Similarly, the thickness of the solenoid, denoted by c, is given by the difference between the outer and the inner radii $(R_o - Ri)$ and is the thickness of an individual tape, including insulation, multiplied by the number of tapes in a layer. For added structural strength and thermal conductivity, the coil is generally impregnated with epoxy, leading to a typical fill factor of $f = 0.75$, the ratio between the total cross-sectional area of the tapes, including insulation[112]. The minimum inner radius of the pancake must

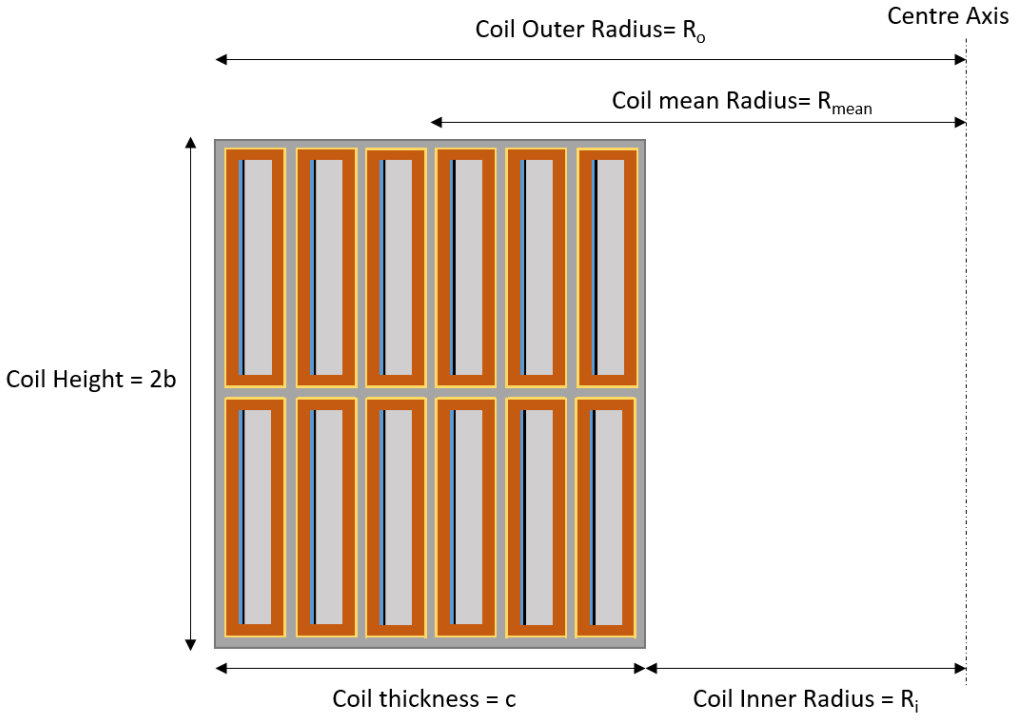

Figure 3.2: *Cross section of a 6 layer double pancake made with YBCO tape*

be at least equal to the minimum bending radius of the selected tape, in order to prevent the degradation of critical current [122].

To assess the suitability and performance of a tape, it is necessary to determine the relation between critical current and magnetic field. Based on the discussion in Section 2.2.2, 2G HTS tapes are considered in this design, due to their high critical temperature of over 90 K, good thermal stability and high critical current, which can exceed 300A in a 12 mm wide tape at 77K and self field [94]. At either end of the solenoid, the direction of magnetic field changes from being parallel to the central axis of the coil, to being perpendicular to it, and hence, to the tape. Due to their high anisotropy, perpendicular magnetic fields will have a larger effect to the critical current of the tape than a parallel field, effect which is observed in the critical curves plotted for parallel and perpendicular field directions in Figure 2.8b. It is common practice in the design process of magnets using highly anisotropic tape to only consider the critical curve for a perpendicular field direction, as it gives lower values of critical current, ensuring the superconducting state is maintained [34, 49, 50, 123].

From a geometrical perspective, a solenoid can be fully defined using three parameters: its internal radius, R_i, its height and its thickness. To further simplify the calculations,

the latter two are expressed in terms of the inner radius through shape factors α and β, so that:

$$R_o = \alpha R_i \tag{3.1}$$

$$H = 2b = 2\beta R_i \tag{3.2}$$

$$R_{mean} = \frac{R_i + R_o}{2} = \frac{\alpha + 1}{2} R_i \tag{3.3}$$

$$c = R_o - R_i = (\alpha - 1) R_i \tag{3.4}$$

Using equations 3.1 and 3.2, the following useful quantities can be expressed in terms of α, β and R_i:

$$\text{Length of superconducting tape: } l = \frac{2\pi f(\alpha^2 - 1)\beta R_i^3}{tw} \tag{3.5}$$

$$\text{Number of turns: } N = \frac{2f(\alpha - 1)\beta R_i^2}{tw} \tag{3.6}$$

$$\text{Inner volume of the coil: } V_i = 2\pi\beta R_i^3 \tag{3.7}$$

$$\text{Outer volume of the coil: } V_o = 2\pi\alpha^2\beta R_i^3 \tag{3.8}$$

3.1.2 Outline of design methodology

The flowchart diagram in Figure 3.3 illustrates the steps taken for designing the superconducting magnet. Given the combination of analytical expressions and numerical tables, the algorithm used in this methodology is a constrained discrete optimisation. Based on a set of input constraints, the algorithm calculates key parameters, such as the coil inductance, stored energy, critical curve current and load line current. If the set of parameters produces a coil configuration that satisfies a series of conditions, such as the stored energy being at least equal to the required value, while the stress is below the limit, the set of parameters is compared to the minimum values (which are either provided initially, or saved in the previous iteration). The optimisation objective is to minimise the amount of superconducting tape used in the coil design. If a set of parameters leads to a lower quantity of superconductor used, that set is saved as the minimum. The algorithm then proceeds to the next set of parameters, until the iteration over all intervals is finalised. Once this is complete, the final configuration of the coil is printed.

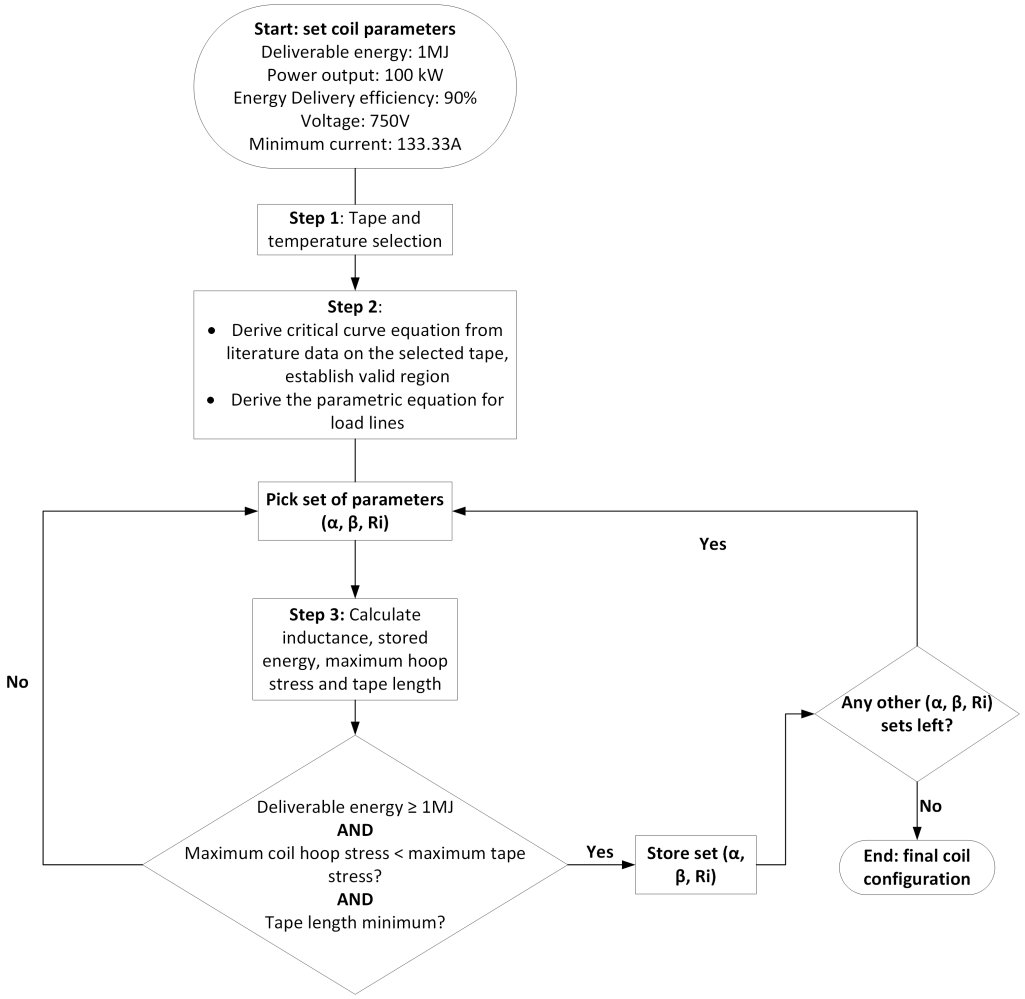

Figure 3.3: *Flow chart outlining the design steps for the superconducting magnet*

Initially, the required storage capacity, power output, energy delivery efficiency and voltage are set. The minimum current required in the coil is calculated by dividing the output power by the voltage. This case corresponds to a duty cycle of 100%. If the current injected in the coil would be lower than the minimum required current, the power level specified in the input could not be sustained.

If the coil current is higher than the minimum, the product between the coil current and the voltage would be higher than the required power. To obtain the right power level, the duty cycle of the power converter is modulated to a value lower than 100%, as will be explained in Chapter 4.

As a numerical exercise, a particular case is chosen for energy, power, voltage, efficiency and current, which are specified in the beginning. A storage capacity of 1 MJ is in the same order of magnitude with the state-of-the-art HTS coil designs in the literature, as

mentioned in section 1.4. As the typical discharge time for high power storage technologies spans between a few milliseconds and a few minutes, a target time of 10 seconds would fit within this range, leading to a target output power of 100 kW. The energy delivery efficiency, which refers to the proportion of the total stored energy that can be delivered at the nominal power (100 kW), should be as high as possible, hence a value of 90% has been commonly adopted [112]. Finally, a voltage of 750 V is a popular level within the range 600-900 V, typically used in DC industrial and transport applications [124]. These sectors, which include sensitive industrial loads and transient power spikes in light rail, would benefit from a fast responding and long lifetime high power energy storage technology. After establishing the requirements, the minimum required transport current which would sustain the target power output level of 100 kW is calculated. This is obtained by dividing the power by the voltage, for a value of $I_{t,min} = 133.3$ A. Hence, the peak transport current can be derived using:

$$\eta = \frac{E_{max} - E_{min}}{E_{max}} = \frac{I_{t,max}^2 - I_{t,min}^2}{I_{t,max}^2} = 1 - \frac{I_{t,min}^2}{I_{t,max}^2} = 90\% \tag{3.9}$$

$$I_{t,max} = \frac{I_{t,min}}{\sqrt{0.1}} = 421.63 \text{ A} \tag{3.10}$$

With a 100% duty cycle of the power converters, a 100 kW discharge rate can be achieved at 750V with as low as 133.3A. For a higher current, the duty cycle must be reduced to achieve the same discharge rate. At full charge (421.63A), the voltage must be chopped to $100,000/421.63 = 237.17V$. This translates in an initial duty cycle of $237.17/750 = 31.6\%$. As the coil is discharged, the current will reduce, requiring a higher duty cycle to achieve 100kW at 750V.

Once the initial parameters are set, a suitable superconducting tape model must be chosen, considering the required peak current. Generally, a safety factor of $s = 0.8$ is applied to the critical current of the tape [50, 112], hence the minimum critical current of the superconducting tape must be:

$$I_{c,min} = \frac{I_{t,max}}{s} = 527 \text{ A} \tag{3.11}$$

The tape operating temperature must be low enough to allow the conduction of a current $I_{c,min} = 527$ A.

Following the tape selection, its critical curve, which relates the critical current to the perpendicular magnetic field, is plotted. Using curve fitting, an approximate equation can be obtained for the relationship $I_c = f(B_\perp)$, making it possible to calculate values of I_c at any value of $B_\perp$. This step is detailed in Section 3.2.

Within a solenoid coil, there is a linear dependency between the transport current and the perpendicular (radial) magnetic field. This function is parametrised in terms of α, β and R_i, the dimensions of the tape, t and w and the safety and fill factors, s and f, respectively. The intersection between the load line and the critical curve is the working point for a certain coil configuration, representing the current at which the dissipation reaches $E = 1\mu V/cm$, as per the voltage criterion discussed in Section 2.3.3. Further detail on this step is in Section 3.3.

The next step consists of a parametric sweep of α, β and R_i, which is implemented using an algorithm in R, attached in Appendix B. For every set of values, the inductance is calculated using Welsby's formula for air-cored rectangular cross-section inductors wound with tapes [125], followed by the maximum hoop stress in the solenoid, using a method described by Wilson [37] and finally the stored energy. Each of these methods is detailed in Sections 3.4, 3.5 and 3.6, respectively. An initial minimum value of the tape length is assigned in a local variable. If the deliverable energy is at least 1 MJ and the maximum hoop stress is below the tape characteristic value, the length of tape used in that particular configuration is compared to the local minimum. If a smaller length is achieved, the local minimum takes this value. This process is repeated until all the sets (α, β, R_i) are verified. The final result consists of a discrete optimisation of the coil configuration, in which the target storage is achieved while using the least amount of superconducting tape.

3.2 Superconducting tape selection

2G HTS tapes are commercially available from several manufacturers, including Bruker, American Superconductors, Fujikura, SuNAM and Superpower Inc. [98]. They come in various widths between 3 and 12 mm and with different thickness of the Cu and Hastelloy layer, depending on the requirements. As the most studied tape configurations for SMES are 4 and 12 mm wide, there is extensive characterisation data available in the literature

[98, 126], particularly for tapes made by Superpower Inc. Two of the most popular ReBCO tapes made by Superpower, SCS4050 (4 mm width) and SCS12050 (12 mm width) were compared for use in a SMES coil in [49]. The study concluded that at 22 K and for similar storage capacities, the coil using the 4 mm tape requires three times the length of tape and costs more than twice as much as the coil with 12 mm tape. Moreover, the operating current of SCS4050 at 22 K is limited at 160 A, which only allows for a discharge margin of 27 A before reaching the minimum value of 133 A, required for supplying 100 kW.

To increase the current carrying capability, multiple superconducting tapes are connected together in parallel to form a Roebel cable, as illustrated in Figure 2.9. However, this method requires cutting the tapes so that they can be wound, reducing the critical current per tape by up to 61 % [100]. For these reasons, the choice of tape for designing the 1 MJ/100 kW coil is the Superpower SCS12050, with its properties summarised in Table 3.1. While the numerical properties of this tape are used for estimating the final coil parameters in this section, the coil design methodology is universally applicable to any kind of 2G HTS flat tape.

Table 3.1: *Properties of Superpower SCS12050 YBCO tape*

YBCO tape characteristics	
Manufacturer	Superpower Inc.
Tape model	SCS12050
Tape Dimensions (without insulation)	
Width (mm)	12
Total tape Thickness (mm)	0.1
• **YBCO layer thickness (µm)**	1
• **Hastelloy layer thickness (µm)**	50
• **Cu layer thickness (µm)**	2 x 20
• **Stabilizer and buffer (µm)**	9
Tape Performance	
Critical Current (Self field, 77K) (A)	330
Critical Current (B = 4T perpendicular, 20K) (A)	600
Minimum Bending Radius (mm)	5
Critical axial Tensile strain (%) (at 77K)	0.45
Maximum Stress (MPa) (at 77K)	> 550

The insulation layer applied to the tape has two main roles. Firstly, it provides electrical insulation between consecutive turns and it thermally insulates the tapes, helping maintain

their temperature below the critical value. A layer of polyimide of 2.5 μm was proven sufficient for insulation at 1000 V [127]. Secondly, ReBCO coils are typically impregnated with epoxy, acting as a binder for the winding and a thermal conduction path from the interior of the coil. If epoxy is applied directly to the tape, large binding forces can lead to delamination, separating individual layers and damaging the tape. By coating the tape in polyimide insulation, a weaker bond between the epoxy and the tape is achieved, thus reducing the stress [91].

With present state-of-the-art manufacturing techniques, such as Ion Beam Assisted Deposition (IBAD), it is possible to reach values of up to 300 kAm at 77 K, with tape lengths of over 1 km [24]. While it is desirable to make the superconducting magnet using as few tape sections as possible, in order reduce the number of joints, which can have a resistance of up to $20n\Omega$ [94], it is difficult to ensure a consistent tape performance along the entire length. As a solution, the entire solenoid is made of multiple double pancake coils, with the structure presented in the previous chapter.

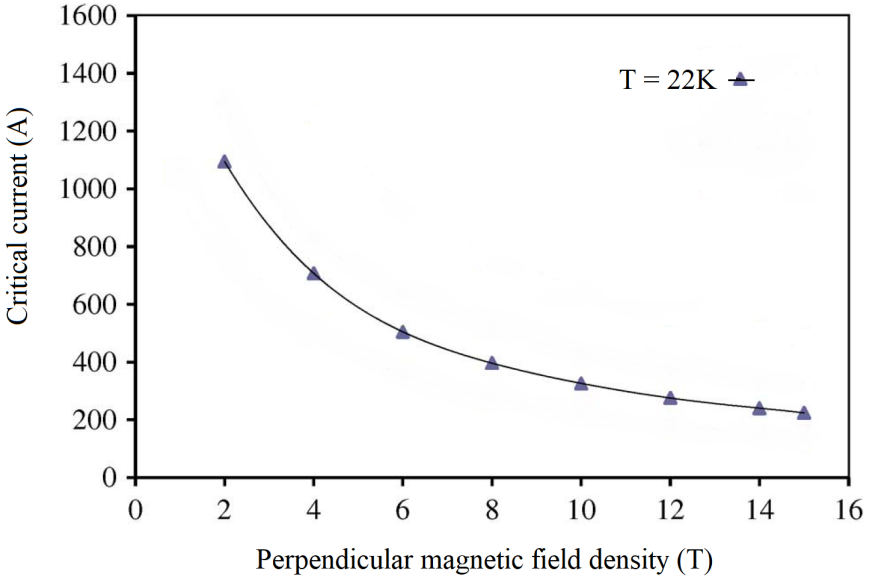

Figure 3.4: *Critical Current as a function of perpendicular field at 22 K in SCS12050 tape. Adapted from [126]*

Due to anisotropy, the main limiting factor for the critical current in the tape is the perpendicular magnetic field lines, at either end of the coil. The tape selected for this project, Superpower SCS 12050, was tested by Lombardo et al. [126], under various magnetic fields and temperatures. A sufficiently large difference between the critical

transition temperature for the superconducting material and the operating temperature is necessary for accommodating a temperature rise due to losses without a state transition. To achieve this, a low operating temperature of $T_{op} = 22K$ is chosen. The perpendicular field critical curve for the tape at 22 K is represented in Figure 3.4.

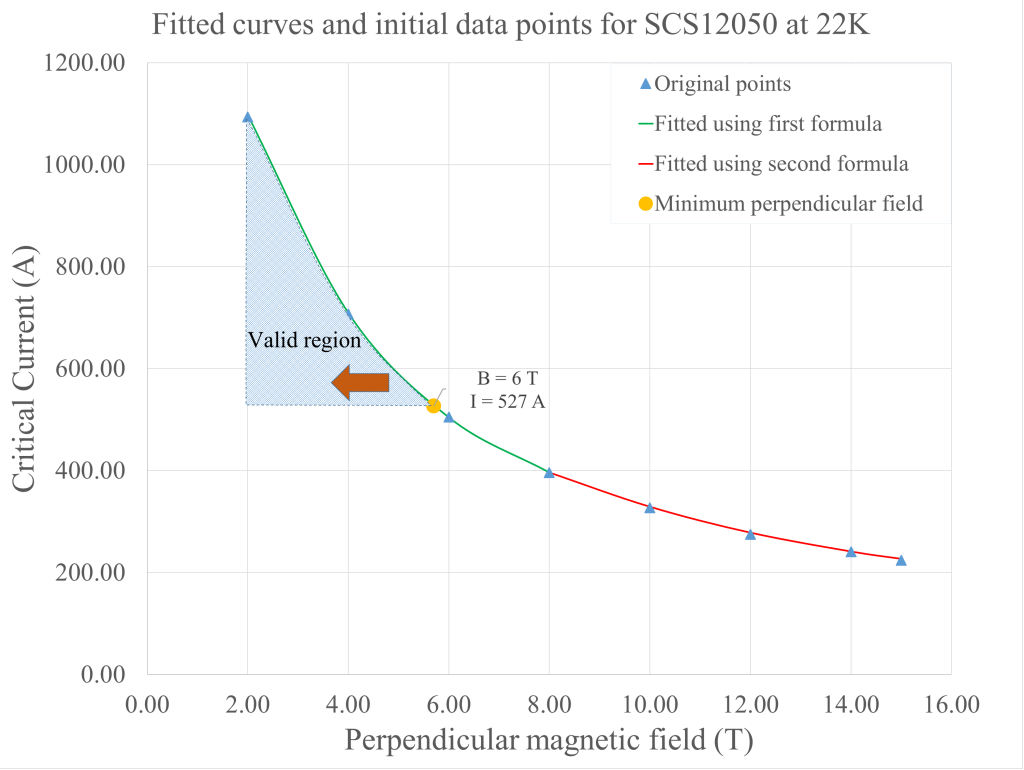

Figure 3.5: *Critical curve fitted using equation 3.12*

As a dataset is not available, and assuming that the graph is to scale, an online graph mapping application, Automeris [128], is used to accurately determine the values of critical current at different field values. Once the graph is uploaded, the minimum and maximum points of each axis are marked on the graph, and the coordinates are assigned to these points. The entire graph is then mapped in a 2D array, which helps determine the exact coordinates $(B_\perp, I_c)$ for every chosen point. The value of critical current at every marker on the 22K curve is then recorded. A curve fitting tool is used with the points of coordinates $(B_\perp, I_c)$ to determine a suitable analytical form of the equation $I_c = f(B_\perp)$. The best fit is achieved if the entire interval 2-15 T is split in two: 2-8 T and 8-15 T. With this

approach, the function is:

$$\begin{cases} I_c = 275.76 + 1555.825 \cdot e^{-0.32B_\perp}, \text{ for } 2T \leqslant B_\perp \leqslant 8T \\ I_c = 143.32 + 920.9 \cdot e^{-0.162B_\perp}, \text{ for } 8T \leqslant B_\perp \leqslant 15T \end{cases} \tag{3.12}$$

With a minimum necessary peak current of $I_{op,min} = 421.63A$ and a safety factor of $s = 0.8$, the minimum critical current is $I_{c,min} = 527A$. This corresponds to a value of perpendicular field of $5.7T$ if using the first part of equation 3.12. Therefore, in order to discharge at least 90% of the stored energy at a rate of 100 kW, with a safety factor of 0.8, the coil must operate at radial field densities of less than 5.7 T, making only the first part of equation 3.12 necessary for this design.

3.3 Magnetic fields in coils

The magnetic field induced by each turn of the coil can be calculated using the Biot-Savart law:

$$\vec{B} = \frac{\mu_0}{4\pi} \int_C \frac{I\vec{dl} \times \hat{\mathbf{r}}}{r^2} \tag{3.13}$$

where $\vec{B}$ is the magnetic flux density generated at a distance r from a wire of length $\vec{dl}$, carrying a current I. With a large number of turns, calculating the total field generated becomes very complex, an FEA model being necessary. Nevertheless, in designing a SMES coil, only the peak values of magnetic field are necessary, as they are the main limiting factor for the critical current, and hence, the maximum storable energy. As an alternative, the method presented by Walstorm et al. [129] is used to quickly estimate the peak radial field generated by the coil, according to its shape factors.

Firstly, the central axial field, $B_z(0,0)$, is calculated using the formula:

$$B_z(0,0) = jR_iF(\alpha,\beta) \tag{3.14}$$

where

$$F(\alpha,\beta) = \mu_0\beta \ln\left(\frac{\alpha + \sqrt{\alpha^2+\beta^2}}{1+\sqrt{1+\beta^2}}\right) \tag{3.15}$$

This is obtained by integrating the contribution of each current loop [37].

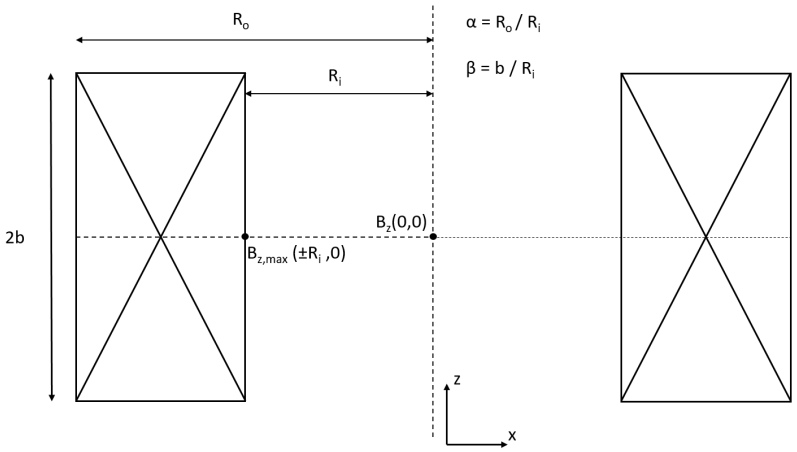

Figure 3.6: *Diagram of the cross section in an axisymmetric solenoid*

The current density in the coil, j, is calculated using:

$$j = \frac{I_{op} N}{A_{tot}} \tag{3.16}$$

where I_{op} is the operating current in a single tape, N is the total number of tapes in the coil and A_{tot} is the total cross sectional area of the coil, calculated as $A_{tot} = 2b(R_o - R_i) = 2(\alpha - 1)\beta R_i^2$.

The fill factor defined previously can be expressed as $f = \frac{N A_{tape}}{A_{tot}}$.

Considering that $N = \frac{f A_{tot}}{A_{tape}}$ equation 3.16 can be rewritten as:

$$j = \frac{f I_{op}}{A_{tape}} = \frac{f I_{op}}{tw} \tag{3.17}$$

in which both t and w include the insulation thickness.

The maximum axial field is measured at the inner surface of the coil, in the mid-plane, as marked in Figure 3.6. This is true for any coil where $\alpha > 1.08$, however there are several situations when $\alpha < 1.08$ in which the maximum axial field is attained at either end of the coil, where $z = \pm b$ [129]. Given the anisotropy of the tape chosen, it is preferable to reduce the effect of perpendicular field, hence the value of α will be larger or equal to 1.08.

Depending on the shape factor of the coil, the maximum axial field is related to the central field by means of a factor $G(\alpha, \beta)$. While this has no analytical form, it has been numerically calculated and tabulated, as presented in Figure 3.7.

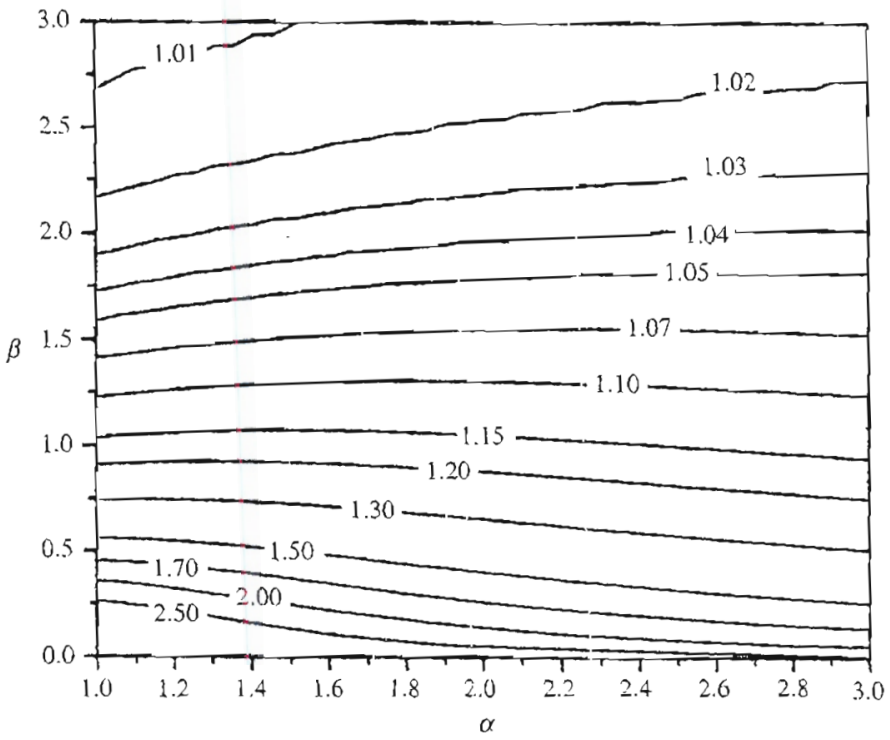

Figure 3.7: *Ratio between maximum and central axial field in a rectangular cross section coil, as a function of α and β [130]*

Therefore the maximum axial field is:

$$B_{z,max} = B_{0,0} \cdot G(\alpha, \beta) = \frac{fI_{op}}{tw} R_i F(\alpha, \beta) G(\alpha, \beta) \tag{3.18}$$

Finally, the relationship between the maximum axial and the maximum radial field is necessary for constructing the load line of the coil. While an analytical form is has not been derived, given the complexity of the problem, the ratio between $B_{r,max}$ and $B_{z,max}$ was numerically calculated and tabulated in [129] and is depicted in Figure 3.8.

The maximum radial field, which is also perpendicular to the tape at either end of the coil, is expressed as:

$$B_{r,max} = B_{z,max} \cdot K(\alpha, \beta) = \frac{fI_{op}}{tw} R_i F(\alpha, \beta) G(\alpha, \beta) K(\alpha, \beta) \tag{3.19}$$

Equation 3.19 can be also written as:

$$I_{op} = \frac{tw}{fR_i} \frac{B_{r,max}}{F(\alpha, \beta) G(\alpha, \beta) K(\alpha, \beta)} \tag{3.20}$$

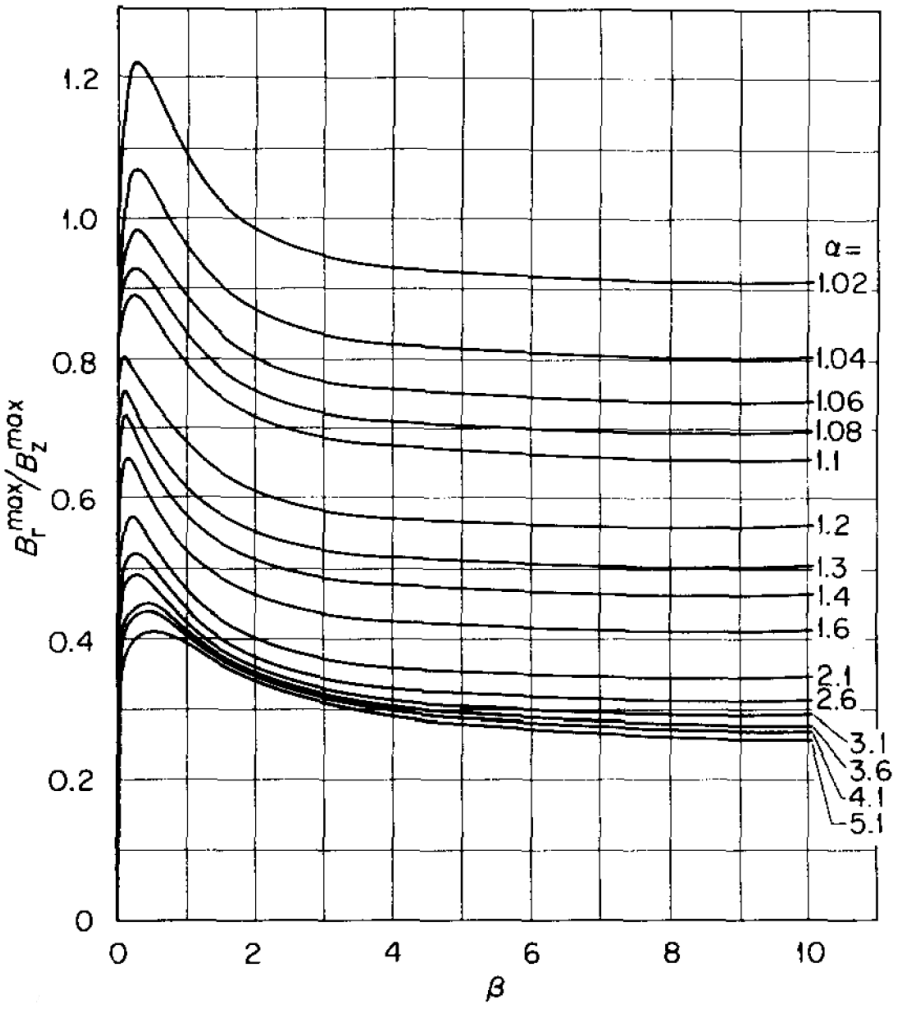

Figure 3.8: *Ratio between radial and axial magnetic field as a function of α and β [129]*

which can be used for plotting the load lines of the coil, depending on its shape factors and the magnetic field perpendicular to the tape. Using the safety factor s defined in Section 3.1.2, $I_{op} = sI_c$, increasing the margin between the operating and the critical current, hence leading to:

$$I_c = \frac{tw}{fsR_i} \frac{B_{r,max}}{F(\alpha,\beta)G(\alpha,\beta)K(\alpha,\beta)} \tag{3.21}$$

Using this equation, the load lines for different configurations of the coil are plotted on the same graph as the critical current curve of the tape. By adjusting the variables α, β and R_i, the gradient of the load line is changed. As shape factors G and K can only be calculated numerically for different pairs (α, β) (values given in Appendix A), load lines can only be plotted for discrete values of parameters α, β and R_i. To check how varying each of these parameters affects the maximum working point, three cases are considered.

Firstly, considering a perpendicular magnetic field value of 5.7 T and a Brooks coil configuration ($\alpha = 2$ and $\beta = 0.5$)[131], a rough figure for the inner radius of the coil can be estimated. Using the equation:

$$w = \frac{B_{z,max}^2}{2\mu_0} \tag{3.22}$$

where w is the energy stored per unit volume in the magnet, $B_{z,max}$ is the maximum axial field estimated using equation 3.18 and μ_0 is the magnetic permeability of free space, the volume required to store 1 MJ is calculated as 0.0246 m^3. The internal volume of a Brooks coil is expressed as $V_{Brooks} = \pi R_i^3$, hence for storing 1.11 MJ the radius is 0.198 m.

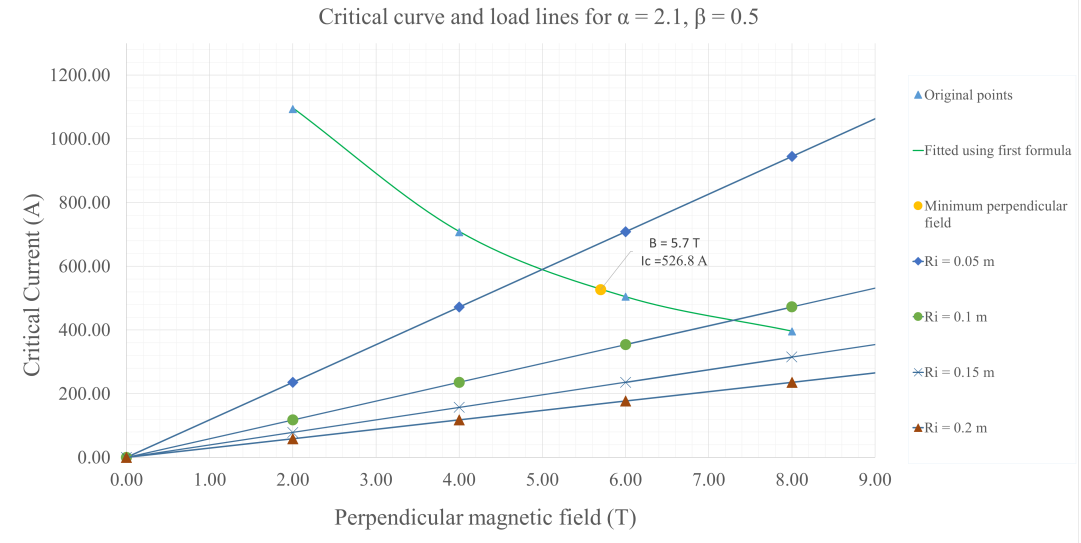

Figure 3.9: *Load Lines for a solenoid made with SCS12050, with* $\alpha = 2.1$ *and* $\beta = 0.5$

In the first case, $\alpha = 2.1$ and $\beta = 0.5$, close to a Brooks coil, while different values of R_i are considered. The plot in Figure 3.9 shows that for lower values of R_i, larger values of critical current can be obtained for the same perpendicular magnetic field.

In the following two graphs, depicted in Figures 3.11 and 3.10, the value of R_i is fixed to 0.1 m, for which the load line crosses the critical curve closest to the point of minimum perpendicular field (5.7 T). In the former, α is fixed at 2.1 and β is varied, while in the latter, β is fixed at 0.5 and α is varied.

When R_i and α are fixed, the lower β is, the higher the critical current for the same perpendicular field. This shows that longer coils can sustain higher values of magnetic field without exceeding the critical curve. Finally, for a fixed coil length and internal

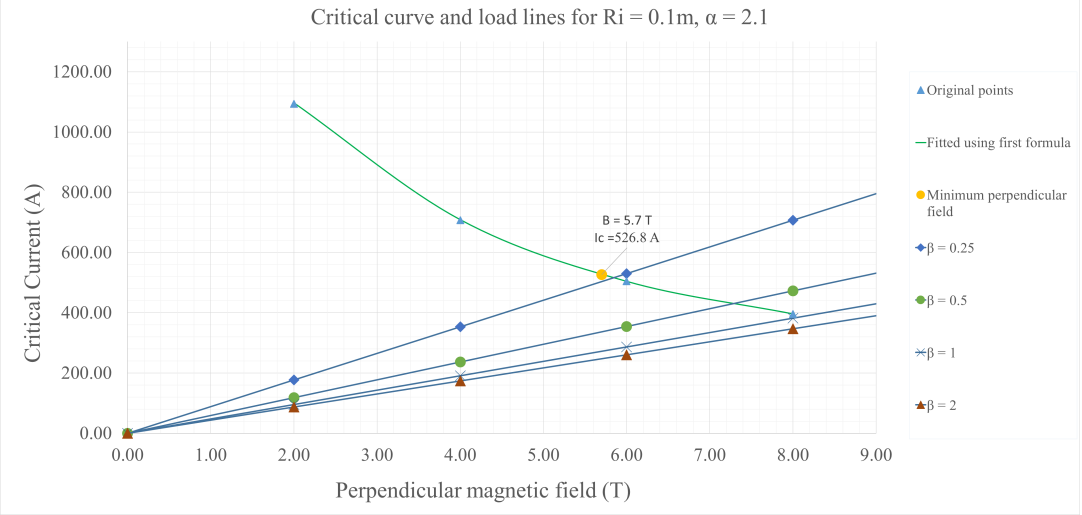

Figure 3.10: *Load Lines for a solenoid made with SCS12050, with* $R_i = 0.1m$ *and* $\alpha = 2.1$

radius, the thicker the coil is (i.e the larger α), the more turns, which lead to a higher magnetic field, but a lower critical current.

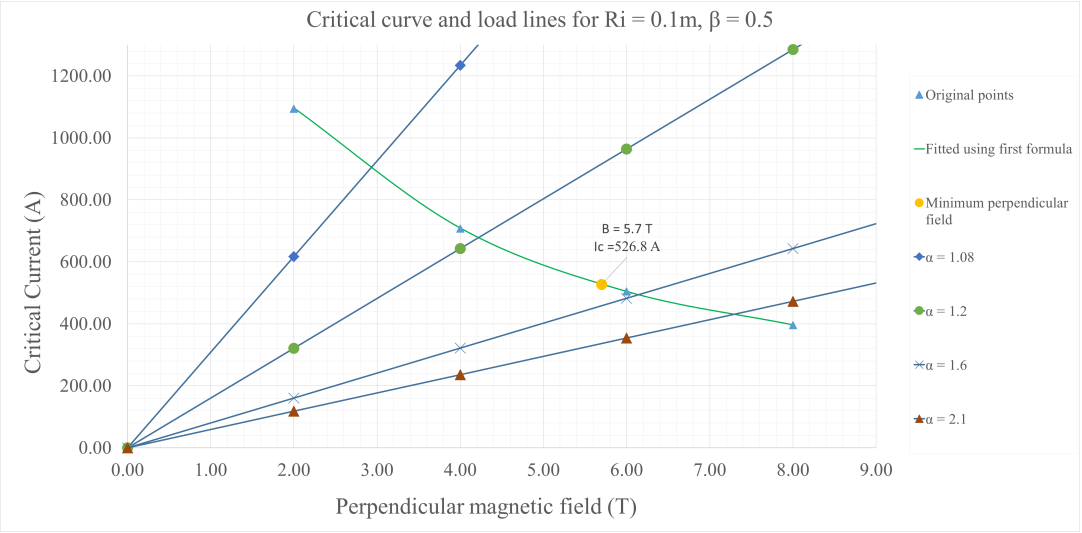

Figure 3.11: *Load Lines for a solenoid made with SCS12050, with* $R_i = 0.1m$ *and* $\beta = 0.5$

By reducing the values of either α or β, the gradient of the load line increases and so does the critical current at the intersection with the critical curve. The opposite effect is noticed when increasing the inner radius of the coil, as the load line gradient decreases. Since the required critical current must exceed 527 A, due to the power requirement the maximum possible inner radius of the coil can be estimated by setting α and β to their lowest values of 1.08 and 0.25, respectively, while plotting the load lines for different values of R_i. The

graph in Figure 3.12 shows that for an inner radius of over 0.4 m, the intersection point between the load line and the critical curve is at a critical current of less than 527 A, making all these configurations not suitable for the current requirements.

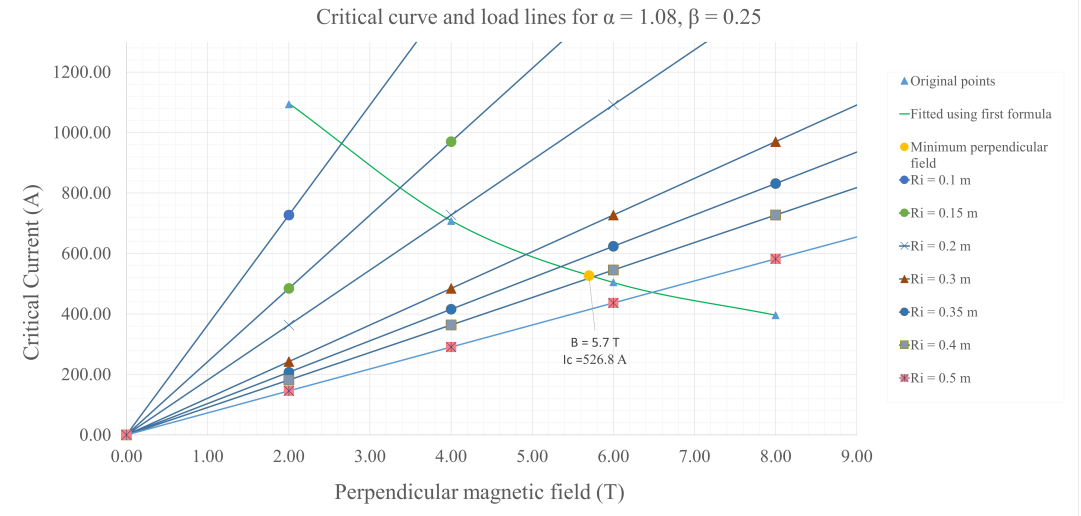

Figure 3.12: *Load lines for a solenoid* $\alpha = 1.08$ *and* $\beta = 0.25$ *and variable* R_i

In a discrete optimisation of the coil configuration, parameters α, β and R_i must be adjusted in order to reach the working point that provides a minimum critical current of 527 A, which corresponds to a radial magnetic field of 5.7 T, while being capable of delivering 1 MJ of energy, using the least amount of superconducting tape. The intersection between a parametric load line and the critical curve is given by:

$$\frac{tw}{fsR_i}\frac{B_\perp}{F(\alpha,\beta)G(\alpha,\beta)K(\alpha,\beta)} = 275.76 + 1555.825 \cdot e^{-0.32B_\perp} \tag{3.23}$$

hence for any coil configuration, the following relations must stand:

$$275.76 + 1555.825 \cdot e^{-0.32B_\perp} > \frac{tw}{fsR_i}\frac{B_\perp}{F(\alpha,\beta)G(\alpha,\beta)K(\alpha,\beta)} \tag{3.24}$$

for any operating value of perpendicular magnetic field, as well as:

$$B_{perp} < 5.7T \tag{3.25}$$

which ensures that the coil can deliver 1 MJ of energy at a 90% efficiency.

3.4 Coil inductance

To calculate the inductance of the coil, the formula developed by Welsby is used [125]. This was developed for rectangular cross section solenoids wound with flat tapes and has the form:

$$L = \frac{2\pi^2 R_{mean}^2 N^2}{2b} K_n \cdot 10^{-7} \tag{3.26}$$

where K_n is the Nagaoka correction factor, accounting for a non-uniform field distribution in short and thick coils and given by the expression:

$$K_n = \frac{1}{1 + 0.9\frac{R_{mean}}{2b} + 0.32\frac{c}{R_{mean}} + 0.84\frac{c}{2b}} \tag{3.27}$$

The notations used in these equations are the same as in Figure 3.2. The dimensions are expressed in metres and the resulting inductance in Henries. By substituting in equation 3.26 all the variables expressed in section 3.1.1 as functions of α, β, R_i, the final expression of inductance takes the form:

$$L = \frac{2\pi^2 f^2 (\alpha-1)^2 \beta R_i^5}{t^2 w^2} \frac{(\alpha+1)^2}{1 + 0.9\frac{\alpha+1}{4\beta} + 0.64\frac{\alpha-1}{\alpha+1} + 0.84\frac{\alpha-1}{2\beta}} \cdot 10^{-7} \tag{3.28}$$

3.5 Stress and strain

Within a solenoid carrying transport current, magnetic fields cause mechanical stress, primarily as circumferential tension and axial compression [37]. The particular tape used in the current design can withstand stress levels of 550 MPa, with a strain of 0.45% causing less than 5% drop in the critical current value. The hoop stress is calculated using the equation:

$$\sigma_{\theta,max} = \frac{B_\perp^2}{F(\alpha,\beta)G(\alpha,\beta)K(\alpha,\beta)^2} \frac{1}{(\alpha-1)} \left\{ \frac{2\alpha(7\alpha^2+\alpha+1)}{9(\alpha+1)} - \frac{5\alpha^2+1}{6} \right\} \tag{3.29}$$

which is derived in Appendix C.

The temperature and composition of a superconducting tape, including materials used and the thickness of each layer, give the value of its Young modulus. Since the exact value for the particular configuration used in this design has not been published, a good estimation can be obtained by using data for the same model of tape, measured at different temperatures and overall thickness of Cu layer. The values of Young's modulus for the same SCS 12050 tape, but at 4 and 297 K, with a Cu layer of 65 and 100 μm was published in [132] and are summarised in table 3.2.

Table 3.2: *Values of Young's modulus for various configurations of SCS12050 tape*

Young's Modulus (GPa)		Cu layer thickness (µm)		
		65	100	40
Temperature (K)	297	117.4	100.9	129.2
	4	125.3	107.9	137.7
	22	124.8	107.5	137.3

The corresponding values for an operating temperature of 22 K and a Cu layer thickness of 40 μm are approximated using linear regression, assuming a dependency in the form: $Y = a_1T + b_1$ and $Y = a_2t_{Cu} + b_2$, where T is the temperature and t_{Cu} is the thickness of the Cu layer. The of Young's modulus at the desired combination of temperature and Cu layer thickness can be derived using either of the equations, the results being 137.45 GPa if using the temperature regression and 137.16 GPa if using the Cu layer thickness regression. Since they are very similar, the value used will be their average, 137.3 GPa.

The strain is calculated using:

$$\varepsilon(\%) = \frac{\sigma_{\theta,max}}{Y} \cdot 100 \tag{3.30}$$

3.6 Stored energy and final configuration

Finally, the total energy stored can be calculated using the equation:

$$E = \frac{LI_{op}^2}{2} \tag{3.31}$$

where $I_{op} = sI_c$ and I_c is the critical current of the working point, given by equation 3.23. The inductance is calculated using equation 3.28.

The central part of the algorithm from Appendix B is the function $coil_configuration$, which takes three inputs consisting in the amount of deliverable energy required (expressed in Joules), the output power (expressed in kW) and the voltage (in Volts) and returns a series of parameters corresponding to the configuration of the coil that satisfies all the constraints and uses the least amount of tape. The function is based on four 'for' loops, used to pick distinct sets of parameters $(alpha, beta, ri, B)$. Depending on the values of α and β, the value of fgk is calculated, representing the product of the three factors F, G, K given in Appendix A. On the other hand, ri and B are the inner radius and perpendicular magnetic field, picked from predefined ranges in increments of 0.01 m and 0.01 T, respectively. The matrix T has the following form:

Table 3.3: *Matrix T, where every element is the product of the corresponding F, G and K factors*

F*G*K	Alpha								
Beta	1.08	1.1	1.2	1.3	1.4	1.6	2.1	2.6	3.1
0.25	5.41E-08	6.35E-08	1.05E-07	1.32E-07	1.48E-07	1.77E-07	2.23E-07	2.43E-07	2.55E-07
0.5	6.38E-08	7.53E-08	1.23E-07	1.58E-07	1.92E-07	2.45E-07	3.33E-07	3.85E-07	4.19E-07
0.75	6.60E-08	7.76E-08	1.29E-07	1.70E-07	2.06E-07	2.67E-07	3.83E-07	4.60E-07	5.13E-07
1	6.83E-08	7.96E-08	1.34E-07	1.79E-07	2.14E-07	2.82E-07	4.12E-07	5.08E-07	5.84E-07
1.5	6.85E-08	8.22E-08	1.38E-07	1.84E-07	2.25E-07	3.06E-07	4.41E-07	5.60E-07	6.50E-07
2	6.91E-08	8.23E-08	1.38E-07	1.85E-07	2.29E-07	3.13E-07	4.54E-07	5.85E-07	6.97E-07
2.5	6.92E-08	8.23E-08	1.38E-07	1.88E-07	2.30E-07	3.11E-07	4.56E-07	5.93E-07	7.23E-07
3	6.96E-08	8.15E-08	1.38E-07	1.88E-07	2.29E-07	3.13E-07	4.58E-07	5.91E-07	7.36E-07

The process employed is a discrete optimisation, which calculates essential coil parameters, such as inductance, magnetic field, stress, stored energy and length of superconducting tape and verifies if they satisfy a set of requirements. The matrix T, from which the value of fgk is picked, has 9 columns and 8 lines, corresponding to the number of individual values of α and β, respectively. The iterations over the matrix are done with the indices i and j, which are also used to iterate over each of the vectors α_vector and β_vector, respectively. The energy delivery efficiency is also factored in, leading to an oversized total storage capacity.

The coil properties are summarised in Table 3.4. The low operating magnetic field allows a larger transport current, which, in turn, increases the overall energy delivery efficiency at 100 kW to 91.4 %, exceeding the required value of 90 %.

Table 3.4: *Final design parameters of the YBCO SMES coil*

YBCO coil design parameters	
Maximum Storage Capacity (MJ)	1.112
Deliverable Energy at 100 kW (MJ)	1
Internal Radius (m)	0.24
External Radius (m)	0.26
α	1.1
Height (m)	0.36
β	0.75
Number of turns (N)	5140
Number of Double Pancakes	15
Number of turns per Double Pancake	343
Fill Factor	0.75
Safety factor	0.8
Coil Inductance (H)	10.72
Maximum Operating radial field density (T)	5.05
Maximum Operating axial field density (T)	6.16
Operating Temperature (K)	22
Critical Current (A)	539.50
Peak Transport Current (A)	455.6
Total length of tape used (km)	8.14
Energy stored for 1 km of tape (kJ)	136.6
Max hoop stress (MPa)	221.84
Young's Modulus for SCS12050 (GPa)	137.3
Poisson's ratio	0.3
Strain (%)	0.162

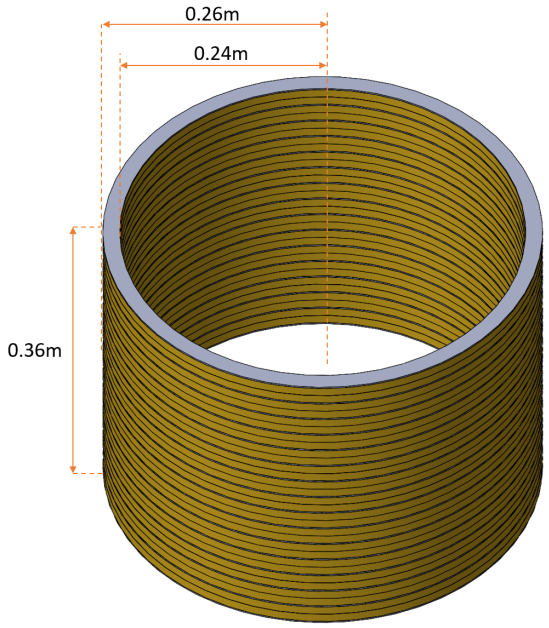

Figure 3.13: *Model of the solenoid with the final parameters*

3.7 Impact of power and voltage

The particular case analysed in the previous section was based on a coil output power of 100 kW at a voltage of 750 V. The algorithm is capable of calculating the near-optimal tape length for at various voltages and power outputs.

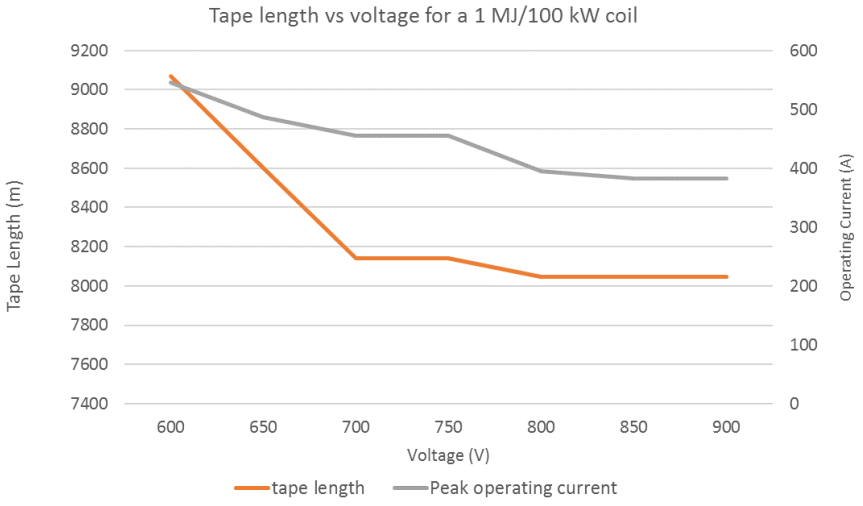

Figure 3.14: *Tape length and peak operating current as a function of voltage*

As the voltage is increased, a lower current is required to achieve the same power level. Up to 800V, the length of tape used in the coil is gradually reducing. After the 800V level, as the voltage is increased, the required current is reduced further, which enables a wider range of magnetic fields to be used in the coil configuration. Given that the stored energy is proportional to the square of the current and to the inductance, reducing the peak operating current by half requires an increase of 4 times in inductance. If $I_1 = 2I_2$, for a given storage requirement E_{stored}:

$$E_{stored} = \frac{L_1 \cdot I_1^2}{2} = \frac{L_2 \cdot (2I_2)^2}{2} = \frac{L_2 \cdot 4I_2^2}{2} \tag{3.32}$$

$$L_1 = 4L_2 \tag{3.33}$$

Therefore, increasing the voltage is only advantageous up until a certain point (800V in this particular case). Beyond this point, choosing a configuration with a lower peak operating current would require a higher inductance, as well as a higher tape length.

3.8 Discussion

Given the large number of variables that influence the design of a coil, including the performance of the tape (critical curve equation, temperature, anisotropy), the fill factor, safety factor and required output power, it is nearly impossible to fairly compare different coils with the output of this algorithm in order to assess its performance. While other designs may use the same type of HTS material, they either use it in a cable configuration as opposed to a single tape [112], from a different manufacturer and at a different temperature [123] as well as in different widths [34, 50].

The design method proposed in this chapter allows for a quick estimation of essential parameters, such as inductance, critical current, as well as physical dimensions of a coil made of superconducting tape, with a given target of energy storage capacity. Moreover, the output is also using the least amount of tape out of all the possible discrete pairs of (α, β, R_i). The steps required for building the algorithm are detailed throughout the sections of this chapter and are summarised in the flowchart in Section 3.1.2.

The key advantages of this method are its simplicity and versatility, as it can be adapted to any 2G HTS tape by changing the critical curve equation in the algorithm. Compared to other methods used in the literature, the design in this chapter does not require setting up an FEA model, or complex optimisation procedures, such as the Genetic algorithm, which may require significant computational resources. Additionally, the output power level of the coil is considered throughout the design process, further enhancing the solution.

Nevertheless, there are some limitations of this method, which must be addressed if a more detailed model of a coil is required. Firstly, shape factors α and β only take 9 and 8 values, respectively. These numbers are limited by the numerical plots used for the values of magnetic field scaling factors $G(\alpha, \beta)$ and $K(\alpha, \beta)$, for the lack of an analytical expression. This aspect can be improved by developing a parametric 3D magnetostatic model in Comsol, which can be used in calculating factors G and K for any possible pair of (α, β). The output of this calculation can then be used in the R algorithm for the equations of load lines, thus allowing for a global optimisation of the coil shape.

Secondly, the field distribution within the coil is not considered. Throughout the coil, the critical current is capped at the value corresponding to the peak perpendicular field,

which is only present at either end of the solenoid. In the regions close to the mid plane of the coil, the tapes are only subject to a parallel magnetic field and can potentially carry a higher current. Alternative designs for coils were proposed, where the solenoid is split into multiple stacked pancakes of various thickness: the thickest are placed close to the mid-plane of the solenoid, while the thinnest are at either end of it, effectively reducing the perpendicular component of the field [133, 134]. However, this design extension is beyond the scope of this project.

Chapter 4

SMES power control

In Chapter 1, two of the common power converters used in SMES are briefly outlined: the voltage source converter (VSC) and the current source converter (CSC). These have been widely employed in the conceptual design of SMES units connected to AC grids, however the choice of switches, their operation and limitations has not been explored in depth. When part of a DC microgrid, the power converter of a SMES unit must deliver a reliable power output while the transport current is decreasing. The same challenge stands for a VSC, where the DC link capacitor voltage must be constant. In this chapter, the DC-DC converter configuration is analysed for the 1MJ/100kW coil designed in the previous chapter.

4.1 Model setup

4.1.1 Modes of operation of SMES magnet

Using the specifications of the SMES unit designed in the previous chapter, a practical model is built to assess its operation. The magnet is emulated as an inductor with no resistance, an inductance of $L = 10.72$ H and a peak transport current of $I_{op} = 455.6$ A. The total stored energy in this unit is $E = \frac{LI_{op}^2}{2} = 1.112$ MJ and it is assumed that the unit is fully charged in the beginning.

The DC-DC side of the converter consists of two Insulated Gate Bipolar Transistors (IGBT) with antiparallel diodes, as well as two diodes. This configuration allows a bidirectional, two-quadrant operation of the SMES magnet, allowing it to charge and discharge while the current is positive. This is achieved by adjusting the switching pattern of the transistors to create either a positive, or a negative voltage at the terminals of the magnet, which, intrinsically, is a zero-voltage device. The switching pattern of IGBTs in each case is presented in Table 4.1.

Table 4.1: *IGBT Switching Pattern*

	T_1	T_2
Charge	PWM	1
Store	0	1
Discharge	0	PWM

When the voltage is positive, current flows from the DC-link capacitor to the magnet, charging it, based on the equation:

$$V = L\frac{\mathrm{d}I}{\mathrm{d}t} \tag{4.1}$$

In this case, the magnet behaves like a load and the current flow is illustrated in Figure 4.1. To achieve this practically, T_1 is chopping, while T_2 is constantly on. The duty cycle on T_1 is adjusted according to the difference between the DC link capacitor voltage and a reference value, set to 750 V in this example.

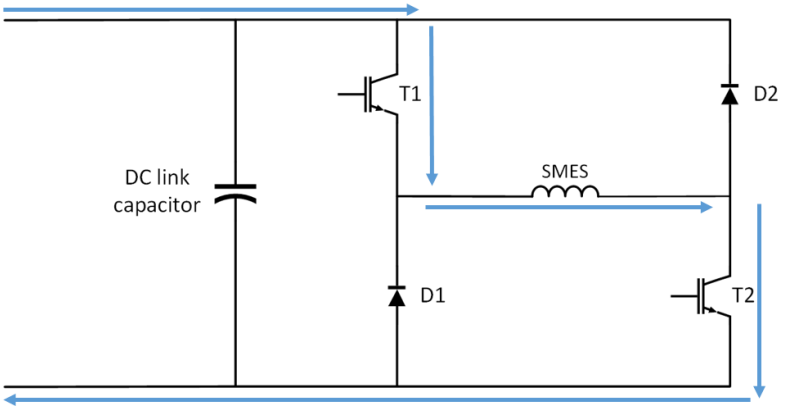

Figure 4.1: *SMES DC-DC chopper in charge mode*

When the voltage at its terminals is negative, the equation becomes:

$$V = -L\frac{\mathrm{d}I}{\mathrm{d}t} \tag{4.2}$$

as the magnet behaves like a generator, with the current path illustrated in Figure 4.2. The duty cycle is adjusted depending on the power draw of the external circuit, and it will vary between 100%, when the power draw is equal to the product between the coil current and the capacitor voltage, or lower than 100%, when the power draw is lower.

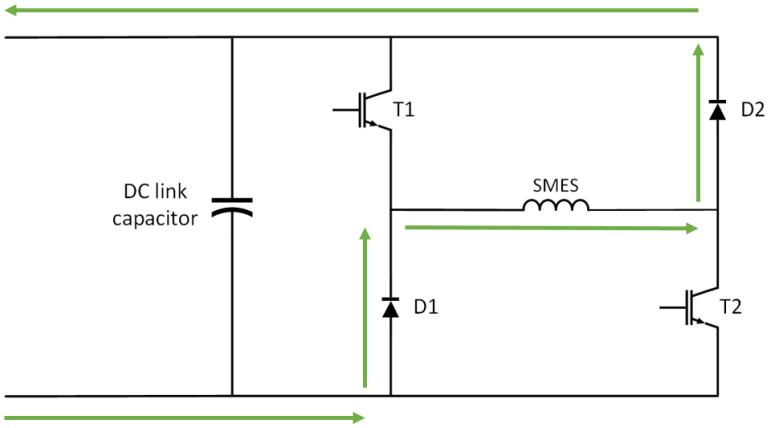

Figure 4.2: *SMES chopper in discharge mode*

If the DC link voltage is 750 V, the chopper operates in a short circuit mode, storing the energy. By maintaining T_1 off and T_2 on, the transport current is circulating with minimal decay through diode D_1, as depicted in Figure 4.3.

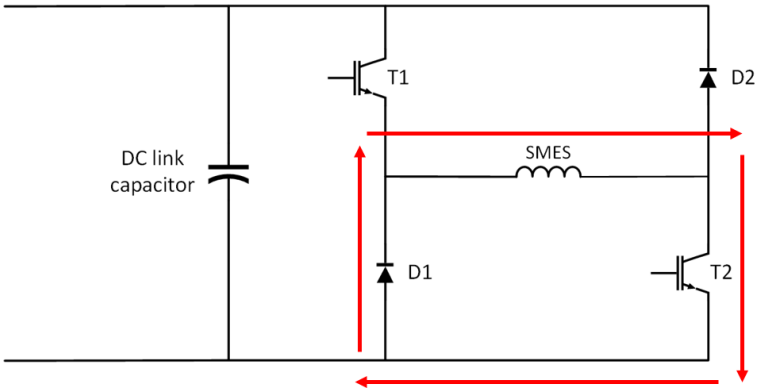

Figure 4.3: *SMES DC-DC chopper in storage mode*

4.1.2 DC microgrid simplified model

To assess the operation of the SMES unit, a circuit model of a simplified DC microgrid is built in MATLAB/Simulink. Besides the coil, emulated as a zero resistance inductor, connected to a DC-DC chopper, the circuit includes a DC link capacitor (C = 10 mF)

with the role of maintaining a steady voltage of 750 V, as well as a current source, which can operate either as a load or a generator, depending on the sign of the current. Each IGBT is driven by a DC PWM generator, which converts an input between 0 and 1 into a pulse width modulated signal with the duty cycle proportional to the value of the input. The circuit is depicted in Figure 4.4.

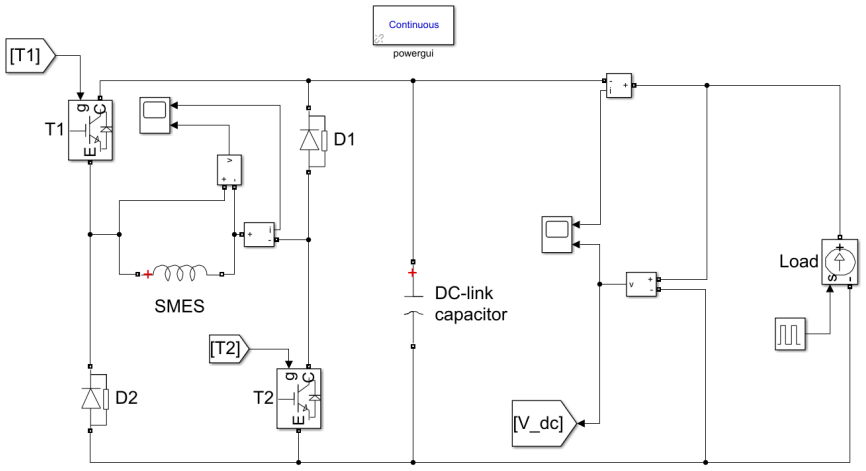

Figure 4.4: *Circuit diagram of the SMES connected to a DC-DC chopper, a DC-link capacitor and a load*

The control loop for the transistors takes the difference between the measured DC link voltage, V_{DC} and the reference value of $V_{ref} = 750$V, normalised to $v^* = \dfrac{V_{DC} - V_{ref}}{V_{ref}}$ and referred to as 'error'. If the DC link voltage exceeds the reference value, the input for the control loop is positive, while if the capacitor voltage drops below the reference value, the input becomes negative. The goal of the control loop is to minimise the error, by adjusting the operating mode of the SMES unit to inject, absorb or store current.

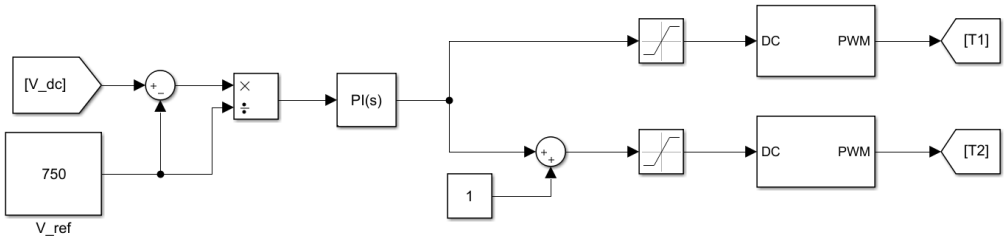

Figure 4.5: *PI Control loop for IGBTs T1 and T2*

Depending on the value of v^*, the following cases are defined:

$$\begin{cases} \text{if } v^* > 0, T_1 = PWM, T_2 = 1 \\ \text{if } v^* < 0, T_1 = 0, T_2 = PWM \end{cases}$$

Therefore for a negative error, T_1 must saturate to 0, while for a positive error, T_2 must saturate to 1. For the PWM generator controlling T_1, no input adjustment is necessary. However, for T_2 to saturate at 1 for any positive input error, the input to the PWM generator must be increased by 1, as shown in Figure 4.5.

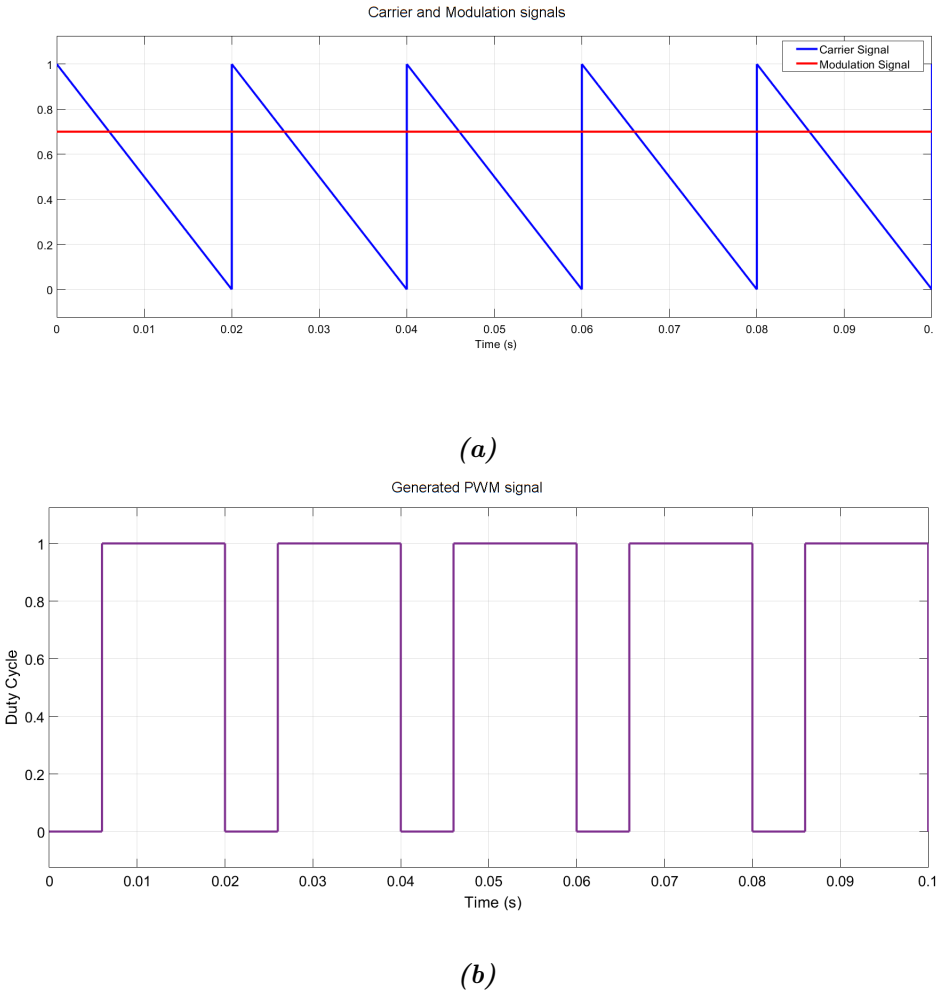

Figure 4.6: *Intersective PWM generation method. (a)Carrier and modulation signals and (b)Output PWM signal*

The reference voltage for the DC link capacitor is set at 750 V. The normalised error is calculated by dividing the difference between the measured and the reference voltage by

the reference voltage. This is used as the input of the PI control loop, which generates the pulse width modulated (PWM) signals for IGBTs T_1 and T_2. The method used to generate these signals is illustrated in Figures 4.6a and 4.6b. A sawtooth carrier signal is compared to a modulation signal, which in this case is the error, v^*. If the carrier signal has a larger value than the modulation signal, the output of the PWM generator is 0. Otherwise, it is 1. The chosen frequency of the carrier signal in this chapter is 1 kHz, which enables the generation of 100 pulses over a short simulation time of 0.1 seconds.

4.2 Simulation Scenarios

4.2.1 Magnet Storage Mode

In the first scenario, the load is disconnected from the DC link capacitor and the voltage and current are plotted in Figure 4.7 and 4.8. The simulation is carried over 0.1 seconds, during which switch T1 is off and switch T2 is on.

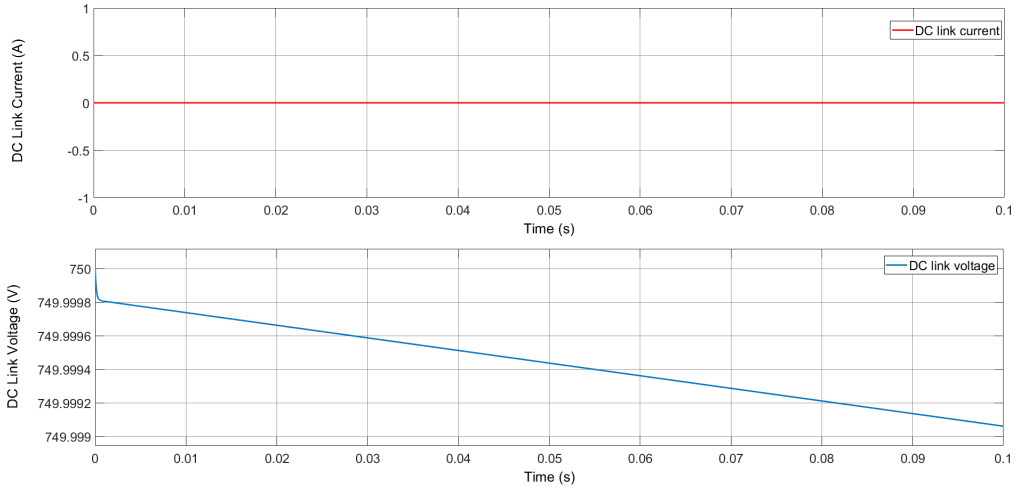

Figure 4.7: *DC link capacitor current and voltage during storage*

In the storage mode, current will decay due to the resistance of the solder joints between double pancake units, as well as due to the power converter diodes. A typical solder joint only has a resistance of $20n\Omega$ [24], leading to a loss of 0.065 W due to the joints. This is calculated as the product of the total joint resistance and the square of the peak current in the coil. Since current is passing through a diode with forward voltage of 0.7 V, the loss through the power converter during the storage mode is at most 319 W, calculated as the

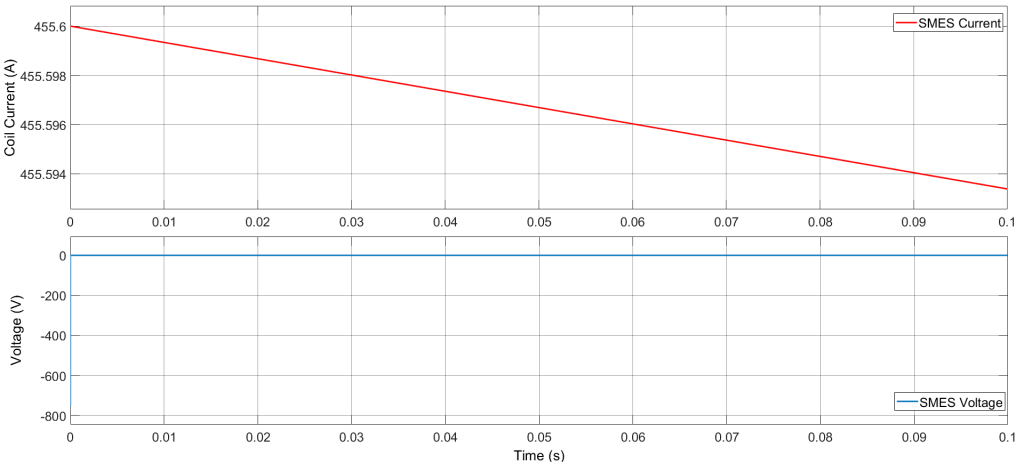

Figure 4.8: *Coil transport current and voltage during storage*

product between the peak coil current and the voltage drop through the diode. Based on the equation:

$$P_{loss} = V_{coil} I_{coil} = L \frac{\mathrm{d}I_{coil}}{\mathrm{d}t} I_{coil} \tag{4.3}$$

the maximum current decay is

$$\frac{\mathrm{d}I_{coil}}{\mathrm{d}t} = \frac{P_{loss}}{I_{coil} L} = 0.065 A/s \tag{4.4}$$

which is confirmed by the simulations, in figure 4.8.

4.2.2 Magnet Discharge Mode at 100 kW

In this scenario, a load is introduced in the circuit through a current source, controlled by a pulse generator. For a pulse duration of 0.1 s, and the load absorbs 133.3 A over a duty cycle of 20 % and a delay of 0.01 s. With the voltage of 750 V, the total power demand is 100 kW. As current is drawn, the capacitor voltage decreases, which is detected by the controller within 1 millisecond. In the first case, the proportional and integral gains in the PI controller are both 1. The magnet begins injecting current to compensate for the sudden power demand. At the end of the load duty cycle, the DC link voltage is stabilised from a minimum value of 600 V to just over 750 V within 0.05 seconds, as shown in Figure 4.9. The transport current in the magnet decreases by 0.35 A, as the coil delivers 95 J.

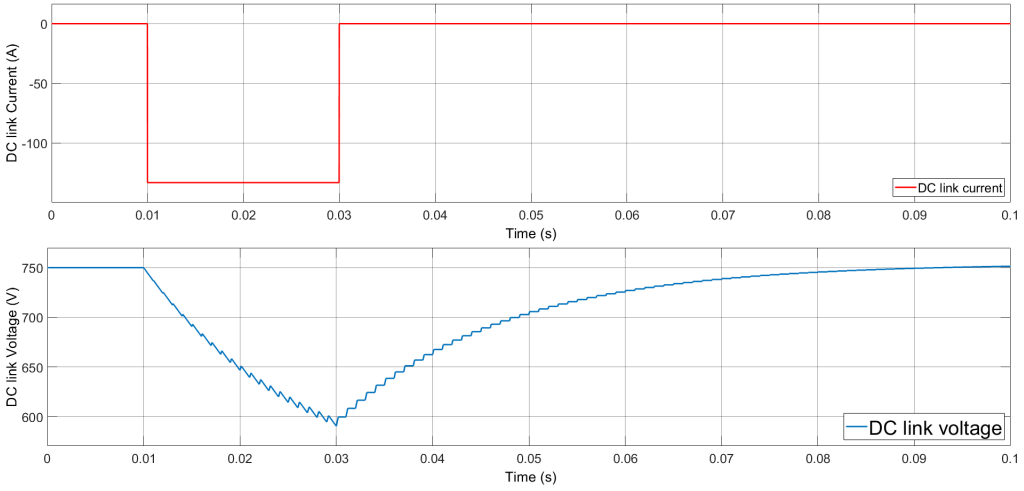

Figure 4.9: *DC link capacitor voltage and current during the compensation of a 100 kW load, with PI gains of 1*

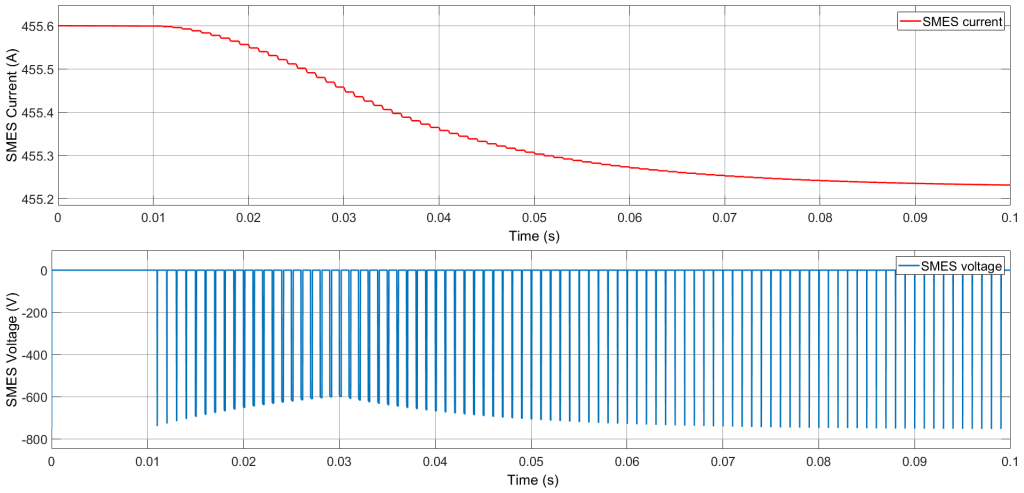

Figure 4.10: *Coil voltage and transport current during the compensation of a 100 kW load, with PI gains of 1*

Nevertheless, the DC link voltage dropped by 150 V, or 20 % relative to the reference value of 750 V. A way of reducing this difference is by adjusting the proportional and integral gain values in the PI controller. For $K_p = K_i = 100$, the compensation is improved, as seen in Figure 4.11.

This time, the DC link voltage only drops to at 743 V, or under 1% of the reference value. The SMES unit is injecting power into the capacitor, stabilising it after less than 0.4 seconds after the initial event.

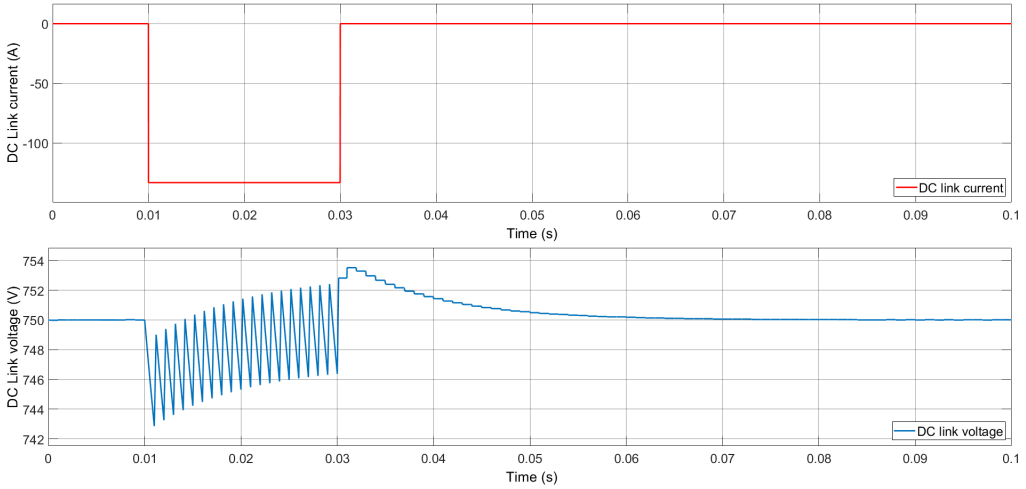

Figure 4.11: *DC link capacitor voltage and current during the compensation of a 100 kW load, with PI gains of 100*

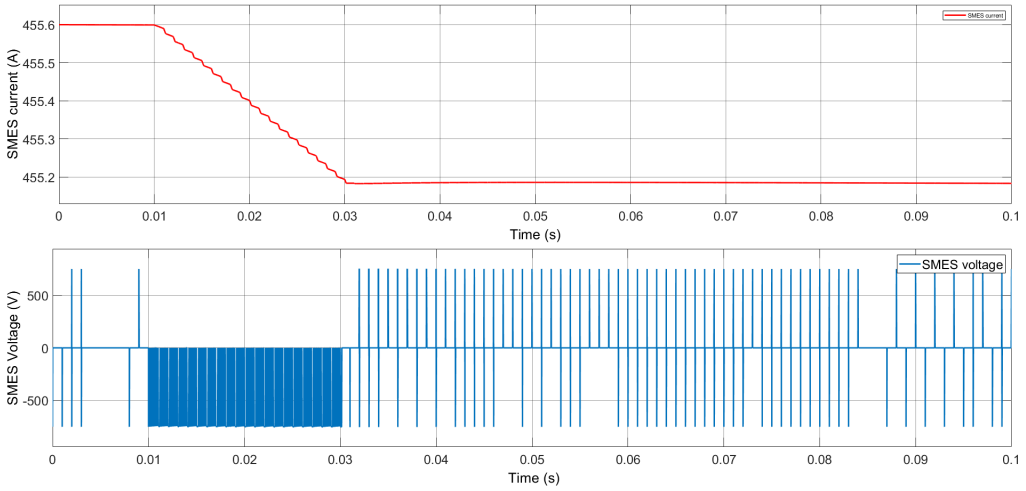

Figure 4.12: *Coil voltage and transport current during the compensation of a 100 kW load, with PI gains of 100*

If the SMES coil is not fully charged and the current is only 150 A, the duty cycle of the power converter is higher, as a higher voltage is required to compensate a 100 kW load. This scenario is illustrated in figures 4.13 and 4.14.

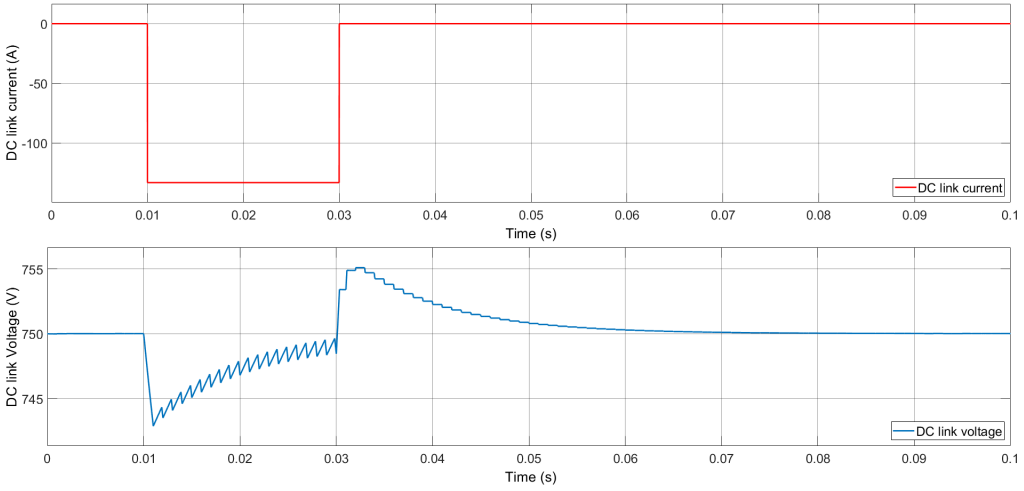

Figure 4.13: *DC link capacitor voltage and current during the compensation of a 100 kW load, with PI gains of 100 and a SMES current of 150A*

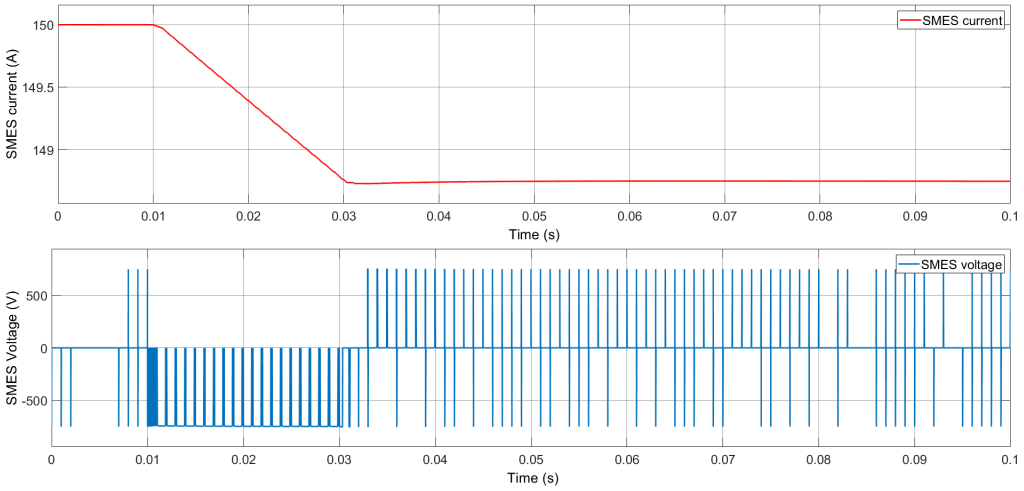

Figure 4.14: *Coil voltage and transport current during the compensation of a 100 kW load, with PI gains of 100, when the coil current starts at 150 A*

4.2.3 Magnet Charge Mode at 100 kW

In the last simulation, the load is converted in a generator, which injects a current with a constant magnitude of 133.33 A in the circuit, effectively raising the DC link capacitor voltage. This corresponds to a surplus power of 100 kW, which must be absorbed in order to prevent a further raise of DC link voltage. To achieve this, the magnet is operated in charge mode. As the coil absorbs the excess power, its transport current increases and the DC link capacitor voltage is stabilised. In this mode, the PI gains are both 100.

During the absorption of excess power, the transport current in the coil increases by 0.4 A. Since the critical current of this solenoid configuration is close to 600 A, there is a

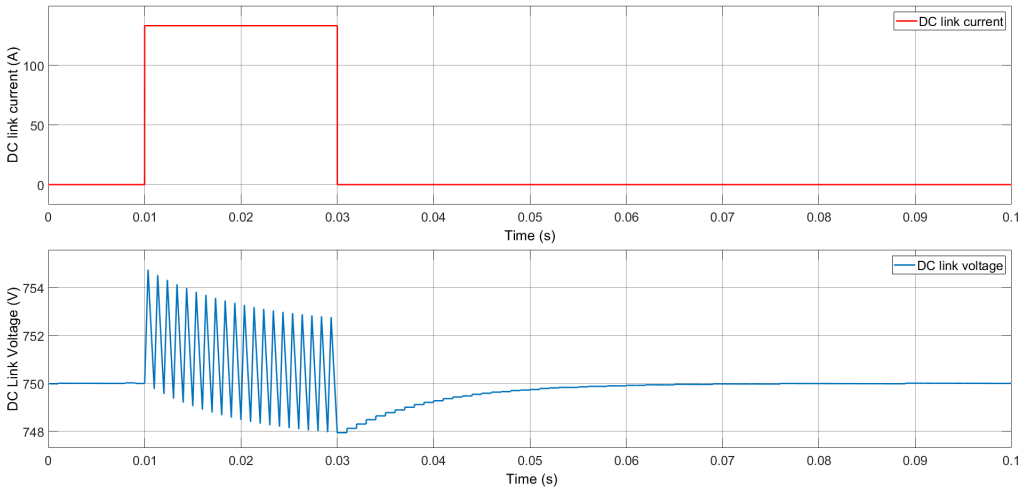

Figure 4.15: *DC link capacitor voltage and transport current during the compensation of a 100 kW excess power injection, with PI gains of 100*

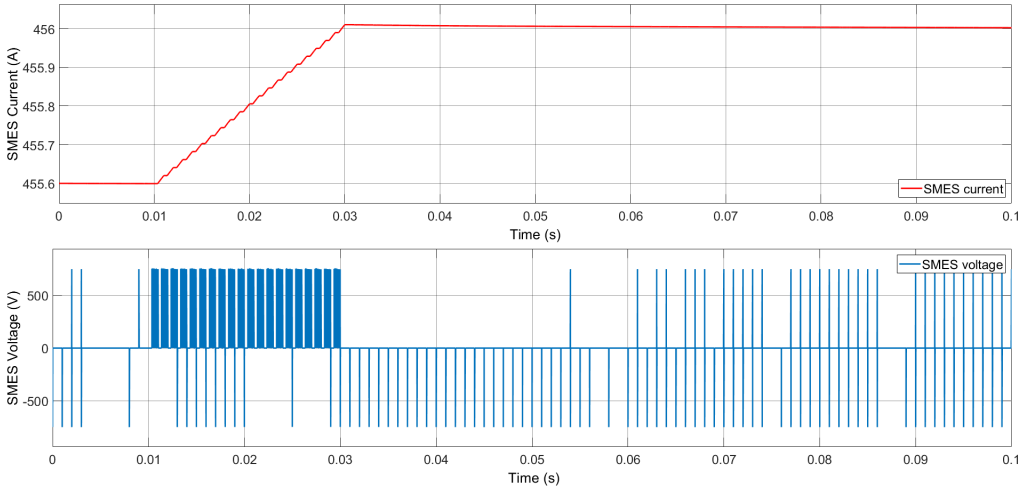

Figure 4.16: *Coil voltage and transport current during the compensation of a 100 kW excess power injection, with PI gains of 100*

sufficiently large margin to allow for further charging, if necessary. However, as a means of protection, a critical current limiter is necessary as part of the control circuit.

4.3 Summary

In this chapter, the 1 MJ/100 kW SMES unit previously designed is modelled as a part of a simplified DC microgrid, operating at 750 V. The coil is connected through a DC-DC converter, which is controlled through a PI loop in order to maintain the DC link voltage at 750V. Three operation scenarios are considered: storage, coil discharge and coil charge.

In the discharge mode, two different values are attributed to the PI gains and the outputs are compared, showing that a quicker compensation is achieved with $K_p = K_i = 100$ than for $K_p = K_i = 1$. A case in which the SMES coil is not fully charged is also considered, showing that the duty cycle of the converter must be increased to compensate for the 100 kW load.

Secondly, there is no definitive method that can determine the power limitation of a SMES unit as a function of its stored energy and transport current and whether there is an analytical relation between these values. Current knowledge suggests that the power output is limited by the rating of switches in the power converter [24], thus higher power outputs could be potentially obtained by using multilevel converters. This gives rise to the idea of combining the output of multiple smaller superconducting coils to achieve the same performance as a single large coil, as a potential cost-saving alternative.

Chapter 5

Conclusions and Further Work

5.1 Conclusions

In the context of an accelerated transition to renewable energy generation, maintaining the stability of future power systems is becoming a real challenge. High power energy storage systems are detrimental for balancing services, as they quickly compensate disturbances, preventing large fluctuations in frequency. As outlined in Chapter 1, superconducting magnetic energy storage using second generation high temperature materials is a promising technology that can fulfil this role in power systems balancing, either as a standalone installation, or in combination with other high energy technologies, such as Lithium-ion batteries. Nevertheless, 2G HTS SMES technology is still premature, due to the lack of large scale demonstrator projects and a general lack of clarity on the suitable methods that can be employed to optimally design a system, both from the magnet and the power converter points of view. This project proposes a simple method of designing a SMES coil, which considers its power output in addition to its energy storage capacity.

After a comprehensive theoretical background and literature review, presented in the first two chapters of this report, a design methodology for a high temperature superconducting magnet was proposed in Chapter 3. While numerous other design methods have been proposed in the literature, they are focused on obtaining a desired storage capacity, or a target magnetic field density, without considering the behaviour of the coil in a power system, or aspects such as stress/strain.

Besides the target energy stored, the method used in this project takes the power output and the voltage as inputs to the optimisation function. This is ensuring that the coil can reliably deliver the required value throughout the discharge process, with an energy efficiency of over 90 %. The process is then following a series of steps consisting in the choice of superconducting tape that can sustain the necessary current, while under magnetic field, the construction of parametric load lines using a combination of analytical and numerical methods, the calculation of inductance and maximum hoop stress in the solenoid, and finally, the discrete optimisation of the coil. The final design is using the lowest quantity of superconducting tape from all configurations calculated. Based on the initial constraints imposed, the number of combinations calculated is just below 1 million. In the particular case considered in this project, a coil that can deliver 1 MJ of energy at 100 kW and 750 V has been designed, with a resulting inductance of 10.72 H, a peak transport current of 455.6 A and a total length of tape of 8.14 km.

The design process was followed by a series of simulations using resulting properties of the coil in a simple DC microgrid model. In Chapter 4, the coil was emulated as a zero resistance inductor, used for compensating positive and negative pulsed power fluctuations, produced by an ideal current source. The power transfer was realised through a two quadrant DC-DC chopper, which allows a bidirectional energy flow to the coil. The objective of the control system, based on a PI controller, is to maintain the DC link voltage at a steady level of 750 V. When the current source was behaving as a load, drawing current, the SMES unit compensated by discharging gradually and injecting current. In this mode of operation, the output was plotted for two different values of the proportional and integral gains: 1 and 100, which showed that a faster settling time and a lower voltage drop were achievable with higher values of gain. Depending on the state of charge of the SMES unit, the power converter is chopping the voltage so that the output power equals the power draw from the load (100 kW in the particular case illustrated, with 750V and 133.3A). For example, when the coil was fully charged, at 455.6A, the DC link voltage of 750V was chopped with a duty cycle of 29.3%, which gradually increased as the coil was discharging.

5.2 Recommended Future Work

SMES is still an underdeveloped and overlooked technology that has immense potential of alleviating power imbalances and providing frequency regulation services, both in transmission and embedded systems. One key area that requires further development is the up-scaling of SMES units for different levels of power outputs, optimising not only the superconducting coil, but also the cooling system and the power converter unit.

The methodology proposed in Chapter 3 can be extended to consider continuous values of the parameters defining the shape factor of the coil, α and β. To do so, a FEA model of the coil is necessary, which would remove the reliance on numerical tables which only contain discrete values of α and β. This would lead to a true optimal set of coil parameters, instead of a near optimal, potentially showing a reduction in the required length of cable.

An optimal output would give an insight on the correlation between stored energy and maximum output power, which will further be used in modelling the entire storage system, comprised of both the coil and the power converter. As the output power is increased, the switches in the converter are subject to higher levels of voltage and current, which can potentially exceed their nominal limits. With typical values of peak voltage and current in modern IGBT switches of 6500 V and 1000 A, respectively [135], alternative chopper topologies, employing multiple switches, would have to be considered for high power single unit systems.

Another area of improvement is considering a multi-magnet system, which can potentially be an attractive solution for scaling up a SMES system, as the required transport current in each coil would be lower. While a multi-magnet SMES system was previously described in the literature [136], the main focus of the study was the coil design, without any consideration of the topology and control of the power converter. Multiple cases can be considered, including dividing the total energy between two, four and six coils. For these cases, the small coils will operate at the same temperature as the single large coil, giving the same critical current curve. Different converter topologies can be compared in terms of performance, losses and cost, including using a multi-input-single-output design or connecting each coil through an individual DC-DC chopper.

Appendix A

Field scaling factors

Table A.1: *Values of shape factors F, G and K depending on α and β. F is calculated using equation 3.15, G and K are determined from Figures 3.7 and 3.8, respectively.*

α	β	F(α, β)	G(α, β)	K(α, β)
1.08	0.25	2.3507E-08	2.45	0.94
1.08	0.5	4.3572E-08	1.61	0.91
1.08	0.75	5.8812E-08	1.29	0.87
1.08	1	6.9684E-08	1.166	0.84
1.08	1.5	8.2616E-08	1.063	0.78
1.08	2	8.9191E-08	1.0265	0.755
1.08	2.5	9.2818E-08	1.015	0.735
1.08	3	9.4984E-08	1.01	0.725
1.1	0.25	2.9125E-08	2.45	0.89
1.1	0.5	5.4051E-08	1.61	0.865
1.1	0.75	7.3059E-08	1.295	0.82
1.1	1	8.6674E-08	1.163	0.79
1.1	1.5	1.0295E-07	1.064	0.75
1.1	2	1.1126E-07	1.027	0.72
1.1	2.5	1.1586E-07	1.015	0.7
1.1	3	1.1861E-07	1.01	0.68
1.2	0.25	5.5835E-08	2.4	0.78
1.2	0.5	1.0418E-07	1.59	0.74
1.2	0.75	1.4172E-07	1.288	0.705
1.2	1	1.6914E-07	1.162	0.68
1.2	1.5	2.0268E-07	1.065	0.64
1.2	2	2.2020E-07	1.028	0.61
1.2	2.5	2.3002E-07	1.016	0.59
1.2	3	2.3594E-07	1.01	0.58

α	β	F(α, β)	G(α, β)	K(α, β)
1.3	0.25	8.0492E-08	2.25	0.73
1.3	0.5	1.5086E-07	1.55	0.675
1.3	0.75	2.0639E-07	1.29	0.64
1.3	1	2.4765E-07	1.172	0.615
1.3	1.5	2.9922E-07	1.067	0.575
1.3	2	3.2676E-07	1.03	0.55
1.3	2.5	3.4241E-07	1.017	0.54
1.3	3	3.5194E-07	1.01	0.53
1.4	0.25	1.0338E-07	2.05	0.7
1.4	0.5	1.9452E-07	1.52	0.65
1.4	0.75	2.6743E-07	1.285	0.6
1.4	1	3.2246E-07	1.165	0.57
1.4	1.5	3.9262E-07	1.07	0.535
1.4	2	4.3091E-07	1.032	0.515
1.4	2.5	4.5298E-07	1.017	0.5
1.4	3	4.6653E-07	1.01	0.485
1.6	0.25	1.4476E-07	1.9	0.645
1.6	0.5	2.7409E-07	1.49	0.6
1.6	0.75	3.7992E-07	1.28	0.55
1.6	1	4.6195E-07	1.164	0.525
1.6	1.5	5.7037E-07	1.106	0.485
1.6	2	6.3198E-07	1.065	0.465
1.6	2.5	6.6849E-07	1.034	0.45
1.6	3	6.9131E-07	1.018	0.445
2.1	0.25	2.2940E-07	1.69	0.575
2.1	0.5	4.3887E-07	1.42	0.535
2.1	0.75	6.1696E-07	1.24	0.5
2.1	1	7.6166E-07	1.152	0.47
2.1	1.5	9.6667E-07	1.073	0.425
2.1	2	1.0935E-06	1.038	0.4
2.1	2.5	1.1736E-06	1.0215	0.38
2.1	3	1.2260E-06	1.01	0.37
2.6	0.25	2.9611E-07	1.58	0.52
2.6	0.5	5.7007E-07	1.35	0.5
2.6	0.75	8.0856E-07	1.21	0.47
2.6	1	1.0083E-06	1.145	0.44
2.6	1.5	1.3052E-06	1.073	0.4
2.6	2	1.5010E-06	1.04	0.375
2.6	2.5	1.6316E-06	1.0235	0.355
2.6	3	1.7207E-06	1.01	0.34
3.1	0.25	3.5115E-07	1.5	0.485
3.1	0.5	6.7890E-07	1.3	0.475
3.1	0.75	9.6881E-07	1.19	0.445

α	β	F(α, β)	G(α, β)	K(α, β)
3.1	1	1.2167E-06	1.13	0.425
3.1	1.5	1.5983E-06	1.07	0.38
3.1	2	1.8623E-06	1.04	0.36
3.1	2.5	2.0461E-06	1.024	0.345
3.1	3	2.1764E-06	1.01	0.335

Appendix B

Coil Optimisation Code

```
wd <- getwd()

# Define the initial variables

F <- read.csv(paste0(wd,"/F.csv"),header = FALSE)
G <- read.csv(paste0(wd,"/G.csv"),header = FALSE)
K <- read.csv(paste0(wd,"/K.csv"),header = FALSE)

T <- F*G*K

mu0 <- 4*pi*1E-7

# Tape parameters

# dimensions

t0 <- 0.0001
w0 <- 0.012
insu <- 2.5*1E-6
t <- t0 + 2*insu
w <- w0 + 2*insu

# safety factor, fill factor and efficiency

```

```
s <- 0.8
f <- 0.75
eta <- 0.9

# Critical curve parameters

a1 <- 275.76
b1 <- 1555.825
c1 <- -0.32

a2 <- 143.32
b2 <- 920.9
c2 <- -0.162


# Shape factors alpha and beta

alpha_vector <- c(1.08,1.1,1.2,1.3,1.4,1.6,2.1,2.6,3.1)
beta_vector <- c(0.25,0.5,0.75,1,1.5,2,2.5,3)


# Constraints

B_min <- 2
B_step <- 0.01

r_min <- 0.01
r_max <- 1
r_step <- 0.01

stress_max <- 550

# Define the functions

# critical current and critical field

critical_current <- function(B){
```

```
1061   if(B<=8){
1062   return (round(a1+b1*exp(c1*B),digits = 2))}
1063   else if (B>8 & B<= 16) {
1064   return (round(a2+b2*exp(c2*B),digits = 2))}
1065   else {print("The magnetic field density is too large!")}
1066 }
1067
1068
1069 critical_field <- function(I){
1070   if (I>=396 & I<1100){
1071   return (round(log((I-a1)/b1)/c1,digits = 2))}
1072   else if (I<396 & I>=143){
1073   return (round(log((I-a2)/b2)/c2,digits = 2))}
1074   else if (I<143) {print("The current is too low!")}
1075   else {print("The current is too high!")}
1076 }
1077
1078
1079 # Load line current
1080
1081 load_line_current <- function(B, fgk, ri){
1082   return ((t*w)/(s*f)*(B/(fgk*ri)))
1083 }
1084
1085
1086 # ------------------------------Working point--------------
1087
1088 working_point <- function(B,fgk,ri){
1089   return(critical_current(B) - load_line_current(B,fgk,ri))
1090 }
1091
1092
1093 # Stress function
1094
1095 stress <- function(a1, B, k, fgk){
1096   round(B^2/(fgk*k)*1/(a1-1)*((2*a1*(7*a1^2+a1+1))/
1097   (9*(a1+1))-(5*a1^2+1)/6)/1E6,2)
```

```
}

# tape length formula

tape_length <- function(alpha,beta, ri){
  return((2*pi*f*(alpha^2-1)*beta*ri^3)/(t*w))
}

# ----------------------Inductance using Welsby formula----

# Shape dependent factor

Kn <- function(alpha,beta){
  return (((alpha+1)^2)/(1+(0.9*(alpha+1)/(4*beta))+
              (0.64*(alpha-1)/(alpha+1))+
                        (0.84*(alpha-1)/(2*beta))))
}

# Number of turns in the coil as a function of alpha,
# beta and inner radius

turns <- function(alpha, beta, ri){
  N <- (2*beta*(alpha-1)*ri^2*f/(t*w))
  return(as.integer(N))
}

# Inductance formula

inductance <- function(alpha, beta, ri){
  return(Kn(alpha,beta)*(turns(alpha,beta,ri)**2)*
           (pi^2)*ri/(2*beta)*1E-7)
}


# Stored energy
energy_stored <- function(alpha, beta, B, fgk,ri){
  return(0.5 * inductance(alpha, beta, ri) *
```

```
  (load_line_current(B,fgk,ri))^2)
}


# ------------------------Search function-----------------
#
# results <- data.frame(0,0,0,0,0)
# colnames(results)<-c("alpha", "beta", "Inner Radius",
# "Inductance","Tape Length")


coil_configuration <- function(Energy, Power, Voltage){

  # Upper bound for tape length (in metres)
  l_max <- 1E6

  # Target energy stored
  E_target <- Energy/eta

  # Minimum required current
  I_min <- Power/Voltage

  # Minimum required peak operating current to achieve efficiency
  I_op_min <- I_min/sqrt(1-eta)

  # Minimum critical current required, considering stress factor
  I_crit <- I_op_min/s

  # Critical field
  B_crit <- critical_field(I_crit)

  for (i in 1:nrow(T)){
    for (j in 1:ncol(T)){
      for (ri in seq(r_min, r_max, r_step)){
        for (B in seq(B_min, B_crit, B_step)){

          # Calculate inductance
```

```
1172            L <- inductance(alpha_vector[i], beta_vector[j], ri)
1173            #print(L)
1174
1175            I_op <- load_line_current(s*B, T[i,j],ri)
1176
1177            # Calculate stored energy
1178            E_stored <- 0.5*L*I_op^2
1179            #print(E_stored)
1180
1181            # Calculate stress
1182            stress_cfg <- stress(alpha_vector[i], B*s, K[i,j], T[i,j])
1183
1184            # Calculate tape length in the current configuration
1185            length_cfg <- tape_length(alpha_vector[i], beta_vector[j], ri)
1186
1187            # Check whether parameters are in line with the requirements
1188            if (working_point(B,T[i,j],ri) > 0 &
1189                E_stored >= E_target &
1190                stress_cfg < stress_max*s&
1191                l_max > length_cfg &
1192                I_op/s > I_crit){
1193
1194                  # Store minimum length in the variable
1195                  l_max = length_cfg
1196                  # Store energy
1197                  e_mem = E_stored
1198                  # Store inductance
1199                  L_mem = L
1200                  # Store stress
1201                  stress_mem = stress_cfg
1202                  # Store alpha, beta and radius
1203                  alpha_mem = alpha_vector[i]
1204                  beta_mem = beta_vector[j]
1205                  r_mem = ri
1206                  #Store indices
1207                  i_mem = i
1208                  j_mem = j
```

```
1209                    # Store perpendicular field
1210                    B_mem = B
1211                    # Store current
1212                    I_mem = load_line_current(B,T[i,j],ri)
1213
1214                    I_op_mem = I_op
1215                    I_critical_curve = critical_current(B)
1216                    I_crit_mem = I_crit
1217
1218                }
1219              }
1220            }
1221          }
1222        }
1223
1224        cat("Magnetic Field (T):",B_mem,"\n",
1225            "Tape Length (m):", l_max,"\n",
1226            "Inner Radius (m):", r_mem,"\n",
1227            "Alpha value:", alpha_mem,"\n",
1228            "Beta value:", beta_mem,"\n",
1229            "Inductance (H):",L_mem,"\n",
1230            "Stored Energy (kJ):", e_mem/1000,"\n",
1231            "Load Line current Current (A):", I_mem,"\n",
1232            "Operating Current (A):", I_op_mem,"\n",
1233            "Minimum Critical curve Current (A):", I_crit_mem,"\n","\n")
1234
1235 }
```

Appendix C

Stress equation

As outlined in [37], the analytical formulation of stress equilibrium in a solenoid is expressed as:

$$\frac{1}{\epsilon}\frac{\mathrm{d}}{\mathrm{d}\epsilon}\left\{\epsilon\frac{\mathrm{d}w}{\mathrm{d}\epsilon}\right\} - \frac{w}{\epsilon^2} = -Q + M\epsilon \tag{C.1}$$

The hoop and radial stresses are given by:

$$\sigma_\theta = \frac{w}{\epsilon} + \nu\frac{\mathrm{d}w}{\mathrm{d}\epsilon} \tag{C.2}$$

and

$$\sigma_r = \frac{\mathrm{d}w}{\mathrm{d}\epsilon} + \nu\frac{w}{\epsilon} \tag{C.3}$$

Here, Y is Young's modulus for the coil, ν is Poisson's ratio, ϵ is the normalised radius, $\frac{r}{R_i}$ and $w = \frac{uY}{R_i(1-\nu^2)}$, where u is the local radial displacement. In equation C.1, $Q = \frac{(\alpha B_{in} - B_{out})JR_i}{\alpha - 1}$ and $M = \frac{(B_{in} - B_{out})JR_i}{\alpha - 1}$, with B_{in} and B_{out} being the internal and external axial magnetic field densities, J the transport current density and α the ratio between the external and internal diameter of the coil.

Starting from the solution of equation C.1:

$$w = C\epsilon + \frac{D}{\epsilon} - \frac{Q\epsilon^2}{3} + \frac{M\epsilon^3}{8} \tag{C.4}$$

constants C and D can be expressed in terms of Q and M by considering the boundary conditions for the radial stress. Hence, the radial stress is considered 0 at both the internal and external surface of the coil, specifically where $r = R_i$ and $r = R_{out} = \alpha R_i$. Under these conditions, $\epsilon = 1$ or $\epsilon = \alpha$.

Using equation C.4,

$$\frac{\mathrm{d}w}{\mathrm{d}\epsilon} = C - \frac{D}{\epsilon^2} - \frac{2Q\epsilon}{3} + \frac{3M\epsilon^2}{8} \tag{C.5}$$

Equation C.3 becomes:

$$\begin{aligned}\sigma_r &= C - \frac{D}{\epsilon^2} - \frac{2Q\epsilon}{3} + \frac{3M\epsilon^2}{8} + \nu\Big(C + \frac{D}{\epsilon^2} - \frac{Q\epsilon}{3} + \frac{M\epsilon^2}{8}\Big) = \\ &= C(1+\nu) - \frac{D}{\epsilon^2}(1-\nu) - Q\epsilon\Big(\frac{2+\nu}{3}\Big) + M\epsilon^2\Big(\frac{3+\nu}{8}\Big)\end{aligned} \tag{C.6}$$

For $\epsilon = 1$, equation C.6 becomes:

$$\sigma_r = C(1+\nu) - D(1-\nu) - Q\Big(\frac{2+\nu}{3}\Big) + M\Big(\frac{3+\nu}{8}\Big) = 0 \tag{C.7}$$

For $\epsilon = \alpha$:

$$\sigma_r = C(1+\nu) - \frac{D}{\alpha^2}(1-\nu) - Q\alpha\Big(\frac{2+\nu}{3}\Big) + M\alpha^2\Big(\frac{3+\nu}{8}\Big) = 0 \tag{C.8}$$

By combining equations C.7 and C.8:

$$C = \frac{1}{1+\nu}\left(Q\frac{\alpha^2(2+\nu) + (2+\nu)(1-\nu)(\alpha+1)}{3(1-\nu)(\alpha+1)} - M\frac{\alpha^2(3+\nu)+1}{8}\right) \tag{C.9}$$

and

$$D = Q\frac{\alpha^2(2+\nu)}{3(1-\nu)(\alpha+1)} - M\frac{\alpha^2(3+\nu)}{8(1-\nu)} \tag{C.10}$$

After substituting C and D in equation C.2:

$$\sigma_\theta = \frac{Q(2+\nu)}{3(\alpha+1)}\left\{\alpha^2+\alpha+1+\frac{\alpha^2}{\epsilon^2} - \epsilon\frac{(1+2\nu)(\alpha+1)}{(2+\nu)}\right\} - \frac{M(3+\nu)}{8}\left\{\alpha^2+1+\frac{\alpha^2}{\epsilon^2} - \frac{1+3\nu}{(3+\nu)}\epsilon^2\right\} \tag{C.11}$$

To further simplify this form, it can be assumed that $B_{out} = 0$, thus

$$Q = \frac{\alpha B_{in} J R_i}{\alpha - 1}$$

and

$$M = \frac{B_{in} J R_i}{\alpha - 1} = \frac{Q}{\alpha}$$

Here, $B_{in} = B_{\parallel,max}$ and is the maximum axial field density. For consistency, the axial field is expressed in terms of the radial field as $B_{in} = \frac{B_\perp}{K(\alpha,\beta)}$, leading to:

$$Q = \frac{\alpha}{\alpha - 1} \frac{B_\perp^2}{F(\alpha,\beta)G(\alpha,\beta)K(\alpha,\beta)^2}$$

and

$$M = \frac{1}{\alpha - 1} \frac{B_\perp^2}{F(\alpha,\beta)G(\alpha,\beta)K(\alpha,\beta)^2}$$

Also, it can be assumed that $\nu = 1/3$, which is a typical approximation for most materials [37]. Given these, the hoop stress can be expressed as:

$$\sigma_\theta = \frac{B_\perp^2}{F(\alpha,\beta)G(\alpha,\beta)K(\alpha,\beta)^2} \frac{1}{(\alpha-1)} \left\{ \frac{7\alpha}{9(\alpha+1)} \left[\alpha^2 + \alpha + 1 - \frac{\alpha^2}{\epsilon^2} - \frac{5}{7}(\alpha+1)\epsilon \right] \right.$$

$$\left. - \frac{5}{12} \left[\alpha^2 + 1 + \frac{\alpha^2}{\epsilon^2} - \frac{3}{5}\epsilon^2 \right] \right\} \tag{C.12}$$

The peak hoop stress is achieved at $\epsilon = 1$, therefore:

$$\sigma_{\theta,max} = \frac{B_\perp^2}{F(\alpha,\beta)G(\alpha,\beta)K(\alpha,\beta)^2} \frac{1}{(\alpha-1)} \left\{ \frac{7\alpha}{9(\alpha+1)} \left[2\alpha^2 + \frac{2}{7}(\alpha+1) \right] - \frac{5}{12} \left(2\alpha^2 + \frac{2}{5} \right) \right\}$$

$$= \frac{B_\perp^2}{F(\alpha,\beta)G(\alpha,\beta)K(\alpha,\beta)^2} \frac{1}{(\alpha-1)} \left\{ \frac{2\alpha(7\alpha^2 + \alpha + 1)}{9(\alpha+1)} - \frac{5\alpha^2 + 1}{6} \right\} \tag{C.13}$$

References

[1] V. Smil. *Energy and civilization: a history*. The MIT press, 2017. ISBN 978-0-26203-577-4.

[2] J. Rogelj, M. de Elzen, N. Hohne, T. Fransen, H. Fekete, H. Wingler, R. Schaeffer, F. Sha, K. Riahi, and M. Meinshausen. Paris Agreement climate proposals need a boost to keep warming below 2C. *Nature*, 534:631–639, 2016. DOI: 10.1038/nature18307.

[3] Department of Energy and Climate Change. UK Renewable Energy Roadmap 2013 Update. Technical report, November 2013.

[4] Renewable Energy Foundation. Escalating UK Grid Management Costs: Consumers Feel the Chill of Sub-Zero Electricity Prices, 2020. https://www.ref.org.uk/ref-blog/361-escalating-uk-grid-management-costs-consumers-feel-the-chill-of-sub-zero-electricity-prices, [Accessed 24 June 2020].

[5] F. Daz-Gonzlez, A. Sumper, O. Gomis-Bellmunt, and R. Villaffila-Robles. A review of energy storage technologies for wind power applications. *Renewable and Sustainable Energy Reviews*, 16:2154–2171, 2012. DOI: 10.1016/j.rser.2012.01.029.

[6] X. Luo, J. Wang, M. Dooner, and J. Clarke. Overview of current development in electrical energy storage technologies and the application potential in power system operation. *Applied Energy*, 137:511–536, 2015. DOI: 10.1016/j.apenergy.2014.09.081.

[7] S. Sabihuddin, A.E. Kiprakis, and M. Mueller. A Numerical and Graphical Review of Energy Storage technologies. *Energies*, 8:172–216, 2015. DOI: 10.3390/en8010172.

[8] C. Randall. Rimac's hypercar CTwo faster than Tesla Roadster, 2018. https://www.electrive.com/2018/03/07/rimac-hypercar-c_two-faster-tesla-roadster/, [Accessed 23 September 2019].

[9] P. Nikolaidis and A. Poullikkas. Cost metrics of electrical energy storage technologies in potential power system operations. *Sustainable Energy Technologies and Assessments*, 25:43–59, 2018. DOI: 10.1016/j.seta.2017.12.001.

[10] Electric Mountain. Dinorwig Power Station. http://www.electricmountain.co.uk/Dinorwig-Power-Station/, [Accessed 12 Mar 2018].

[11] H. Zeng et al. Introduction of Australian 100MW Storage Operation and its Enlightenment to China. In *Proceedings of the 2018 China International Conference on Electricity Distribution)*, Tianjin, China, 2018. DOI: 10.1109/CICED.2018.8592035.

[12] M. Budt, D. Wolf, R. Span, and J. Yan. A review on compressed air energy storage: basic principles, past milestones and recent developments. *Applied Energy*, 170: 250–268, 2016. DOI: 10.1016/j.apenergy.2016.02.108.

[13] H. Chen, T.N. Cong, W. Yang, C. Tan, Y. Li, and Y. Ding. Progress in electrical energy storage system: A critical review. *Progress in Natural Science*, 19:291–312, 2009. DOI: 10.1016/j.pnsc.2008.07.014.

[14] C.R. Birkl, M.R. Roberts, E. McTurk, P.G. Bruce, and D.A. Howey. Degradation diagnostics for lithium ion cells. *Journal of Power Sources*, 341:373–386, 2017. DOI: 10.1016/j.jpowsour.2016.12.011.

[15] M. Farhadi and O. Mohammed. Energy Storage Technologies for High-Power Applications. *IEEE Transactions on Industry Applications*, 52(3):1953–1961, 2016. DOI: 10.1109/TIA.2015.2511096.

[16] T. Bocklisch. Hybrid energy storage approach for renewable energy applications. *Journal of Energy Storage*, 8:311–319, 2016. DOI: 10.1016/j.est.2016.01.004.

[17] M. Aneke and M. Wand. Energy storage technologies and real life applications - A state of the art review. *Applied Energy*, 179:350–377, 2016. DOI: 10.1016/j.apenergy.2016.06.097.

[18] J. Baker. New Technology and possible advances in energy storage. *Energy Policy*, 36:4368–4373, 2008. DOI: 10.1016/j.enpol.2008.09.040.

[19] A. Gonzlez, E. Goikolea, J.A.i Battena, and R. Mysyk. Review on supercapacitors: Technologies and materials. *Renewable and Sustainable Energy Reviews*, 58: 1189–1206, 2016. DOI: 10.1016/j.rser.2015.12.249.

[20] L. Chen, Y. Liu, A.B. Arsoy, P.F. Ribeiro, M. Steurer, and M.R. Irvani. Detailed Modeling of Superconducting Magnetic Energy Storage (SMES) System. *IEEE Transactions of Power Delivery*, 21(2):699–710, 2006. DOI: 10.1109/TPWRD.2005.864075.

[21] B.Gholizad. *Superconducting technology for power and energy management.* PhD thesis, University of Bologna, 2016.

[22] A. Morandi, B. Gholizad, and M. Fabbri. Design and performance of a 1MW-5s high temperature superconductor magnetic energy storage system. *Superconductor Science and Technology*, 29(2):015014, 2016. DOI: 10.1088/0953-2048/29/1/015014.

[23] A. Gabriel-Buenaventura and B. Azzopardi. Energy recovery systems for retrofitting in internal combustion enginevehicles: A review of techniques. *Renewable and Sustainable Energy Reviews*, 41:955–964, 2015. DOI: 10.1016/j.rser.2014.08.083.

[24] Z. Melhem. *High Temperature Superconductors for energy applications.* Woodhead Publishing Series in Energy, 2012. ISBN 978-0-85709-012-6.

[25] W. Buckles and W.V. Hassenzahl. Superconducting Magnetic Energy Storage. *IEEE Power Engineering Review*, 20(5):16–20, 2000. DOI: 10.1109/39.841345.

[26] Y.F. Bi. Cooling and Cryocoolers for HTS Power Applications. *Applied Superconductivity and Electromagnetics*, 4(1):97–108, 2013.

[27] R. Navarro. Hundred Years of Superconducting Materials. In *Second International Conference of Energy Engineering (ICEE-2)*, Aswan, Egypt, 2010.

[28] J-X. Jin, X-Y. Chen, Y. Xin, and Y-W. Sun. Theoretical Modeling and Simulation of Magnetic Energy Storage System. In *Proceedings of the 29th Chinese Control Conference*, Beijing, China, 2010.

[29] M.H. Ali, B. Wu, and R.A. Dougal. An Overview of SMES applications in power and energy systems. *IEEE Transactions on Sustainable Energy*, 1(1):38–47, 2010. DOI: 10.1109/TSTE.2010.2044901.

[30] V. Monteiro, J.G. Pinto, B. Exposto, and J.L. Alfonso. Comprehensive Comparison of a Current-Source and a Voltage-Source Converter for Three-Phase EV Fast Battery Chargers. In *Proceedings of the 9th International Conference on Compatibility and Power Electronics*, Costa da Caparica, Portugal, 2015. DOI: 10.1109/CPE.2015.7231068.

[31] Y. Xie, M. Song, J. Shi, G. Jiang, P. Geng, and M. Zhang. Simulation on a micro-grid system based on superconducting magnetic energy storage. In *Proceedings of the 2014 International Power Electronics and Application Conference and Exposition*, Shanghai, China, 2014. DOI: 10.1109/PEAC.2014.7038078.

[32] J. Li, R. Xiong, Q. Yang, F. Liang, M. Zhang, and W. Yuan. Design/test of a hybrid energy storage system for primary frequency control using a dynamic droop method in an isolated microgrid power system. *Applied Energy*, 201:257–269, 2017. DOI: 10.1016/j.apenergy.2016.10.066.

[33] J. Zhu, W. Yuan, T.A. Coombs, and Q. Ming. Simulation and experiment of a YBCO SMES prototype in voltage sag compensation. *Physica C*, 471:199–204, 2014. DOI: 10.1016/j.physc.2010.12.015.

[34] L. Chen, H. Chen, J. Yang, H. He, Y. Yu, G. Li, Y. Xu, Z. Wang, and L. Ren. Conceptual Design and Evaluation of an HTS Magnet for an SMES Used in Improving Transient Performance of a Grid-Connected PV System. *IEEE Transactions on Applied Superconductivity*, 28(3), 2018. DOI: 10.1109/TASC.2017.2783349.

[35] L. Chen, H. Chen, Y. Li, G. Li, J. Yang, X. Liu, Y. Xu, L. Ren, and Y. Tang. SMES-Battery Energy Storage System for the Stabilization of a Photovoltaic-Based Microgrid. *IEEE Transactions on Applied Superconductivity*, 28(4), 2018. DOI: 10.1109/TASC.2018.2799544.

[36] J. Li, Q. Yang, F. Robinson, F. Liang, M. Zhang, and W. Yuan. Design and test of a new droop control algorithm for a SMES/battery hybrid energy storage system. *Energy*, 118(1):1110–1122, 2017. DOI: 10.1016/j.energy.2016.10.130.

[37] M. Wilson. *Superconducting Magnets*. Oxford University Press, 1983. ISBN 978-0-19854-810-2.

[38] J.D.D. Gawith, J. Ma, B. Shen, C. Li, J. Yang, Y. Ozturk, and T. Coombs. An HTS Power Switch Using YBCO Thin Film Controlled by AC Magnetic Field. *Supercond. Sci. Technol*, 32, 2019. DOI: 10.1088/1361-6668/ab2d61.

[39] E. Hoffmann, J. Alcorn, W. Chen, Y-H. Hsu, J. Purcell, and R. Schermer. Design of the BPA Superconducting 30 MJ Energy storage coil. *IEEE Transactions on Magnetics*, MAG-17(1):521–524, 1981. DOI: 10.1109/TMAG.1981.1060923.

[40] C.A. Luongo, T. Baldwin, P. Ribeiro, and C.M. Weber. A 100 MJ SMES Demonstration at FSU-CAPS. *IEEE Transactions on Applied Superconductivity*, 13(2):1800–1805, 2003. DOI: 10.1109/TASC.2003.812894.

[41] S. Nagaya, N. Hirano, M. Kondo, T. Tanaka, H. Nakabayashi, K. Shikimachi, S. Hanai, J. Inagaki, S. Ioka, and S. Kawashima. Development and Performance Results of 5MVA SMES for Bridging Instantaneous Voltage Dips. *IEEE Transaction on Applied Superconductivity*, 14(2):699–704, 2004. DOI: 10.1109/TASC.2004.830076.

[42] W.V. Hassenzahl, D.W. Hazelton, B.K. Johnson, P. Komarek, M. Noe, and C.T. Reis. Electric Power Applications of Superconductivity. *Proceedings of the IEEE*, 92(10), 2004.

[43] Q. Wang, Y. Dai, B. Zhao, S. Song, Z. Cao, S. Chen, Q. Zhang, H. Wang, J. Cheng, Y. Lei, X. Li, J. Liu, S. Zhao, H. Zhang, G. Xu, Z. Yang, X. Hu, H. Liu, C. Wang, and L. Yan. Development of Large Scale Superconducting Magnet with Very Small Stray Magnetic Field. *IEEE Transaction on Applied Superconductivity*, 20(3):1352–1355, 2010. DOI: 10.1109/TASC.2009.2039471.

[44] H.J. Kim, K.C. Seong, J.W. Cho, J.H. Bae, K.D. Sim, S. Kim, E.Y. Lee, K. Ryu, and S.H. Kim. 3MJ-750kVA SMES System for Improving Power Quality. *IEEE Transaction on Applied Superconductivity*, 16(2):574–577, 2006. DOI: 10.1109/TASC.2006.871329.

[45] L. Ottonello, G. Canepa, P. Albertelli, E. Picco, A. Florio, G. Masciarelli, S. Rossi, L. Martini, C. Pincella, A. Mariscotti, E. Torello, A. Martinolli, and M. Mariani. The Largest Italian SMES. *IEEE Transaction on Applied Superconductivity*, 16(2): 602–607, 2006. DOI: 10.1109/TASC.2005.869677.

[46] W-S. Kim, S-Y. Kwak, J-K. Lee, K-D. Choi, H-K. Jung, K-C. Seong, and S-Y. Hahn. Design of HTS Magnets for a 600 kJ SMES. *IEEE Transaction on Applied Superconductivity*, 16(2):620–623, 2006. DOI: 10.1109/TASC.2005.864244.

[47] K. Shikimaki, H. Moriguchi, N. Hirano, S. Nagaya, T. Ito, J. Ingaki, S. Hanai, M. Takahashi, and T. Kurusu. Development of MVA Class HTS SMES System for Bridging Instantanous Voltage Dips. *IEEE Transaction on Applied Superconductivity*, 15(2):1931–1934, 2005. DOI: 10.1109/TASC.2005.849338.

[48] P. Tixador, B. Bellin, M. Deleglise, J.C. Vallier, C.E. Bruzek, A. Allais, and J.M. Saugrain. Design and First Tests of a 800kJ HTS SMES. *IEEE Transaction on Applied Superconductivity*, 17(2):1967–1972. DOI: 10.1109/TASC.2007.898520.

[49] W. Yuan. *Second-Generation High-Temperature Superconducting Coils and Their Applications for Energy Storage*. PhD thesis, University of Cambridge, 2011.

[50] Y. Li, P. Song, Y. Kang, F. Feng, and T. Qu. Design of a 30-K/4-kJ HTS Magnet Cryocooled with Solid Nitrogen. *IEEE Transaction on Applied Superconductivity*, 28(4), 2018. DOI: 10.1109/TASC.2018.2814960.

[51] Z-X. Zheng, X-Y. Chen, X-Y. Xiao, and C-J. Huang. Design and Evaluation of a Mini-Size SMES Magnet for Hybrid Energy Storage Application in a kW-Class Dynamic Voltage Restorer. *IEEE Transaction on Applied Superconductivity*, 27(7), 2017. DOI: 10.1109/TASC.2017.2748954.

[52] Z-X. Zheng, X-Y. Xiao, C-J. Huang, and C s. Li. Design and Evaluation of a kW-class SMES-BES DVR System for mitigation of power quality disturbances. In *2017 IEEE International Conference on Environment and Electrical Engineering and 2017 IEEE Industrial and Commercial Power Systems Europe*. IEEE, 2017. DOI: 10.1109/EEEIC.2017.7977603.

[53] K. Koyanagi, K. Ohsemochi, M. Takahashi, T. Tosaka, M. Ono, Y. Ishii, K. Shimada, S. Nomura, K. Kidoguchi, H. Onoda, N. Hirano, and S. Nagaya. Design of a High Energy-Density SMES Coil With Bi-2212 Cables. *IEEE Transaction on Applied Superconductivity*, 16(2):586–589, 2006. DOI: 10.1109/TASC.2005.869647.

[54] T. Tosaka, K. Koyanagi, K. Ohsemochi, M. Takahashi, Y. Ishii, M. Ono, H. Ogata, K. Nakamoto, H. Takigami, S. Nomura, K. Kidoguchi, H. Onoda, N. Hirano, and S. Nagaya. Excitation Tests of Prototype HTS Coil with Bi2212 Cables for Development of High Energy Density SMES. *IEEE Transaction on Applied Superconductivity*, 17(2):2010–2013, 2007. DOI: 10.1109/TASC.2007.899871.

[55] J. Zhu, M. Qiu, B. Wei, Ho. Zhang, X. Lai, and W. Yuan. Design, Dynamic Simulations and construction of a hybrid HTS SMES for Chinese power grid. *Energy*, 51:184–192, 2013. DOI: 10.1016/j.energy.2012.09.044.

[56] V.E. Sytnikov, V.S. Vysotsky, I.P. Radchenko, and N.V. Polyakova. 1G versus 2G-comparison from the practical standpoint for HTS power cables use. In *Proceedings of the 8th European Conference on Applied Superconductivity (EUCAS)*, Brussels, Belgium, 2008. DOI: 10.1088/1742-6596/97/1/012058.

[57] X.Y. Chen, J.X. Jin, K.M. Ma, J. Wen, Y. Xin, W.Z. Gong, A.L. Ren, and J.Y. Zhang. High Temperature Superconducting Magnetic Energy Storage and Its Power Control Technology. *Journal of Electronics Science and Technology of China*, 6(2): 137–142, 2008.

[58] A. Morandi, L. Trevisani, F. Negrini, P.L. Ribani, and M. Fabbri. Feasibility of SMES on Board of Ground Vehicles with Present State-of-the-Art Superconductors. *IEEE Transactions on Applied Superconductivity*, 22(2), 2012. DOI: 10.1109/TASC.2011.2177266.

[59] L. Trevisani, A. Morandi, F. Negrini, P.L. Ribani, and M. Fabbri. Cryogenic Fuel-Cooled SMES for Hybrid Vehicle Application. *IEEE Transactions on Applied Superconductivity*, 19(3):2008–2011, 2009. DOI: 10.1109/TASC.2009.2018482.

[60] K. Shikimaki, N. Hirano, S. Nagaya, H. Kawashima, K. Higashikawa, and T. Nakamura. System Coordination of 2GJ Class YBCO SMES for Power System Control. *IEEE Transaction on Applied Superconductivity*, 19(3):2012–2018, 2009. DOI: 10.1109/TASC.2009.2018491.

[61] S. Suzuki, J. Baba, K. Shutoh, and E. Masada. Effective Applications of Superconducting Magnetic Energy Storage (SMES) to Load Leveling for High Speed Transportation System. *IEEE Transactions on Applied Superconductivity*, 14(2): 713–716, 2004. DOI: 10.1109/TASC.2004.830082.

[62] J. Deng, J. Shi, Y. Liu, and Y. Tang. Application of a hybrid energy storage system in the fast charging station of electric vehicles. *IET Generation, Transmission and Distribution*, 10(4):1092–1097, 2016. DOI: 10.1049/iet-gtd.2015.0110.

[63] A. Cansiz, C. Faydaci, M.T. Qureshi, O. Usta, and D.T. McGuiness. Integration of a SMES-Battery-Based Hybrid Energy Storage System into Microgrids. *Journal of Superconductivity and Novel Magnetism*, 31(5):1449–1457, 2017. DOI: 10.1007/s10948-017-4338-4.

[64] Z. Wang, Z. Zou, and Y. Zheng. Design and Control of a Photovoltaic Energy and SMES hybrid system with current-source grid inverter. *IEEE Transactions on applied superconductivity*, 23(3):184–192, 2013. DOI: 10.1109/TASC.2013.2250172.

[65] Z. Wang, Y. Zheng, M. Cheng, and S. Fan. Unified control for a wind turbine-superconducting magnetic energy storage hybrid system based on current source converters. *IEEE Transactions on Magnetics*, 48(11):3973–3976, 2012. DOI: 10.1109/TMAG.2012.2201213.

[66] T. Ise, M. Kita, and A. Taguchi. A Hybrid Energy Storage With a SMES and Secondary Battery. *IEEE Transactions on Applied Superconductivity*, 15(2): 1915–1918, 2005. DOI: 10.1109/TASC.2005.849333.

[67] J.W. Shim, Y. Cho, S-J. Kim, S.W. Min, and K. Hur. Synergistic Control of SMES and Battery Energy Storage for Enabling Dispatchability of Renewable Energy Sources. *IEEE Transactions on Applied Superconductivity*, 23(3), 2013. DOI: 10.1109/TASC.2013.2241385.

[68] S. Wang, Y. Tang, J. Shi, K. Gong, Y. Liu, L. Ren, and J. Li. Design and advanced control strategies of a hybrid energy storage system for the grid integration of wind power generations. *IET Renewable Power Generations*, 9(2):89–98, 2014. DOI: 10.1049/iet-rpg.2013.0340.

[69] Z. Nie, X. Xiao, Q. Kang, R. Aggarwal, H. Zhang, and W. Yuan. SMES-Battery energy storage system for conditioning outputs from direct drive linear wave energy converters. *IEEE Transactions on applied superconductivity*, 23(3), 2013. DOI: 10.1109/TASC.2013.2246852.

[70] H. Alafnan, M. Zhang, W. Yuan, J. Zhu, J. Li, M. Eleshiekh, and X. Li. Stability Improvement of DC Power Systems in an All-Electric Ship Using Hybrid SMES/Battery. *IEEE Transactions on Applied Superconductivity*, 28(3), 2018. DOI: 10.1109/TASC.2018.2794472.

[71] J. Li, M. Zhang, Q. Yang, Z. Zhang, and W. Yuan. SMES/Hybrid Energy Storage System for Electric Buses. *IEEE Transactions on Applied Superconductivity*, 26(4), 2016. DOI: 10.1109/TASC.2016.2527730.

[72] M. Sander, R. Gehring, and H. Neumann. LIQHYSMES: A 48 GJ Toroidal MgB2-SMES for Buffering Minute and Second Fluctuations. *IEEE Transaction on Applied Superconductivity*, 23(3), 2013. DOI: 10.1109/TASC.2012.2234201.

[73] N. Bizon. Effective mitigation of the load pulses by controlling the Battery/SMES hybrid energy storage system. *Applied Energy*, 229(3):459–473, 2018. DOI: 10.1016/j.apenergy.2018.08.013.

[74] D. van Delft and P. Kes. The discovery of superconductivity. *Physics Today*, 63(9): 38–43, 2010.

[75] W. Meissner and R. Ochsenfeld. Ein neuer Effekt bei Eintritt der Supraleitfahigkeit. *Die Naturwissenschaften*, 21:787, 1933. DOI: 10.1007/BF01504252.

[76] A.M. Forrest. Meissner and Ochsenfeld revisited. *European Journal of Physics*, 4: 117–120, 1987. DOI: 10.1088/0143-0807/4/2/011.

[77] F. London and H. London. The electromagnetic equations of the supraconductor. *Proceedings of the Royal Society A*, 149(866):71–88, 1935. DOI: 10.1098/rspa.1935.0048.

[78] J.E. Hirsch. Why only hole conductors can be superconductors. In F.H. Teherani, D.C. Look, D.J. Rogers, and I. Bozovic, editors, *Proceedings of SPIE Vol 10105*, Bellingham, WA, 2017. DOI: 10.1117/12.2269644.

[79] J.E. Sonier. *The magnetic penetration depth and the vortex core radius in type-II superconductors.* PhD thesis, Department of Physics and Astronomy, University of British Columbia, 1998.

[80] A.A. Abrikosov. Nobel Lecture: Type-II superconductors and the vortex lattice. *Reviews of Modern Physics*, 76:975–979, 2004. DOI: 10.1103/RevModPhys.76.975.

[81] J.D. Doss. *Engineer's Guide to High-Temperature Superconductivity.* John Wiley & Sons Inc., 1989. ISBN 978-0-47151-307-0.

[82] I. Kesgin. *Processing and Electromagnetic Properties of Low AC Loss, Multifilamentary Rare Earth-Barium-Copper-Oxide Superconductor Tapes.* PhD thesis, University of Houston, 2013.

[83] M.C. Steele and R.A. Hein. Superconductivity of Titanium. *Physical Review*, 92(2): 243–247, 1953. DOI: 10.1103/PhysRev.92.243.

[84] J.F. Cochran, D.E. Mapother, and R.E. Mould. Superconducting Transition in Aluminium. *Physical Review*, 103(6):1657–1669, 1956. DOI: 10.1103/PhysRev.103.1657.

[85] T.P. Sheahen. *Introduction to High-Temperature Superconductivity.* Plenum Press New York, 1994. ISBN 978-0-306-47061-5.

[86] X.B. Xu, H. Fangohr, S.Y. Ding, F. Zhou, X.N. Xu, Z.H. Wang, M. Gu, D.Q. Shi, and S.X. Dou. Phase diagram of vortex matter of type II superconductors. *Physical Review B*, 83(014501), 2011. DOI: 10.1103/PhysRevB.83.014501.

[87] J. Bardeen, L.N. Cooper, and J.R. Schrieffer. Theory of Superconductivity. *Physical Review*, 108(5):1175–1204, 1957. DOI: 10.1103/PhysRev.108.1175.

[88] J.E. Hirsch and F. Marsiglio. Superconducting materials classes-introduction and overview. *Physica C*, 514:1–8, 2015. DOI: 10.1016/j.physc.2015.03.002.

[89] P.J. Ray. Structural investigation of $La_{2-x}Sr_xCuO_{4+y}$. Master's thesis, University of Copenhagen, 2015.

[90] K.A. Muller and J.G. Bednorz. The Discovery of a Class of High-Temperature Superconductors. *Science*, 237:1133–1139, 1987. DOI: 10.1126/science.237.4819.1133.

[91] H. Maeda and Y. Yanagisawa. Recent Developments in High-Temperature Superconducting Magnet Technology (Review). *IEEE Transactions on Applied Superconductivity*, 24(3), 2014. DOI: 10.1109/TASC.2013.2287707.

[92] R.M. Scanlan, A.P. Malozemoff, and D.C. Larbalestier. Superconducting Materials for Large Scale Applications. *Proceedings of the IEEE*, 92(10):1639–1654, 2004. DOI: 10.1109/JPROC.2004.833673.

[93] Superconductor Technologies Inc. About superconducting wire, . http://www.suptech.com/about_superconducting_wire_n.php, [Accessed 04 June 2018].

[94] Superpower Inc. 2G HTS Wire, . http://www.superpower-inc.com/content/2g-hts-wire, [Accessed 04 June 2018].

[95] M. Marchevsky. Quench detection and protection for hts accelerator magnets. Presentation, 3rd Workshop on Accelerator Magnets in HTS, September 2015.

[96] J. Nagamatsu, N. Nakagawa, T. Muranaka, Y. Znitani, and J. Akimitsu. Superconductivity at 39k in magnesium diboride. *Nature*, 410:63–64, 2001. DOI: 10.1038/35065039.

[97] C. Buzea and T. Yamashita. Review of superconducting properties of MgB_2. *Superconductor Science and Technology*, 14(11):R115–R146, 2001. DOI: 10.1088/0953-2048/14/11/201.

[98] C. Senatore, C. Barth, M. Bonura, M. Kulich, and G. Mondonico. Field and temperature scaling of the critical current density in commercial REBCO coated conductors. *Superconductor Science and Technology*, 29(1), 2015. DOI: 10.1088/0953-2048/29/1/014002.

[99] G. Majkic, R. Pratap, A. Xu, E. Galstyan, H.C. Higley, S.O. Prestemon, X. Wang, D. Abraimov, and V. Selvamanickam. Engineering current density over $5kA/mm^2$ at 4.2K, 14T in thick film REBCO tapes. *Superconductor Science and Technology*, 31(2), 2018. DOI: 10.1088/1361-6668/aad844.

[100] W. Goldacker, F. Grilli, E. Pardo, A. Kario, S.I. Schlachter, and M. Vojeniak. Roebel cables from REBCO coated conductors: a one-century-old concept for the superconductivity of the future. *Superconductor Science and Technology*, 27(2), 2014. DOI: 10.1088/0953-2048/27/9/093001.

[101] W. Goldacker, A. Frank, A. Kudymow, R. Heller, A. Kling, S. Terzieva, and C. Schmidt. Status of high transport current ROEBEL assembled coated conductor cables. *Superconductor Science and Technology*, 22(2), 2009. DOI: 10.1088/0953-2048/22/3/034003.

[102] C.P. Bean. Magnetization of High-Field Superconductors. *Reviews of Modern Physics*, 36(1):31–39, 1964. DOI: 10.1103/RevModPhys.36.31.

[103] Y.B. Kim ad C.F. Hempstead and A.R. Strand. Magnetization and critical supercurrents. *Journal of Physical Review*, 129(2):528–536, 1963. DOI: 10.1103/PhysRev.129.528.

[104] Z. Jiang, K.P. Thakur, M. Staines, R.A. Badcock, N.J. Long, R.G. Buckley, A.D. Caplin, and N. Amemiya. The dependence of AC loss characteristics on the spacing between strands in YBCO Roebel cables. *Journal of Superconductor Science and Technology*, 24, 2011. DOI: 10.1088/0953-2048/24/6/065005.

[105] P.W. Anderson. Theory of Flux Creep in Hard Superconductors. *Physical Review Letters*, 9(7):309–311, 1962. DOI: 10.1103/PhysRevLett.9.309.

[106] J. Rhyner. Magnetic properties and ac-losses of superconductors with power law current-voltage characteristics. *Physica C: Superconductivity*, 212(3-4):292–300, 1993. DOI: 10.1016/0921-4534(93)90592-E.

[107] Z. Zhang. *Electrical characterizing of superconducting power cable consisted of Second-Generation High-temperature superconducting tapes.* PhD thesis, University of Bath, 2016.

[108] J.W. Ekin. Offset criterion for determining superconductor critical current. *Applied Physics Letters*, 55(9):905–907, 1989. DOI: 10.1063/1.102259.

[109] K. Szota, J. Jedryka, M. Nabiaek, and M. Szota. Determination of current characteristics of 2G HTSC. *Scientific Research of the Institute of Mathematics and Computer Science*, 2(10):237–242, 2011.

[110] F. Grilli, E. Pardo, A. Stenvall, D.N. Nguyen, W. Yuan, and F. Gmry. Computation of Losses in HTS Under the Action of Varying Magnetic Fields and Currents. *IEEE Transactions on Applied Superconductivity*, 24(1), 2014. DOI: 10.1109/TASC.2013.2259827.

[111] M.P. Oomen. *AC loss in superconducting tapes and cables.* PhD thesis, University of Twente, 2000.

[112] A. Morandi, M. Fabbri, B. Gholizad, F. Grilli, F. Sirois, and V.M.R. Zermeno. Design and Comparison of a 1-MW/5-s HTS SMES With Toroidal and Solenoidal Geometry. *IEEE Transactions on Applied Superconductivity*, 26(4), 2016. DOI: 10.1109/TASC.2016.2535271.

[113] A. Hekmati and R. Hekmati. Double pancake superconducting coil design for maximum magnetic energy storage in small scale smes systems. *Cryogenics*, 80: 74–81, 2016. DOI: 10.1016/j.cryogenics.2016.09.009.

[114] O. Vincent-Viry, A. Mailfert, and D. Trassart. New SMES Coil Configurations. *IEEE Transactions on Applied Superconductivity*, 11(1):1916–1919, 2001. DOI: 10.1109/77.920225.

[115] M. Fabbri, D. Ajiki, F. Negrini, R. Shimada, H. Tsutsui, and F. Venturi. Tilted Toroidal Coils for Superconducting Magnetic Energy Storage Systems. *IEEE Transactions on Magnetics*, 39(6):3546–3550, 2003. DOI: 10.1109/TMAG.2003.819483.

[116] R.Radebaugh. Refrigeration for Superconductors. *Proceedings of the IEEE*, 92(10), 2004. DOI: 10.1109/JPROC.2004.833678.

[117] A.T.A.M de Waele. Basic Operation of Cryocoolers and Related Thermal Machines. *Journal of Low Temperature Physics*, 164:179–236, 2011. DOI: 10.1007/s10909-011-0373-x.

[118] R. Radebaugh. Cryocoolers: the state of the art and recent developments. *Journal of Physics: Condensed Matter*, 21, 2009. DOI: 10.1088/0953-8984/21/16/164219.

[119] S. Noguchi, Y. Oga, and H. Igarashi. Quench simulation of SMES consisting of some superconducting coils. *Physica C*, 471:1399–1403, 22011. DOI: 10.1016/j.physc.2011.05.203.

[120] Y. Yang, B. Wei, P. Chen, H. Zhang, M. Qiu, and D. Zhang. The Quench Protection System for Superconducting Magnetic Energy Storage. *IEEE Transactions on Applied Superconductivity*, 23(3), 2013. DOI: 10.1109/TASC.2012.2233855.

[121] S. Caspi, L. Chiesa, P. Ferracin, S.A. Gourlay, R. Hafalia, R. Hinkins, A.F. Lietzke, and S. Prestemon. Calculating Quench Propagation with ANSYS. *IEEE Transaction on Applied Superconductivity*, 13(2):1714–1717, 2003. DOI: 10.1109/TASC.2003.812867.

[122] S. Otten, A. Kario, A. Kling, and W. Goldacker. Bending properties of different REBCO coated conductor tapes and Roebel cables at T = 77 K. *Superconductor Science and Technology*, 29:125003, 2016. DOI: 10.1088/0953-2048/29/12/125003.

[123] F. Trillaud and L.S. Cruz. Conceptual design of a 200-kJ 2G-HTS Solenoidsl micro-SMES. *IEEE Transactions on Applied Superconductivity*, 24(3):5700205, 2013. DOI: 10.1109/TASC.2013.2284478.

[124] D. Kumar, F.Zare, and A.Ghosh. Dc microgrid technology: System architectures, ac grid interfaces, grounding schemes, power quality, communication networks, applications, and standardizations aspects. *IET Access*, 5:12230–12256, 2016. DOI: 10.1109/ACCESS.2017.2705914.

[125] V.G. Welsby. *The theory and design of inductance coils, 2nd edition.* Macdonald and co., 1960.

[126] V. Lombardo, E. Barzi, D. Turrioni, and A.V. Zlobin. Critical Currents of YBCO Tapes and BSCCO Wires at Different Temperatures and Magnetic Fields. *IEEE Transactions on Applied Superconductivity*, 21(3):3247–3250, 2011. DOI: 10.1109/TASC.2010.2093865.

[127] D. Hazelton and T. Lehner. Superpower 2G HTS Wire for Electrical and Magnet Applications. Presentation, 2010. https://indico.cern.ch/event/96071/attachments/1111052/1585241/2010_0504_CERN_Visit_DWH_pres.pdf, [Accessed 23 April 2019].

[128] Automeris. Web Plot Digitizer, 2019. https://apps.automeris.io/wpd/, [Accessed 24 April 2019].

[129] P.L. Walstorm and M.S. Lubell. Calculation of radial magnetic fields for axisymmetric solenoids with rectangular cross section. *Journal of Applied Physics*, 44(3): 4195–4198, 1973. DOI: 10.1063/1.1662917.

[130] H. Jones. *Handbook of Superconducting Materials*, chapter Electromagnets. Institute of Physics Publishing, 2003. ISBN 978-0-75030-898-4.

[131] M. Brooks and H.M. Turner. Inductance of Coils. *University of Illinois Bulletin*, 9 (53):4195–4198, 1912.

[132] S.L. Lalitha and R.C. Gupta. The Mechanical Design Optimization of a High Field HTS Solenoid. *IEEE Transactions on Applied Superconductivity*, 25(3), 2015. DOI: 10.1109/TASC.2014.2367153.

[133] S. Noguchi, H. Yamashita, and A. Ishiyama. An Optimal Design Method for SMES Coils Using HTS Tapes. *IEEE Transaction on Applied Superconductivity*, 12(1), 2002. DOI: 10.1109/TASC.2002.1018677.

[134] Q. Sun, Z. Zhang, L. Lin, Q. Qiu, D. Liu, G. Zhang, and S. Dai. Design Method of SMES Magnet Considering Inhomogenous Superconducting Properties of YBCO Tapes. *IEEE Transaction on Applied Superconductivity*, 24(3), 2014. DOI: 10.1109/TASC.2014.2304241.

[135] ABB. Insulated gate bipolar transistor (IGBT) and diode modules with SPT and SPT+ chips, 2019. https://new.abb.com/semiconductors/igbt-and-diode-modules, [Accessed 02 October 2019].

[136] J. Zheng, S.S. Peng, W.Y. Li, and Y.J. Dai. Magnet design of 10 MJ multiple solenoids SMES. In *IOP Conference Series: Earth and Environmental Science*, number 233, 2019. DOI: 10.1088/1755-1315/233/3/032026.